Alba Alcañiz Moya

Numerical simulation of c-Si solar cells based on transition metal oxide as carrier selective contact

Drift diffusion and *ab initio*

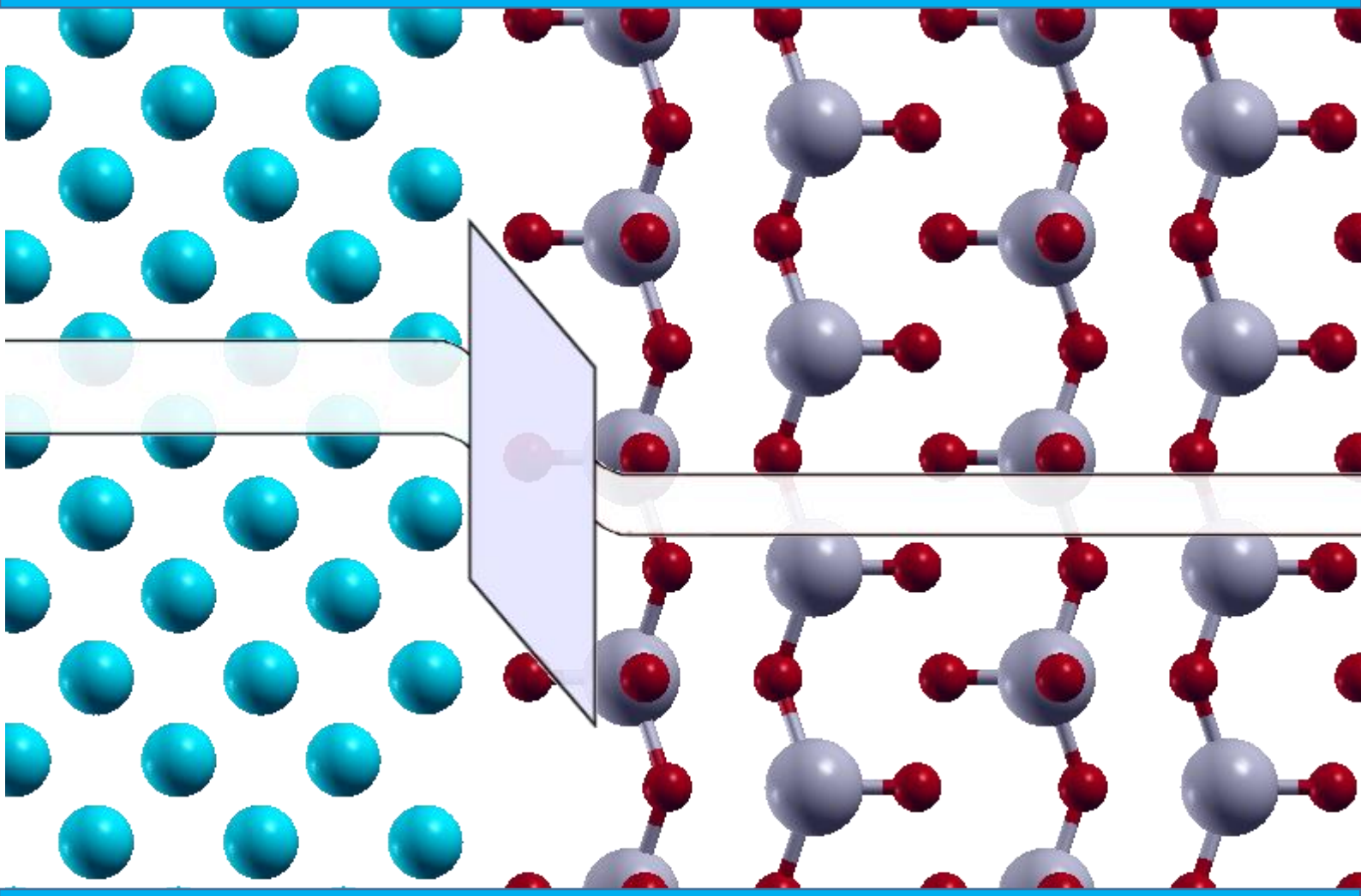

TU Delft

Numerical simulation of c-Si solar cells based on transition metal oxide as carrier selective contacts

Drift diffusion and *ab initio*

By

Alba Alcañiz Moya

in partial fulfilment of the requirements for the degree of

Master of Science
in Sustainable Energy Technology

at the Delft University of Technology,
to be defended publicly on Thursday June 4, 2020 at 10:00 AM.

Student number: 4939700
Project duration: October 2019 – June 2020
Thesis committee:

Dr. ir. O. Isabella,	TU Delft, ESE – PVMD	Supervisor
Dr. P. A. Procel Moya	TU Delft, ESE – PVMD	Daily supervisor
Dr. L. Mazzarella	TU Delft ESE – PVMD	Internal committee member
Prof. Dr. Ir. M. Zeman	TU Delft, ESE – PVMD	Internal committee member
Dr. R. Ishihara	TU Delft, Q&CE – QIT	External committee member

TU Delft

Abstract

Silicon heterojunction solar cells employing transition metal oxides as carrier selective contact are of particular interest due to the potential of reducing parasitic absorption while featuring optimal electrical properties. Recently, a record efficiency of 23.5% was achieved by employing molybdenum oxide (MoO_x) as carrier selective contact. MoO_x exhibits advantageous properties with respect to the p-doped standard amorphous silicon contacts due to its lower parasitic absorption and better thermal stability. However, achieving an efficient carrier collection is challenging and not well understood yet. In this work, transport of charge is studied from drift diffusion and atomistic approach by means of numerical simulations. Two different state-of-art computational tools are employed: TCAD Sentaurus for drift diffusion simulations, and VASP for *ab initio* simulations.

Through drift diffusion simulations, the contact formation of molybdenum oxide as carrier selective contact is consistently explored including quantum confinement and transport based in mid-gap energy states. The work function of MoO_x is shown to be the core for an efficient charge collection. Thanks to experimental results, it is revealed relevant phenomenon at MoO_x/intrinsic amorphous silicon (i-a-Si:H) interface which includes silicon oxide formation and charge accumulated. Therefore, a special focus at interface is here presented, in order to study the inner physics of the detrimental effects and how to avoid them. Altogether, drift diffusion simulations reveal that MoO_x thickness is an essential parameter because it strongly determines the work function and hence the efficiency of the solar cell. All the knowledge acquired is used to provide guidelines on the fabrication of these type of solar cells.

Looking at MoO_x/a-Si:H interface, *ab initio* simulations are employed to study interface properties. Accordingly, such interface is analysed using both materials in their crystalline matrix. It is demonstrated that oxygen deficiency tunes the MoO_x work function, a statement which is key for the proper contact formation and consistent with drift diffusion results. Finally, the charge arrangement at interface reveals the creation of an interface dipole together with silicon dioxide interlayer which is coherent with drift diffusion simulations analysis.

Acknowledgements

With this master thesis, I end my studies at Delft after two amazing years. This experience has been a great lesson, not only in sustainable energies but also in life. It has provided me with independence and motivated me to look from different perspectives.

I would like to thank first my daily supervisor Paul. He has been an amazing support, always trusting me and encouraging me to go further. He has helped me achieve many of the knowledge from this thesis. I would also like to thank Luana, for being the bridge between simulations and experiments. My gratitude also goes to my main supervisor, Olindo Isabella, for helping me whenever in need and for his insights and dedication. The insights from the crystalline silicon cluster meetings were also helpful. I wouldn't have been able to perform the *ab initio* simulations without the help from Jouke Heringa, which provided me access to the adequate server and helped me with the program. I would also like to thank Prof. dr. ir. Miro Zeman and Dr. Ryoichi Ishihara for being part of my graduation committee.

Thanks also to all the friends I have made during these two years. To the colleagues at Solar Monkey, who made me felt like I wasn't working. To Patrick for his willingness and patience while teaching me Dutch. Special thanks to Damiano, who has demonstrated to always be there, even on a Monday night. And to so many more that I have no room here to say.

I am also thankful for all the friends I left in Barcelona. Especially to the best writer and the best cook I know. They make me feel like I never left.

Special thanks to my family. It is very hard to miss so much such an important part of your life. They have always encouraged and trusted me, making me feel like I would never disappoint them. In particular, I want to thank my grandmothers, for being so strong until now and until the end.

Finally, I would like to thank Miguel for accompanying me in this adventure, and all the ones left to come.

Alba Alcañiz Moya

Schiedam, May 2020

Contents

Abstract i
Acknowledgements iii
List of figures vii
List of tables x
List of symbols xi
Latin symbols xi
Greek symbols xii
Acronyms xiii

1 Introduction 1
1.1 Motivation and outline of the thesis 2
2 Drift diffusion background and simulation framework 4
2.1 Semiconductor physics fundamentals 4
2.1.1 Heterojunctions 7
2.2 Simulation Approach 8
2.3 Working principle of TMO SHJ solar cells 10
2.4 Models and Parameters of the materials 11
3 Drift diffusion simulation results 13
3.1 Calibration and effect of MoO_3 work function 13
3.1.1 Validation 15
3.1.2 Impact of trap concentration 16
3.1.3 Impact of electron affinity 17
3.1.4 Realistic devices 18
3.2 Passivating contacts 20
3.2.1 Effect of SiO_2 interlayer 20
3.2.2 Work function attenuation 23
3.2.3 Reduction of the work function attenuation 25
3.2.4 SiO_2 and dipole 29
3.3 Maximizing the conversion efficiency 30
3.3.1 State of the art trends 30
3.3.2 Light management 31

3.3.3 Towards the maximum performance 32
3.4 Nature of dipole 33
4 Atomistic background 34
4.1 Density functional theory fundamentals 34
4.1.1 Born-Oppenheimer approximation 35
4.1.2 Hohenberg-Kohn theorems 35
4.1.3 Kohn-Sham equations 36
4.2 Implementation 37
4.2.1 VASP 38
4.2.2 Computational details 39
4.2.3 Approximations 39
4.3 Symmetry element 41
4.3.1 The lattice coincidence method 41
4.4 Structures of the materials 42
4.4.1 Silicon 43
4.4.2 Molybdenum trioxide 44
5 *Ab initio* simulation results 45
5.1 Validation of the model 45
5.2 Evaluation of the work function 47
5.2.1 Calculation approach 47
5.2.2 Effect of strain in MoO_3 49
5.2.3 Effect of oxygen deficiency 50
5.3 MoO_3/Si interface 51
5.3.1 Coincidence lattice 51
5.3.2 Atomic structure 52
5.3.3 Electrostatic potential 55
5.3.4 Interface dipole 57
6 Conclusions 60
7 Outlook 62
Bibliography 63

List of figures

Figure 2.1: Energy band diagram of an intrinsic semiconductor. 5

Figure 2.2: Energy band diagram of two different semiconductors isolated (left) and in a p-n junction under thermal equilibrium (right). 7

Figure 2.3: Schematic of the four transport mechanisms to overcome a barrier. The processes are indicated with red arrows for electrons, and blue ones for holes. 8

Figure 2.4: Simulation approach flowchart. 9

Figure 2.5: Sketch of the basis SHJ solar cells simulated in this work. 10

Figure 2.6: HTL (left) and ETL (right) equilibrium band diagrams of the simulated SHJ solar cell. Conduction and valence band levels are sketched in the diagrams. The trajectory of electrons (red circles) and of holes (blue circles) is also shown. 10

Figure 3.1: Band diagram of the simulated MoO_3 SHJ solar cell in quasi equilibrium conditions for MoO_3 work function values of 5 (left) and 6 (right) eV. 14

Figure 3.2: Open circuit voltage (left) and fill factor (right) of the simulated solar cells as a function of the MoO_3 work function for different trap concentrations. 14

Figure 3.3: Open circuit voltage (left) and fill factor (right) as a function of the MoO_3 work function for different trap distributions (continuous lines only). Figure extracted from [42]. 15

Figure 3.4: Band diagram for fixed low electron affinity (4.625 eV) and increasing trap concentration. 17

Figure 3.5: Band diagram for fixed trap concentration (10^{16} cm^{-3}) and increasing electron affinity. 18

Figure 3.6: Band diagram for the three devices with similar MoO_3 work function. 19

Figure 3.7: Sketch of the modified HTL of the SHJ solar cells simulated in this work. 20

Figure 3.8: TEM image of a MoO_3 SHJ solar cell, where the silicon oxide interlayer can be appreciated, from [82]. 20

Figure 3.9: Open circuit voltage and fill factor of the solar cell with varying SiO_2 interlayer thickness for $WFMoO3 = 6.3$ eV. 21

Figure 3.10: J-V curve with varying SiO_2 interlayer thickness for $WFMoO3 = 6.3$ eV (left) and $WFMoO3 = 5.5$ eV (right). 22

Figure 3.11: Sketch of the interface dipole between the MoO_3 and the neighbouring semiconductor. 24

Figure 3.12: Work function attenuation as a function of the dipole moment. 24

Figure 3.13: J-V curves (left) and band diagram (right) for the solar cells with different dipole moments. The drop across the dipole layer is represented in the band diagram, pointing out the magnitude of the work function attenuation. 25

Figure 3.14: Literature values of MoO_x work function as a function of thickness. The values used for the simulations in this work are also represented with black crosses. 26

Figure 3.15: Graphical explanation of Equation 3.6 where the three cases can be distinguished. 27

Figure 3.16: Graphical determination of $\Delta WFdipolet$ for the chosen $WFMoOxt$ in this work. 28

Figure 3.17: Open circuit voltage and fill factor as a function of MoO_x thickness with the dipole implemented. 28

Figure 3.18: Open circuit voltage (left) and fill factor (right) of the solar cells with dipole and different SiO_2 thicknesses as a function of MoO_x thickness. 29

Figure 3.19: Short circuit current of textured solar cells under different front layer thicknesses. 31

Figure 4.1: Graphical representation of the main assumption performed by the Kohn-Sham equations, from [95]. 37

Figure 4.2: Flowchart of the iterative solution of the Kohn-Sham orbitals, based on the diagram by [95]. 38

Figure 4.3: Graphical explanation of the lattice coincidence method. 42

Figure 4.4: Primitive (top row) and conventional (bottom row) unit cells of crystalline silicon observed from two orientations. The silicon atoms are represented by the light blue balls. Figures generated with XCrySDen [137]. 43

Figure 4.5: α-MoO_3 unit cell from two different perspectives. The three oxygen sites are indicated. Molybdenum atoms are represented by grey balls, while the oxygen atoms are the red coloured ones. Figures generated with XCrySDen [137]. 44

Figure 5.1: Relaxed lattice parameters from the structural optimization of $MoO_{2.75}$ and $MoO_{2.9375}$. The results were simulated for the three inequivalent oxygen positions for the atom with the lowest stoichiometry. The results obtained by [116] as well as the parameters for the stoichiometric oxide are added for comparison. 46

Figure 5.2: Schematic illustration of the approach employed to calculate the work function of MoO_3. The doubled slab and work function slab are pointed out. Figure based on [148]. 48

Figure 5.3: Local potential of MoO_3, with the Fermi level taken as zero reference. The work function has been pointed out. 49

Figure 5.4: MoO_3 work function as a function of the distortion of b lattice constant. 50

Figure 5.5: Work function of molybdenum oxides depending on oxygen deficiency. 51

Figure 5.6: Left, original MoO_3 unit cell employed in all previous calculations. Middle, modified MoO_3 unit cell for the interface simulations. Right, MoO_3 and Si interface. The dashed purple lines represent the limits between bilayers in the MoO_3 unit cells. Molybdenum atoms in grey, oxygen ones in red, silicon atoms in blue. Figures generated with XCrySDen [137]. 53

Figure 5.7: Left, total energy of the interface cell for MoO_3 moved across the Si unit surface cell. Right, top view of the unrelaxed interface structure unit cell. The two highest Si layers (blue) and lowest O (red) and Mo (grey) layers are shown. 54

Figure 5.8: Optimization of the Si-O distance. 54

Figure 5.9: Electrostatic potential at the interface. 56

Figure 5.10: Interface potential and band energy levels for the alignment of MoO_3 bulk potential by minimums (left) and by maximums (right). 56

Figure 5.11: Differential charge dQ (left) and charge transfer ΔQ (right) upon the formation of the MoO_3/Si interface. 58

Figure 5.12: Electrostatic potential difference at the interface between MoO_3 and Si due to rearrangement of charges. 59

List of tables

Table 2.1: Simulation parameters. 11

Table 3.1: Summary of comparison of the trends obtained in [42] and in this work. 15

Table 3.2: Parameters of three simulated devices with the same electron affinity and increasing trap concentration. 16

Table 3.3: Parameters of three simulated devices with fixed trap concentration and varying electron affinity. 17

Table 3.4: Parameters of three simulated devices with similar work function. 19

Table 3.5: Simulated parameters for the SiO_2 interlayer. 21

Table 3.6: Characteristics of the solar cells fabricated by Dréon [33] and their fittings. 30

Table 3.7: Comparison between the best fabricated SHJ solar cell with the best simulated solar cell in this work. 33

Table 5.1: Calculated lattice parameters for bulk MoO_3 compared to previous theoretical works and experiment. Percentage deviation from experimental values is given in brackets. 45

Table 5.2: Best coincidence lattice cells for Si and MoO_3. 52

List of symbols

Latin symbols

A	Dipole area
a_i	Conventional lattice vector
d	Dipole layer thickness
dQ	Differential charge
E	Energy
$E[n(\vec{r})]$	Energy functional
E_C	Bottom energy of conduction band
E_{cut}	Plane-wave cut-off energy
E_F	Fermi energy
E_{gap}	Energy band gap
E_V	Top energy of valence band
E_{vacuum}	Vacuum energy
E_{xc}^{true}	Non-classic self-interaction energy
$F(E)$	Fermi-Dirac probability
$F[n(\vec{r})]$	Universal functional
f_i	Surface vector
F_i	Superlattice unit vector
G_{th}	Carrier generation
$\hat{H}$	Hamiltonian operator
$\vec{J}_n$	Electron current density
$\vec{J}_p$	Hole current density
$\vec{k}$	Crystal lattice wave vector
k_B	Boltzmann constant
m_{ij}	Superlattice surface coefficients
n	Electron density
n_0	Ground state density
N_{trap}	Trap concentration
p	Dipole moment
p_i	Primitive lattice vector
q	Elementary charge
Q	Dipole charge
$\vec{r}_\mathrm{n}$	Position of electrons
$\vec{R}_\mathrm{n}$	Position of the lattice ions
R_{net}	Net recombination rate
R_{th}	Recombination
s_i	Strain of the interface surface
t	Time
t	Molybdenum oxide thickness
T	Temperature
$\hat{T}$	Kinetic operator
$T[n(\vec{r})]$	Kinetic energy functional
t_{opt}	Optimum TMO thickness
u	Bloch factor
v	Potential
$\hat{V}$	Potential operator
V_{bi}	Built-in potential
$V_{bi,max}$	Maximum built-in potential
v_{ext}	External potential
WF	Work function
$\boldsymbol{x}$	Three coordinates in space
Z_n	Atomic number of the nuclei

Greek symbols

Δ	Work function attenuation	ϵ	Electronic energy
ΔE_C	Conduction band offset	ϵ_0	Vacuum permittivity
ΔE_V	Valence band offset	θ_{ij}	Superlattice vectors angle
Δn	Local charge density	ρ	Electrical charge density
ΔQ	Charge transfer	σ_{DP}	Interface charge density
ΔV	Electrostatic potential difference	φ	Electrostatic potential
$\Delta \bar{V}$	Average electrostatic potential	ϕ	Wave function
ΔWF_{cation}	Cation work function attenuation	χ	Electron affinity
ΔWF_{dipole}	Dipole work function attenuation	χ	Nuclear wave function
ΔWF_{donor}	Donor work function attenuation	ψ	Electronic wave function
ε_i	Kohn-Sham eigen-energy	ψ_0	Ground state wave function
ϵ	Relative permittivity	∇^2	Laplacian

Acronyms

1BZ	First Brillouin zone
Å	Armstrong
a-Si	Amorphous silicon
B2BT	Band to band tunnelling
BZ	Brillouin zone
CB	Conduction band
CSC	Carrier selective contact
c-Si	Crystalline silicon
D	Debye
DFT	Density functional theory
ETL	Electron transport layer
eV	Electronvolt
FF	Fill factor
GGA	Generalized gradient approximation
GPa	Gigapascal
HSE06	Heyd, Scuseria and Ernzerhof functional
HTL	Hole transport layer
ITO	Indium tin oxide
J	Current
J_{SC}	Short circuit current density
LDA	Local density approximation
Mo	Molybdenum
MoO_3	Molybdenum trioxide
MoO_x	Sub-stoichiometric molybdenum trioxide
Mo^{X+}	Molybdenum cation (X = 4,5,6)
n-Si	Highly n-type doped amorphous silicon
O	Oxygen
PAW	Projector augmented wave
PBE	Perdew, Burke and Ernzerhof functional
SHJ	Silicon heterojunction
Si	Silicon
SiO_2	Silicon dioxide
SRH	Shockley Read Hall
TAT	Trap assisted tunnelling
TCAD	Technology computer-aided design
TCO	Transparent conductive oxide
TMO	Transition metal oxide
V	Voltage
V_2O_5	Vanadium pentoxide
VASP	Vienna *ab initio* simulation package
VB	Valence band
vdW	Van der Waals

vdW-DF2	Van der Waals functional
V_{OC}	Open circuit voltage
WO_3	Tungsten trioxide

1 Introduction

The use of carrier selective contacts (CSC) in crystalline silicon (c-Si) solar cells potentially allows to overpass the conversion efficiency of the homo-junction counterparts. Efficiencies as high as 25.1% have been achieved on both-side contacted solar cells applying this strategy [1]. The record cell, fabricated by Kaneka, consists on a c-Si bulk caped in both sides with a thin layer of amorphous Si (a-Si) passivation layer including n-type and p-type doped amorphous silicon carrier selective contacts [2].

The key of success in this solar cell is found on the usage of amorphous silicon as passivating layer. This material shows a high quality interface with the c-Si wafer, suppressing the minority carrier recombination at the surface of the bulk [1] and enhancing the open circuit voltage [3]. This fact is due to the good lattice-matching with c-Si [4]. Furthermore, the use of a-Si CSC is industrially appealing due to its low thermal budget and ease of deposition with respect to conventional c-Si homo-junction solar cells [5].

However, amorphous silicon exhibits a relatively high absorption coefficient [6]. Indeed, using amorphous silicon in front side of solar cells is detrimental due to its parasitic absorption ascribed to the low band gap (1.7 eV) [7]. This fact strongly limits the short circuit current in solar cells employing it as CSC [8]. Moreover, the thermal instability of the material hinders the fabrication process of the solar cell [9]. Furthermore, doping a-Si requires of toxic boron and phosphorus gas precursors, which should be replaced for risk-free materials [10]. These drawbacks have encouraged the exploration of novel materials and strategies. The combination of thin films materials with c-Si in solar cells are gaining importance due to the increased flexibility to tune optoelectrical properties towards CSC [11]. Among thin film materials, novel materials such as organic materials or transition metal oxides (TMOs) as CSC in silicon heterojunction (SHJ) solar cells have proven to be a feasible alternative [9].

TMOs have been extensively used in perovskites [12], [13] and organic [14], [15] solar cells. They are characterized by their wide range of work function values, from 3.5 to 7.0 eV [16]. Exhibiting a relatively wide band gap (> 2.8 eV), most of TMOs are transparent in the visible and infrared regions, hence reducing the parasitic absorption compared to a-Si front layers [17], [18]. The possibility of low-temperature [9] and thin-layer [19] deposition make them attractive for fabrication process. Moreover, TMOs can have either a n or p-type character, determined by defects in the material background [20].

TMOs allow carrier selectivity by inducing the conditions for a n or p-type contact [21] through a proper energy alignment [22]. They enable efficient transport of only one type of carrier while hindering the transport of the other, thus reducing recombination at the interface. Accordingly, TMOs can exhibit properties of hole or electron contacts depending on the energy alignment [23].

Among TMO as hole transport layers, the most common are molybdenum trioxide (MoO_3) [24], vanadium pent-oxide (V_2O_5) [25], [26] and tungsten tri-oxide (WO_3) [27]. Their high work function makes them suitable as hole-selective contacts [10]. Moreover, their wide bandgap results in a low optical absorption and allows for sufficient carrier selectivity even when using layers of only a few nanometres thick [9]. Additionally, they are highly compatible with well-developed technology for processing solar cells [28]–[30].

Although these three oxides have similar characteristics, molybdenum trioxide has shown a particular performance with respect to the other two [25], [31], [32]. This is due to an appropriate band alignment with silicon because of its higher work function compared to the other two materials. Moreover, out of the three compounds, MoO_3 causes the least oxidation effects on the adjacent material [32]. In fact, this material has recently stablished the record efficiency of 23.5% [33] for solar cells based on TMOs silicon heterojunction technology.

The most important characteristic of molybdenum trioxide is its high oxygen reactivity. During thermal deposition, oxygen reacts with the surrounding layers [32] resulting in a slightly sub-stoichiometric molybdenum oxide (MoO_x where x is within the range $2<x<3$) [32] with amorphous character [34]. These oxygen vacancies allow energy levels slightly below the conduction band, giving the material a n-type character [35], and increasing its conductivity [36].

The oxygen vacancy amount together with the material work function is essential for the effectiveness of MoO_x as hole transport layer [37]. The work function controls the barrier height at the c-Si/MoO_x interface, while the oxygen vacancies are the ones that assist the tunnelling of charge carriers through the contact [38]. A well-balanced defect content would lead to the best performances. However, in presence of a low work function or little oxygen vacancies, hole collection issues arise in the device [39]. The performance of the solar cell is affected, resulting in S-shapes in the J-V curves [40].

However, the oxygen reactivity is very sensitive not only to the already mentioned interfacial reactions but also to air and oxygen exposure [41]. It is worth noting that such vacancies as sub-gap energy states are uncontrollable from process perspective. Moreover, during processing, the interfacial reactions induce surface oxidation of the bulk, reducing the passivation quality [42]. That is the reason why MoO_x alone is not the best candidate for the passivation of c-Si, and is usually deposited on top of a passivating amorphous silicon layer [40], [43].

This type of solar cell has great perspectives and prospects but there is still scope for improvement. There are issues when understanding the detrimental phenomena and the interfacial reactions with the deposited adjacent materials. SHJ solar cells employing molybdenum oxide as CSC is a topic under research.

1.1 Motivation and outline of the thesis

The motivation of this thesis lies in understanding how the physical properties of molybdenum oxide affect the performance of the solar cell. The goal is to identify the limits of this transition metal oxide to build performant charge carrier selective contact in solar cells. This study will be performed through the support of simulation tools. Based on a previously calibrated Technology Computer-Aided Design (TCAD) model and some experimental characterization, this project will i) validate the device modelling, ii) identify the dominant physical mechanisms, iii) propose an

optimization and iv) provide guidelines for developers to increase the performance. Through this path, the following questions will be answered:

- What are the main material parameters affecting the contact formation? Chapter 3
- How is the transport behaviour?
- What are the limiting physical mechanisms for hole transport layer stack?
- What material parameters can be controlled during the process to improve conversion efficiency?
- What is the atomistic nature of interface charge rearrangement?

This thesis can be divided into two sections. The first section consists on drift diffusion simulations, enclosed in Chapters 2 and 3. The first chapter starts with a background in semiconductor physics and describes the simulation approach used in semiconductor devices. The next Chapter 3 discusses the results obtained through drift diffusion simulations regarding the use of molybdenum oxide as carrier selective contact in solar cells. The first four questions will be discussed and answered in this third chapter.

The second part of this work, which consists on Chapters 3 and 5, regards *ab initio* simulations. These simulations will be a strong support to the results obtained in the previous computational experiments. Chapter 3 gives some concise theoretical background on the topic and presents the modelled materials. The following Chapter 5 describes the main outcomes achieved through *ab initio* simulations, and in particular, it discusses the atomistic nature of the interface charge rearrangement.

This work closes with the conclusions in Chapter 6 and a brief outlook in Chapter 7.

2

Drift diffusion background and simulation framework

In this chapter, the basis of semiconductor physics for solar cells applications is presented as the foundation of numerical simulation tool models. For this purpose, section 2.1 presents the fundamental level of semiconductor physics, emphasizing on heterojunction systems. Then, section 2.2 describes the simulation methodology employed by the numerical solver. Section 2.3 presents the working principle of silicon heterojunctions employing molybdenum oxide as carrier selective contact as an application of fundamental concepts. Finally, section 2.4 summarizes the main computational parameters and models of the devices.

2.1 Semiconductor physics fundamentals

Semiconductors are solid state materials with conductivity between conductors and insulators. Their electrical properties can be modified by temperature, illumination, magnetic field, and impurities. Such properties make them extremely useful for modern electronics [4].

The atoms in any compound are chemically bonded to each other. For semiconductors, such as crystalline silicon, the link is a covalent bond achieved by sharing electrons. These shared electrons are called valence electrons. For temperatures higher than the absolute zero, these bonds can be broken by thermal vibrations [4]. When that occurs, a valence electron is liberated, becoming a free electron that can participate in current conduction. Free electrons have a higher energy than valence electrons. The electron deficiency that is left behind can be filled by neighbouring electrons. In other words, such electron deficiency is like a positively charged particle that has moved. That particle is so-called a hole and it also contributes to the electric current.

The electrons in an isolated atom have discrete energy levels [44]. When isolated atoms are brought together in order to form a compound, the orbits of their outer electrons overlap and interact with each other. This interaction causes the discrete energy levels to be continuous and form a band. The free electrons form a so-called conduction band (CB), while the valence electrons form a valence band (VB). The holes are also located on the valence band. For semiconductors, there is a relatively small energy gap between the CB and the VB, where no states are available. Defining the bottom energy of the CB as E_C, and the top energy of the VB as E_V, the width of this forbidden gap is $E_{gap} = E_C - E_V$ [45].

As already mentioned, at absolute zero there are no thermal vibrations, therefore the electrons occupy the lowest energy states; the valence band is full, while the conduction band is empty. As the temperature increases, thermal energy excites electrons from the VB to the CB leading to an equal number of holes in the valence band. The higher the temperature, the greater the amount of excited carriers. The probability $F(E)$ that an electron occupies an electronic state with energy E at a certain temperature T is given by the Fermi-Dirac distribution function [46], Equation 2.1.

$$F(E) = \frac{1}{1 + e^{(E-E_F)/k_B T}} \tag{2.1}$$

Where k_B is the Boltzmann constant, and E_F is the Fermi energy or Fermi level, in which the probability of occupation is equal to $1/2$. For semiconductors with no impurities (named intrinsic), the Fermi energy is located in the middle of the band gap. Another important quantity is the vacuum energy E_{vacuum}; the energy of a free electron which is outside of any material.

The vacuum level, Fermi energy, bottom energy of the CB and top energy of the VB can be represented in a so-called band diagram. The interpretation of this schema gives crucial understanding of semiconductor devices. Figure 2.1 shows the band diagram of an intrinsic semiconductor.

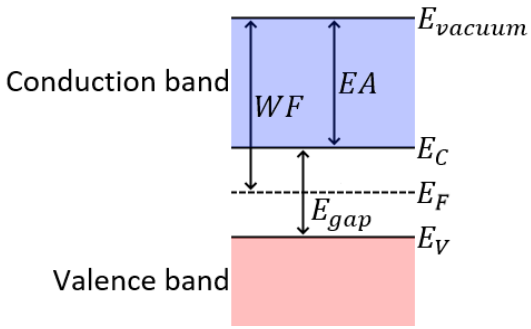

Figure 2.1: Energy band diagram of an intrinsic semiconductor.

Two more additional quantities can be established by looking at the schematic graph. First, the electron affinity χ, defined as the energy needed for an electron of the conduction band to reach the vacuum level. Related to it, the work function WF is the energy width between the vacuum level and the Fermi level.

$$\chi = E_{vacuum} - E_C \tag{2.2a}$$

$$WF = E_{vacuum} - E_F \tag{2.2b}$$

In order to tune the density of electrical charge carriers ρ, semiconductors are usually doped with impurities. This action displaces the Fermi energy by adding energy levels in the material. If the impurities (or doping) induce the excess of electrons, dopants are called donor and the semiconductor becomes n-type. Similarly, for impurities providing excess of holes in the semiconductor, the dopant is called an acceptor and the semiconductor, a p-type.

In a n-type semiconductor, due to the impurities added, there is a higher density of electrons than holes. In these materials, electrons are the majority charge carriers, while holes are the minority ones. The equivalent case occurs for p-type semiconductors, where holes are the majority charge carriers, and electrons are the minority ones.

The dynamics of the charge carriers can be tuned by a junction of two materials. If the jointed compounds are the same one, a homo-junction is formed. If the two materials are different, a heterojunction is created. Independently of the type of union, the junction is formed between a n-type and a p-type semiconductor.

The electrons in the conduction band move thermally. That motion is random and with no net displacement. When a junction of two compounds is formed, additional velocity components are superimposed creating a net movement and therefore a current. When these materials are brought together, large carrier concentration gradients cause carrier diffusion of electrons (holes) to the p-(n-)type material. This current due to the spatial difference between the concentration of each species is called diffusion current. When the charge carriers leave their respective sides, the doping ions left behind are uncompensated. This fact creates an electric field, and consequently a drift current, on the opposite direction to the diffusion current. Thermal equilibrium is reached when these two forces compensate each other.

This electric field creates a variation of the electrostatic potential at different points of the device. The conduction and valence band energies are proportional to the electrostatic potential φ through the elementary charge $E = -q\varphi$ [45]. Therefore, the energy levels also vary as a function of distance. When this variation is represented in the band diagram, the energy levels experience a bending.

The shape of the electrostatic potential is determined by solving Poisson's equation [47]. Poisson equation relates the density of electrical carriers ρ to the electrostatic potential. It is displayed in Equation 2.3, where ϵ is the relative permittivity of the semiconductor, and ϵ_0 is the vacuum permittivity. By knowing the boundary conditions in the device as well as several material characteristics, Poisson equation can be solved, which provides the electrostatic potential, and in turn the energy band diagram in static conditions.

$$\nabla(\nabla\varphi) = -\frac{\rho}{\epsilon\epsilon_0} \tag{2.3}$$

When an external excitation breaks chemical bonds of electrons, an electron hole pair is generated. The amount of charge carriers formed is quantified by the carrier generation G_{th}. In a solar cell, this generation is induced by optical excitation. This excess of charge carriers alters the equilibrium of the device. In order to restore it, recombination R_{th} processes of minority and majority charge carriers occurs. In equilibrium, recombination equals carrier generation.

There are three possible recombination processes: radiative, Auger and Shockley Read Hall (SRH). This thesis only refers to SRH recombination [48], due to the nature of the main material studied. Information on the other processes can be found elsewhere [45].

SRH recombination occurs by means of an impurity atom or crystal defect [48]. The impurities produce energy levels inside the forbidden gap, called trap-states. An electron or hole can be trapped in this defect. When trapped, they can attract the opposite charge carrier and recombine with each other.

The defects are mainly ascribed to (i) impurities inside the material or (ii) the abrupt termination of a surface. Surface defects appear at semiconductor interfaces due to the abrupt discontinuity of the lattice structure [4]. The amount of impurities is related to the dissimilarity between lattice parameters and the interaction between adjacent layers. Passivation of the surface can reduce the surface recombination [49]. It consists on depositing an adjacent material with similar lattice

parameters. For instance, in the case of c-Si, hydrogenated amorphous silicon (a-Si) is a widely used passivating material [50].

All these effects (drift and diffusion currents, generation and recombination) determine the dynamics of electron and holes [51]. These in turn stablish the working principle of semiconductor devices as solar cells. The magnitudes are related through the continuity equations (Equation 2.4a and 2.4b), based on the charge conservation inside the device. $\vec{J}_n$ and $\vec{J}_p$ are the current densities of electrons and holes, respectively, and $R_{net} = (G_{th} - R_{th})$ is the net recombination rate.

$$-\nabla \vec{J}_p = qR_{net,p} + q\frac{\partial p}{\partial t} \tag{2.4a}$$

$$\nabla \vec{J}_n = qR_{net,n} + q\frac{\partial n}{\partial t} \tag{2.4b}$$

2.1.1 Heterojunctions

A heterojunction is the junction of two dissimilar semiconductors. The left sketch in Figure 2.2 shows the energy band diagram of two isolated materials before the formation of a heterojunction. In this band diagram, the semiconductors are assumed to have different electron affinities, energy band gaps and work functions. To understand the band diagram of the junction under thermal equilibrium, two main aspects need to be considered. First, the Fermi level must be constant thorough the sample as reference energy. Secondly, the vacuum level must be continuous and parallel to the band edges, in order to preserve the properties of the material [52]. These two conditions create discontinuities on the conduction and valence bands of the sample, which sometimes result in barriers for the electrons and holes. This phenomenon can be observed in the energy band diagram under thermal equilibrium in Figure 2.2 (right). A new parameter is defined in the sketch, the built-in potential V_{bi}, which is the total electrostatic potential difference between the p-side and the n-side neutral regions at thermal equilibrium [4].

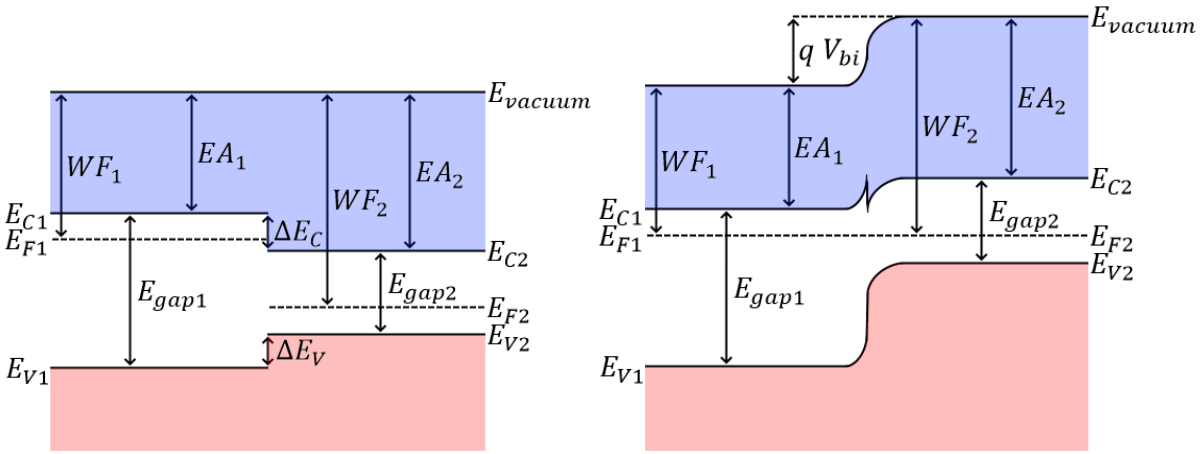

Figure 2.2: Energy band diagram of two different semiconductors isolated (left) and in a p-n junction under thermal equilibrium (right).

The barriers that arise due to band discontinuities will be an obstacle to charge carriers in the heterojunction. They will need to transport by means of thermionic emission across a barrier or by tunnelling through it [4]. Thermionic emission is a transport mechanism in which charge carriers with an energy above the barrier energy are able to travel over a potential barrier.

If the carrier does not have enough energy, it still has a finite probability of overcoming the barrier. This non-classical phenomenon is explained by the wavelike behaviour of particles on the quantum scale [4]. The necessary conditions for tunnelling to occur are: (i) carrier population available to tunnel, (ii) a finite tunnelling probability, and (iii) available states to which the carriers can go at the other side of the barrier. The tunnelling probability is related to the size of the barrier, the dielectric constant of the barrier material and the tunnelling mass [53].

Tunnelling can be further classified into direct tunnelling and trap assisted tunnelling (TAT), whether the transport is assisted by traps or not. Direct tunnelling can be distinguished again into intra band tunnelling and band to band tunnelling (B2BT). The main difference between the two transport mechanisms is that in the former, the carrier stays in the same band after having trespassed the barrier.

As previously mentioned, impurities inside a material are recombination centres for the charge carriers, since they can capture and emit charge carriers [54]. These traps can have a positive effect on the device if they assist the tunnelling. When an electron (hole) from one extreme of the energy barrier is captured by a trap, a hole (electron) from the other side of the barrier can reach that trap and be recombined with the captured charge carrier. Overall, it is the same effect as if an electron (hole) had overcome the barrier [55]. Once the impurity is free, it is able to capture again another charge carrier. TAT is a more efficient transport than direct tunnelling, since the carriers need less energy to overcome the barrier, due to the use of intermediate states [56].

The three tunnelling mechanisms together with thermionic emission are represented in Figure 2.3.

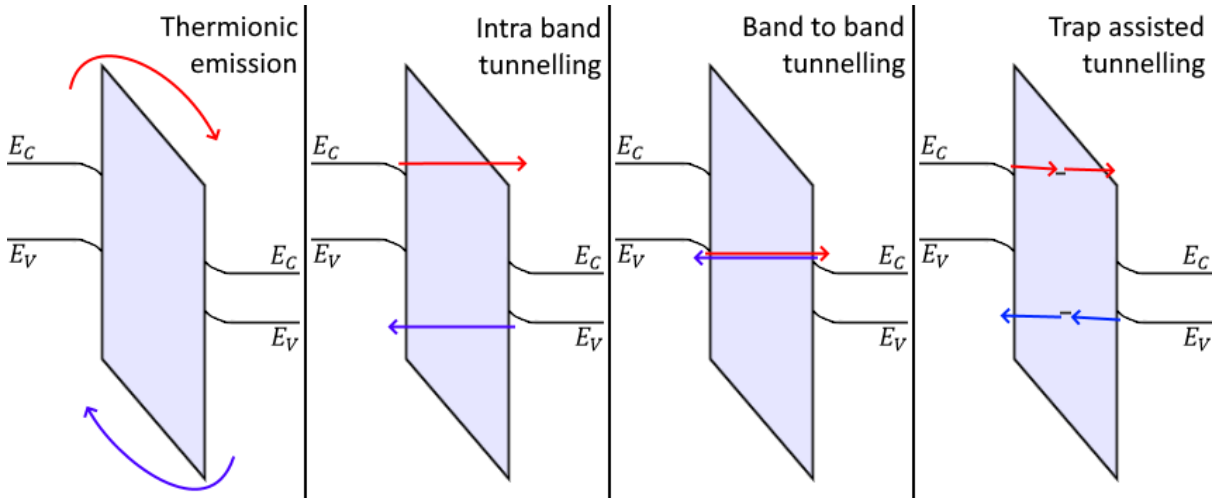

Figure 2.3: Schematic of the four transport mechanisms to overcome a barrier. The processes are indicated with red arrows for electrons, and blue ones for holes.

2.2 Simulation Approach

The semiconductor physics numerical solver used in this thesis is TCAD Sentaurus by Synopsys [57]. TCAD stands for Technology Computer-Aided Design and it is a tool which employs computer simulations to develop and optimize semiconductor processing technologies and devices [58]. It is the adequate solver to represent solar cells and study the physical phenomena occurring inside the structure in order to solve the issues encountered in fabricated devices.

The first step of the simulation is to create the device structure. This implies setting all the layers in the right order and its thicknesses. The material opto-electronic properties are also included in this step. Then the metal and optical contacts (boundary conditions) need to be defined. Finally, a mesh of the device is calculated to proper consider the physics inside the structure [59]. It determines the number of points available in each layer and interface. A denser mesh implies higher number of points, hence greater accuracy. There is a trade-off with the computational cost, therefore the mesh is generally very dense on the critic interfaces and less packed on the bulk of the materials.

Once the virtual device is built, the physical modelling needs to be solved. It consists on the set of equations presented in section 2.1, also called the drift diffusion model. This set is complemented by additional physical models that mimic the physical behaviour of SHJ, such as the tunnelling models just discussed. The simulator provides a numerical solution of this collection which is consistent with all the optical and tunnelling models implemented.

The physical modelling starts by solving Poisson equation (Equation 2.3) in static conditions. This allows to observe the energy band diagram under thermal equilibrium. Then, the voltage of the device is increased under 1 sun illumination until the current across the solar cell is smaller than 0. With this transition, the current-voltage (J-V) curve of the solar cell is obtained. Poisson as well as the continuity equations (Equations 2.4) for electrons and holes are solved in this level.

With the electron and hole densities obtained under the already mentioned different conditions, several parameters such as recombination, current density, or energy band diagram can be determined. The magnitudes can be visualized in order to understand the different phenomena occurring inside the solar cell.

All the simulation steps are graphically represented in the flowchart of Figure 2.4.

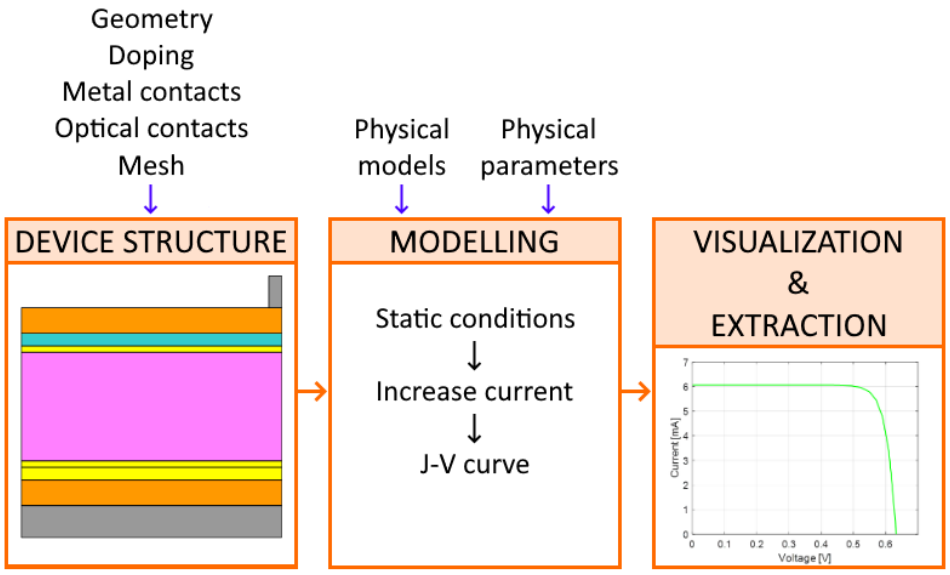

Figure 2.4: Simulation approach flowchart.

2.3 Working principle of TMO SHJ solar cells

This section explains the working principle of the SHJ solar cells simulated in this work. Each solar cell consists on the bulk material, an electron transport layer (ETL) that collects electrons, and a hole transport layer (HTL) which gathers holes.

This work studies the use of molybdenum oxide (MoO_3) as carrier selective contact. Because of its large work function (6.82±0.05 eV [16]), when in contact with n-type c-Si, a hole inversion layer is formed. Therefore, although MoO_3 is an n-type semiconductor, it acts as a hole transport layer in n-type SHJ solar cells [60]. For that reason, this work mainly focuses on the hole transport layer.

The HTL is composed of a passivating layer of hydrogenated intrinsic amorphous silicon (a-Si), followed by molybdenum oxide, then transparent conductive oxide (TCO) made of indium tin oxide (ITO) and finally a silver front metal contact. On the other side of the solar cell, the ETL is made of a-Si passivating layer, highly n-type doped amorphous silicon (n-Si), ITO TCO and finally a full area covered silver contact. Figure 2.5 shows the sketch of the basis solar cell simulated in this work.

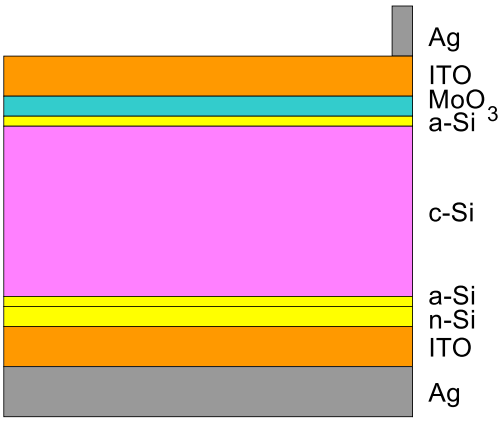

Figure 2.5: Sketch of the basis SHJ solar cells simulated in this work.

Figure 2.6 shows the energy band diagram of the electron and hole electron transport layers of the above solar cell. Because of the electric field on the c-Si bulk, the holes are attracted to the HTL (left graph) and the electrons are drawn to the ETL (right graph).

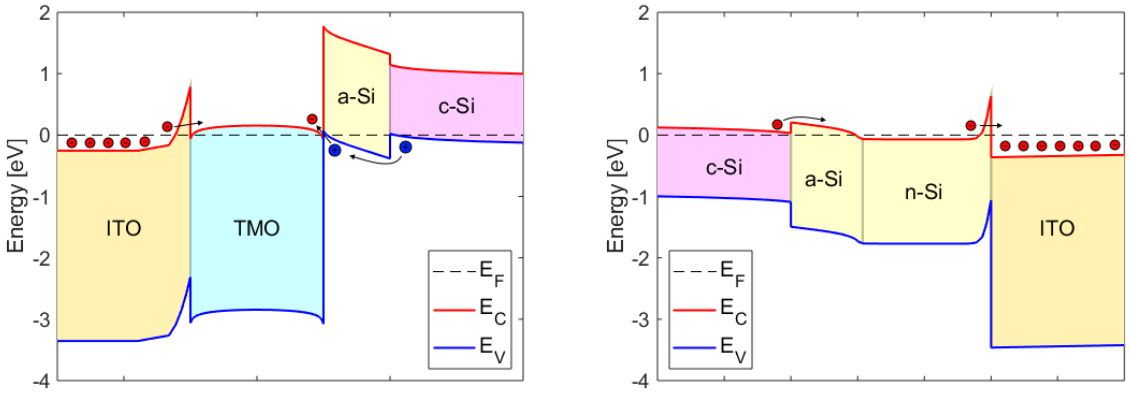

Figure 2.6: HTL (left) and ETL (right) equilibrium band diagrams of the simulated SHJ solar cell. Conduction and valence band levels are sketched. The trajectory of electrons (red circles) and of holes (blue circles) is also shown.

Starting with the HTL (left figure), holes are attracted to the interface between a-Si and c-Si owing to the electric field of the bulk. These holes are able to tunnel the encountered barrier at the a-Si interface by direct tunnelling. When they reach the TMO/a-Si interface, the holes recombine with the electrons of the MoO_3 either by TAT or B2BT, depending on the density of traps, energy alignment and the work function of the TMO. The conduction of carriers in high work function metal oxides is facilitated by defect states close to the Fermi level [61]. This phenomenon is further explained in section 3.1. The MoO_3 electrons come from the ITO, after crossing the barrier by direct tunnelling at the ITO/TMO interface. In turn, these electrons have reached the TCO by lateral transport from the front metal contact.

Often, the limitation in this contact is because the hole accumulation at the c-Si/a-Si interface is not enough for the tunnelling to occur [62]. The hole accumulation is represented by the energy difference between the valence band of c-Si and the Fermi level. It is reduced by the insufficient band bending, which implies a low electric field. There are several parameters that affect this band bending, as will be tackled along this work.

On the opposite extreme of the device (right figure), the electrons are attracted to the c-Si/a-Si interface by the electric field of the bulk. They encounter a small barrier, but they are able to trespass it by direct tunnelling. There is a high availability of energy states on the highly n-type doped amorphous silicon, that are able to cross the barrier at the n-Si/ITO interface again by direct tunnelling. An even greater amount of unoccupied states can be found on the ITO, which are easily transported to the metal contact.

2.4 Models and Parameters of the materials

This section states the parameters and physical models employed by the numerical solver.

Table 2.1: Simulation parameters.

	Quantity	Value
Global	Temperature	300 K
	Spectrum	AM1.5
	Pitch	600 µm
Physical models	Free carrier statistics	Fermi-Dirac [15]
	Transport mechanisms	Thermionic emission [63] Non-local B2BT with two-band dispersion relation [64], [65]
	Free carrier mobility	High field saturation [66]
	Doping	Phosphorus and boron constant profile
c-Si bulk	Thickness	270 µm
	Resistivity	n-type 2 Ωcm unless stated otherwise
	Electron tunnelling mass	0.19 [67]
	Hole tunnelling mass	0.16 [67]
	Lifetime	1 ms
	Band gap narrowing	Schenk model [68]
	Recombination	SRH with doping-dependent lifetime [69] Auger model [70]

	Quantity	Value
a-Si	Free carrier mobility	Philips unified mobility model [71]
	Band gap	1.7 eV [7]
	Electron affinity	3.9 eV [7]
	Tunnelling mass	0.1 [7]
n-Si	Thickness	10 nm
	Doping	n-type 10^{21} cm^{-3}
passivating layers	Thickness	5 nm unless stated otherwise
	Doping	n-type 10^{3} cm^{-3}
Molybdenum oxide	Thickness	10 nm unless stated otherwise
	Band gap	3 eV [42]
	Electron affinity	Varied between 5 and 6 eV
	Doping	n-type 6.78 10^{12} cm^{-3}
	Electron density of states	6.78 10^{18} cm^{-3} [72]
	Hole density of states	7.92 10^{17} cm^{-3} [72]
TCO	Thickness	75 nm
	Doping	n-type 10^{20} cm^{-3}
	Electron affinity	4.9 eV [73]
	Band gap	3.7 eV [7]
	Recombination	SRH with doping-dependent lifetime [69]
Silver metal contacts	Thickness	1 µm
	Front shading	5 %

3

Drift diffusion simulation results

This chapter describes and discusses the results of numerical simulations based in drift diffusion model. Section 3.1 explores the effect of the trap concentration and work function of MoO_3, being the parameters that affect the most the contact formation. Next, section 3.2 focuses on the interface between MoO_3 and a-Si, exploring the effect of the oxygen deficiency on the performance of the solar cell. Then, section 3.3 proposes strategies for maximizing the conversion efficiency based on investigations of state-of-art solar cells including their light management. Finally, section 3.4 introduces atomistic models (*ab initio*) to deep in understanding material properties.

3.1 Calibration and effect of MoO_3 work function

The first step is to construct an accurate state of the art model in order to properly simulate SHJ solar cells using MoO_3. This study is based on state-of-art simulation work performed by Messmer et al [42]. A consequent objective of this approach is to understand the effect of the trap concentration and work function of MoO_3 in the conversion of efficiency. These two quantities are considered the main parameters that affect the contact formation of the devices under analysis [37].

[42] stresses the transport limitations at the TMO/a-Si interface. The most important property of this interface is the position of the bottom of the MoO_3 conduction band, $E_{C,MoO3}$, with respect to the top of the valence band of the a-Si passivation layer, $E_{V,a-Si}$. There is a change in transport mechanism when the two bands are aligned. If the conduction band of the MoO_3 is lower than the valence band of a-Si ($E_{C,MoO3} < E_{V,a-Si}$), the charge carriers are able to tunnel from band to band (band to band tunnelling, B2BT). However, if $E_{C,MoO3} > E_{V,a-Si}$, the charge carriers need to overcome this barrier by the assistance of the traps of the MoO_3 (trap assisted tunnelling, TAT). The lower the trap density, the harder is the transport for the charge carriers, hence the lower the efficiency. These traps represent oxygen vacancies of the material, which have been found to assist the transport [74]. For higher WF_{MoO3} values, the transport is B2BT hence the trap concentration is not important anymore because TAT is not limiting. The change in transport phenomena occurs for $WF_{MoO3} = E_{V,a-Si} = 5.62$ eV.

The objective is to calibrate the simulated model by reproducing the phenomenon reported in [42]. The structure of the device simulated is the one described in Figure 2.5. The MoO_3 density of states was fixed to 5 10^{20} cm^{-3} and the bulk resistivity was set to 1 Ω*cm in order to mimic the parameters from the reference paper. The work function of the molybdenum oxide was tuned from 5 to 6 eV. In order to illustrate this change, band diagrams of the solar cell in quasi equilibrium

conditions have been sketched in Figure 3.1. They show the relative position of the band energies under MoO_3 work functions of 5 and 6 eV (left and right graph, respectively).

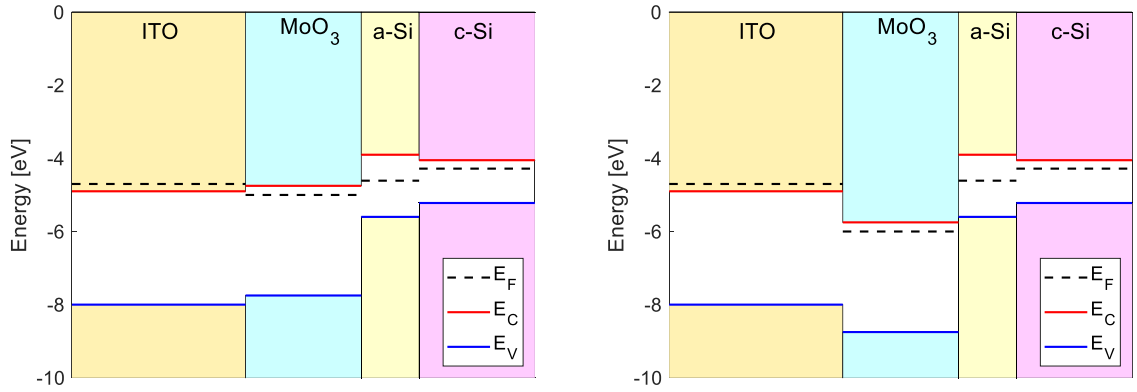

Figure 3.1: Band diagram of the simulated MoO_3 SHJ solar cell in quasi equilibrium conditions for MoO_3 work function values of 5 (left) and 6 (right) eV.

The open circuit voltage (V_{OC}) and fill factor (FF) of these simulated devices is shown in Figure 3.2. These two electrical parameters are indicators of transport and selectivity. Therefore, by examining their behaviour under different electron affinities and trap concentrations N_{trap} of the MoO_3 layer, the effect of the TMO work function can be examined. The two photovoltaic magnitudes show a similar trend: an improvement as the work function increases until a saturation value is reached.

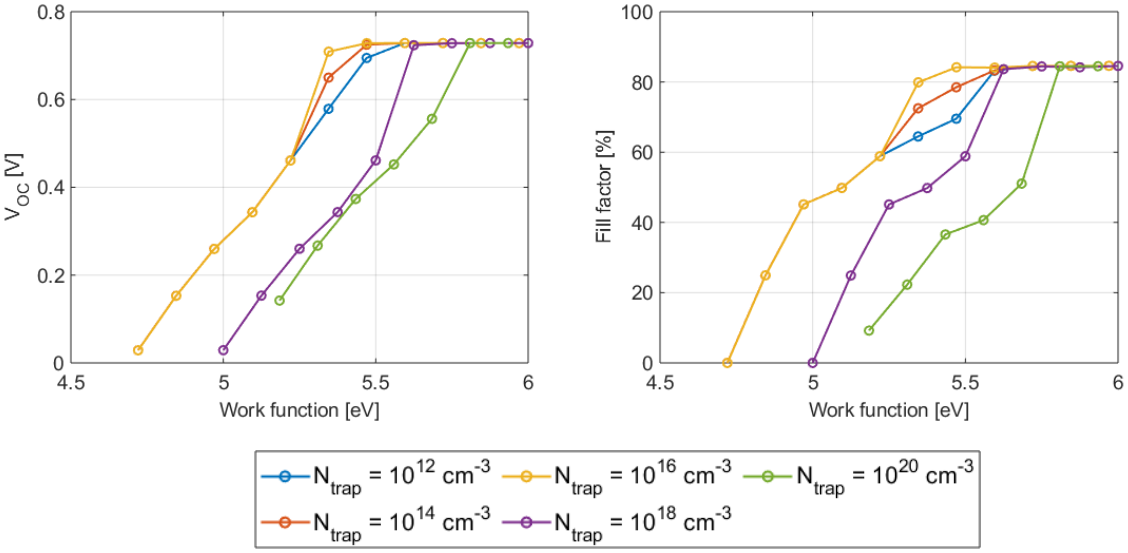

Figure 3.2: Open circuit voltage (left) and fill factor (right) of the simulated solar cells as a function of the MoO_3 work function for different trap concentrations.

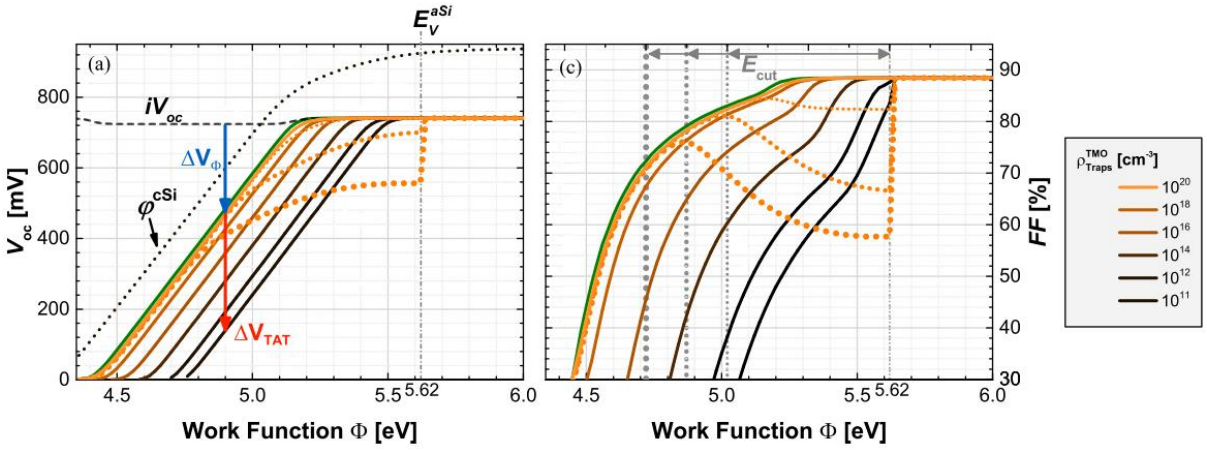

Figure 3.3: Open circuit voltage (left) and fill factor (right) as a function of the MoO_3 work function for different trap distributions (continuous lines only). Figure extracted from [42].

For comparison purposes, Figure 3.3 shows the open circuit voltage and fill factor values obtained by Messmer [42] as a function of work function and trap concentration (continuous lines on the graph). Although both results exhibit similar trends, some differences can be appreciated. They will be analysed in the first subsection.

3.1.1 Validation

In order to validate the simulation approach employed in this thesis, similar devices reported in [42] are simulated and the results are compared. A comparison of approaches from both simulation platforms is summarized in Table 3.1.

Table 3.1: Summary of comparison of the trends obtained in [42] *and in this work.*

Messmer et al. [42]	*This work*
Work function depends solely on electron affinity	Work function depends on electron affinity and trap density
No TCO	Includes TCO
Minimum work function value of 4.5 eV	Minimum work function value of 4.75 eV
Change from TAT to B2BT for 5.62 eV	Change from TAT to B2BT for 5.97 eV

- In [42], the work function depends only on the electron affinity $WF_{MoO3} = \chi_{MoO3}$. Experimentally, changes in work function were reported not only due to electron affinity [75], but also due to carrier density variations [36]. In this work we study the effects of both carrier density (by altering the trap doping concentration) and electron affinity changes, following the example by [76]. This difference in work function variation explains that although the trends of both works are similar, the effect of the trap density is different.
- These simulations did not employ MoO_3 work function values as low as 4.5 eV. For this value, independently of the amount of traps present in the MoO_3, the band bending is not enough. This effect is observed on the band diagram in quasi equilibrium from Figure 3.1. The work functions of a-Si and ITO are 4.8 and 4.7 eV, respectively. If $WF_{MoO3} = 4.5$ eV, the bending of the bands would be opposite to the desired one. Therefore, the holes would be repelled instead of attracted. This issue is not encountered by [42] because of the difference in work function variation and the absence of the TCO layer.
- The limiting work function in which the transport mechanism changes from TAT to B2BT is also different. As previously mentioned, this change in regime occurs for 5.62 eV in [42].

However, in the present work, B2BT is apparent when MoO_3 work function is approximately 5.97 eV, which corresponds to $E_{V,a-Si}$.

Overall, the differences in the simulated devices show that the solar cells simulated in this work are closer to fabricated devices because of the integration of the transparent conductive oxide layer as semiconductor, as well as the dependence of work function on trap concentration. However, it is worth noting that none of the abovementioned methods mimic a realistic device because, in both simulation works, the distribution of traps is uniform among the energy and TMO background. Such assumptions were employed because they can highlight a specific phenomenon, but their premises are hard to find in nature.

Sections 3.1.2 to 3.1.4 explain the trends obtained and reported in Figure 3.2. Three variations are studied: (i) the effect of increasing the trap concentration at fixed electron affinity, (ii) the effect of enhancing the electron affinity at fixed trap concentration, and (iii) how different electron affinity and trap concentrations yield the same work function value.

3.1.2 Impact of trap concentration

To analyse the effect of trap concentration, three set of simulations are performed corresponding to solar cells using MoO_3 with the same electron affinity $\chi = 4.625$ eV, but increasing trap concentration. The work function, open circuit voltage and fill factor of these devices are presented in Table 3.2. The work function increases with the trap concentration, since as displayed in Table 3.1, the WF depends not only on the electron affinity, but also on the trap concentration. From the electrical values, it can be observed: (i) these devices exhibit low efficiency (< 2.5 %), (ii) the greater the trap concentration, the higher the performance. The band diagram of these devices will explain these variations.

Table 3.2: Parameters of three simulated devices with the same electron affinity and increasing trap concentration.

χ [eV]	WF [eV]	N_{trap} [cm^{-3}]	V_{OC} [mV]	FF [%]
4.62	4.84	10^{12}	153	24.9
4.62	5.12	10^{18}	153	24.9
4.62	5.31	10^{20}	267	22.3

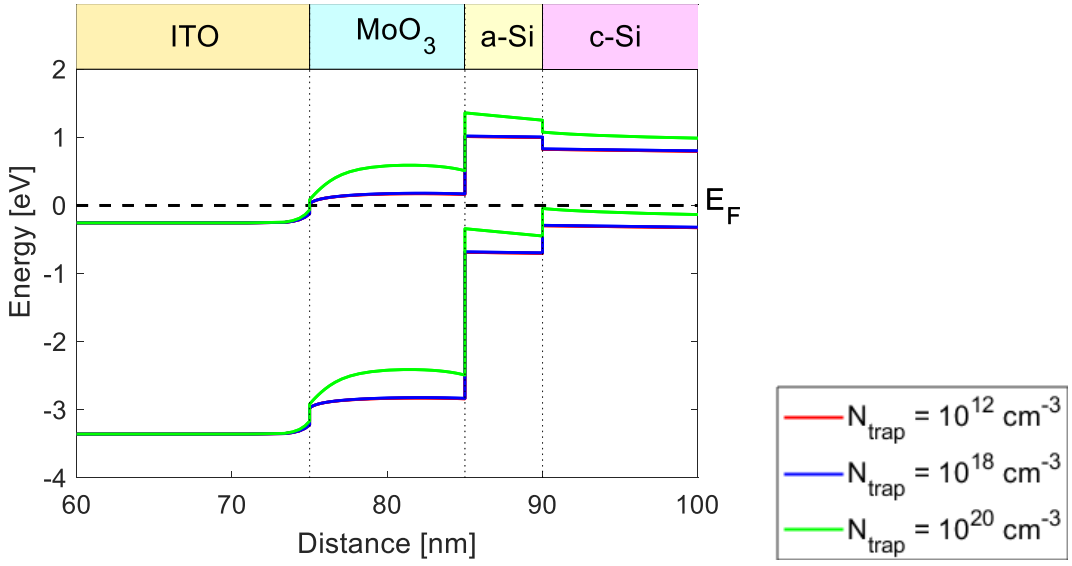

Figure 3.4: Band diagram for fixed low electron affinity (4.625 eV) and increasing trap concentration.

Focusing first on the two lowest trap concentration values (red and blue curves from the above figure), their band diagrams are mostly overlapping. That explains why their V_{OC} and FF values are the same. One can also observe the high energy difference between the c-Si valence band and the Fermi level. That occurs because there is no bending of the bands at the c-Si interface due to the small TMO WF. The consequence of that is a low accumulation of holes. This low accumulation explains the deficient V_{OC} and FF obtained.

When the trap concentration is increased to 10^{20} cm^{-3}, the band bending at the c-Si interface improves considerably (green line in Figure 3.4). The energy difference between the Fermi level and the valence band at the c-Si interface is reduced with respect to the two previous cases, resulting in a higher hole accumulation. This explains the greater V_{OC} value obtained. However, for this device, the FF is slightly reduced. The reason for this is the hindered transport of charge carriers, due to the smaller electron accumulation at the MoO_3 layer. It can be observed by the higher energy difference between the MoO_3 conduction band and Fermi level with respect to the two cases with lower trap concentration.

3.1.3 Impact of electron affinity

We consider a set of simulations for devices featuring MoO_3 with fixed trap concentration but varying the electron affinity values. In these devices, the TMO work function increases at the same rate as the electron affinity. Their photovoltaic performance parameters are summarized in Table 3.3. From a first inspection of the table, it can be seen that there is a considerable improvement with increasing electron affinity. This enhancement can be understood by analysing the band diagram of these three devices, Figure 3.5.

Table 3.3: Parameters of three simulated devices with fixed trap concentration and varying electron affinity.

χ $[eV]$	WF $[eV]$	N_{trap} $[cm^{-3}]$	V_{OC} $[mV]$	FF [%]
4.75	4.97	10^{16}	260	45.1
5.00	5.22	10^{16}	461	58.9
5.25	5.47	10^{16}	728	84.2

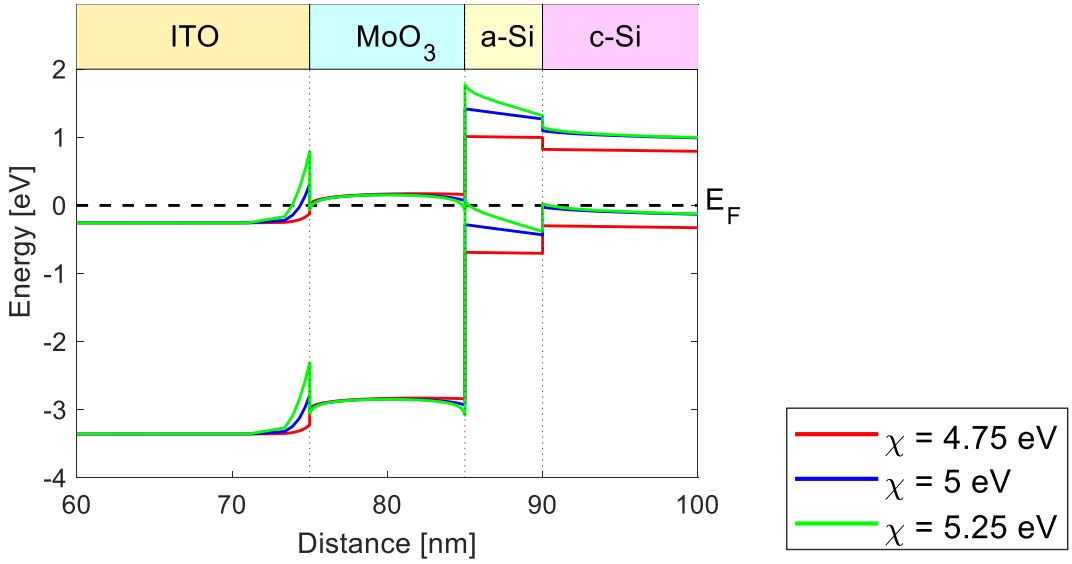

Figure 3.5: Band diagram for fixed trap concentration (10^{16} cm^{-3}) and increasing electron affinity.

By inspecting the band diagram, one can observe that the energy difference between the valence band and the Fermi level at the c-Si surface is reduced as the electron affinity increases. This explains the increase in open circuit voltage. However, that is not the only feature that affects V_{OC}. The bending at c-Si for 5 and 5.25 eV electron affinity is the same, but there is a considerable enhancement in open circuit voltage. This improvement is due to the higher bending not at the c-Si interface, but at the MoO_3/a-Si interface.

The red (4.75 eV) and blue (5 eV) curves in Figure 3.5 show an energy difference between the valence band of a-Si and the conduction band of MoO_3. The transport of charge carriers from one band to the other is assisted by traps (trap assisted tunnelling). The energy difference is smaller for 5 eV electron affinity compared to the 4.75 eV case, which explains the increase in FF. For the highest electron affinity (5.25 eV), there is no longer an energy difference between the valence band of a-Si and the conduction band of MoO_3. Tunnelling can occur without the help of impurities (B2BT). This change in transport mechanism explains the greater improvement in fill factor for the highest electron affinity, as well as the saturation observed in the photovoltaic parameters in Figure 3.2. Once the band levels are aligned, (i) an increase in work function does not imply a smaller energy barrier, and (ii) the transport is no longer hindered by the use of traps, therefore an increase in trap concentration does not imply a rise in fill factor.

One more aspect that can be observed on Figure 3.5 is the increase of the energy barrier at the MoO_3/ITO interface. Such barrier appears due to the difference in work function levels between the adjacent layers and the fulfilment of Anderson's law [52]. This barrier is thin enough and the electron accumulation at the TCO is high enough so that the tunnelling transport is not hindered, having no effect on the electrical performance.

3.1.4 Realistic devices

During the fabrication of TMO SHJ solar cells, the work function of MoO_3 is more commonly used as a reference, rather than the electron affinity or the trap concentration. Quite a common measured value of MoO_3 work function is 5.7 eV [16], [34], [38], [75], [77]–[79]. For that reason, this set of solar cells has in common a TMO work function close to 5.7 eV with the objective to represent a more realistic structure. The similar work function is achieved by a trade-off between

electron affinity and trap concentration: if the electron affinity increases, the trap concentration needs to decrease. This trade-off together with the FF and V_{OC} of these devices are shown in Table 3.4.

Table 3.4: Parameters of three simulated devices with similar work function.

χ [eV]	WF [eV]	N_{trap} [cm^{-3}]	V_{OC} [mV]	FF [%]
5.00	5.68	10^{20}	556	51.1
5.25	5.75	10^{18}	728	84.4
5.50	5.72	10^{16}	729	84.6

The devices with 5.75 eV and 5.72 eV work function exhibit almost identical photovoltaic characteristics. However, the device with a work function of 5.68 eV shows a reduced open circuit voltage and fill factor. This decrease in performance cannot be explained by the difference in work function. Therefore, the band diagram of these three devices needs to be compared in order to understand this behaviour, Figure 3.6.

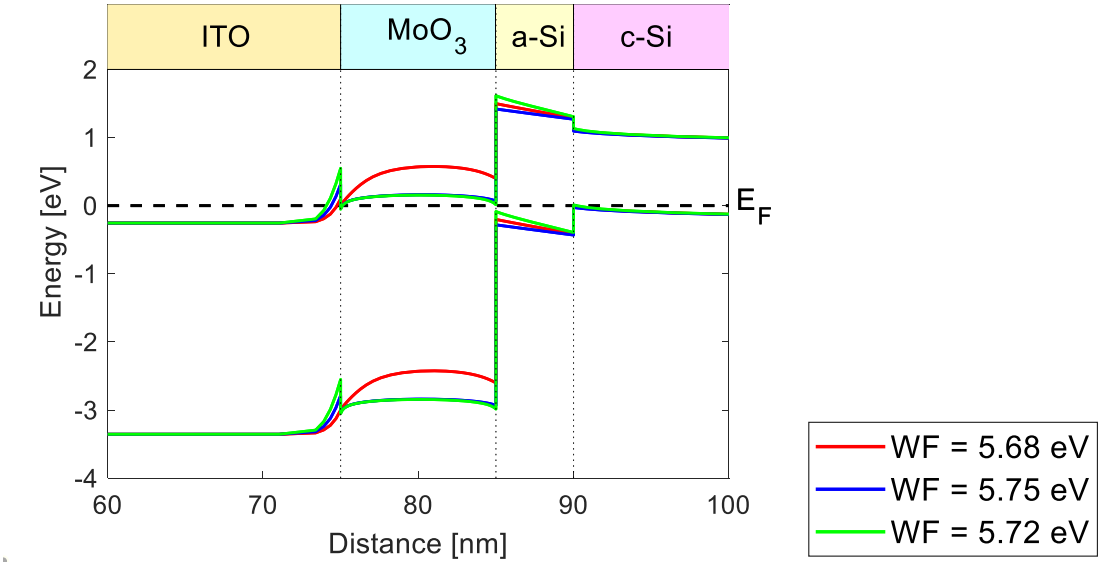

Figure 3.6: Band diagram for the three devices with similar MoO_3 work function.

Since the three simulated devices have a very similar MoO_3 work function, the band bending at the a-Si/c-Si interface is equivalent. The blue and green curves, which correspond to the band diagrams of the devices with work function of 5.75 and 5.72 eV respectively, are almost overlapping. This overlapping explains the similarity between electrical parameters in Table 3.4. From the two, the device with 5.72 eV work function shows a higher performance because the energy barrier at the a-Si/MoO_3 interface is slightly reduced.

In Figure 3.6, the red curve represents the band diagram of the device with a work function of 5.68 eV. The most prominent difference in this curve with respect to the other two, is the high energy difference between the MoO_3 conduction band and the Fermi level. This energy difference results in an increased energy barrier at the a-Si/MoO_3 interface. This explains the reduced performance with respect to the other two solar cells. These three examples show how devices with the same work function do not necessarily have the same performance.

3.2 Passivating contacts

As mentioned during the Introduction, a common problem in the solar cells under study is the high oxygen reactivity of MoO_3. This reactivity results in interfacial reactions with surrounding layers [32], which affect the performance of the solar cell [38], [80]–[83]. In the solar cells simulated in this study, two interfaces with the TMO are encountered: MoO_3/a-Si, and MoO_3/ITO.

Several papers have claimed to encounter issues at the TMO/ITO interface [38], [41], [81], [83]. In particular, [38] obtained an S-shape because of barriers encountered at the surrounding interfaces of the MoO_3. With proper deposition conditions, they were able to get rid of the barrier at the transparent conductive oxide interface. However, they could not remove the energy barrier at the a-Si/MoO_3 interface with adequate deposition conditions. More groups have encountered that interface problematic [80]–[82], rather than the TMO/ITO interface, so the focus will be on the a-Si/MoO_3 interface.

The objective of this section is to analyse the phenomena that occur on the a-Si/MoO_3 interface through semiconductor physics simulations. To this purpose, the interface between MoO_x and a-Si is modelled as ultrathin virtual layer with tuneable properties to mimic interface phenomena for different analysis, as shown in Figure 3.7.

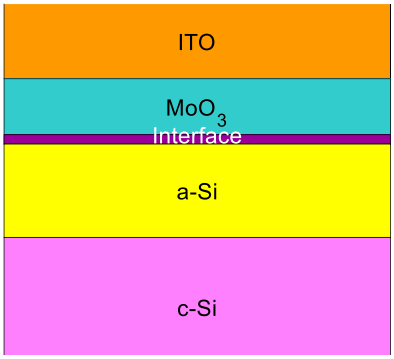

Figure 3.7: Sketch of the modified HTL of the SHJ solar cells simulated in this work.

3.2.1 Effect of SiO_2 interlayer

It is common to find silicon oxide interlayers on the MoO_3/a-Si interface of the solar cell devices in study [80]–[82], [84]. An example can be observed in the TEM image in Figure 3.8 [82]. This thin interlayer is claimed to increase the contact resistivity at the hole contact [81] and to create a hole barrier that limits the cell properties at room temperature. The hole barrier is due to the high band gap of 9.3 eV of the oxide [85].

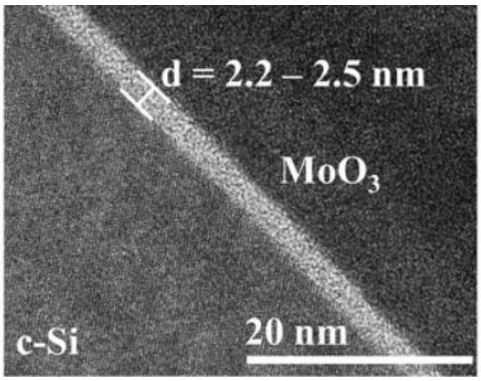

Figure 3.8: TEM image of a MoO_3 SHJ solar cell, where the silicon oxide interlayer can be appreciated, from [82].

This section studies the effect that a silicon dioxide (SiO_2) interlayer has on the performance of the solar cell. To do so, a SiO_2 interlayer was placed at the a-Si/MoO_3 interface. Table 3.5 displays the simulation parameters of this layer. In this section, two set of simulations are performed in which the interlayer thickness is increased, in order to find the effect that it has on the performance of the solar cell. This thickness increase is performed under a high (6.3 eV) and a low (5.5 eV) MoO_3 work function scenario. These two values are within the range of measured MoO_3 work function [34], [86], [87].

Table 3.5: Simulated parameters for the SiO_2 interlayer.

	Quantity	**Value**
SiO_2 interlayer	Thickness	2 nm unless stated otherwise
	Electron tunnelling mass	0.32 [56]
	Hole tunnelling mass	0.4 [56]

Starting with the devices with 6.3 eV MoO_3 work function, the open circuit voltage and fill factor as a function of the SiO_2 thickness can be observed in Figure 3.9. The graph shows a steady open circuit voltage until 2.3 nm thickness is reached. Below that thickness, the insulator layer merely acts as an ohmic contact with negligible resistance in our case. Above that thickness, the interlayer acts as an effective insulator limiting the current since the charge carriers can no longer tunnel through it [88].

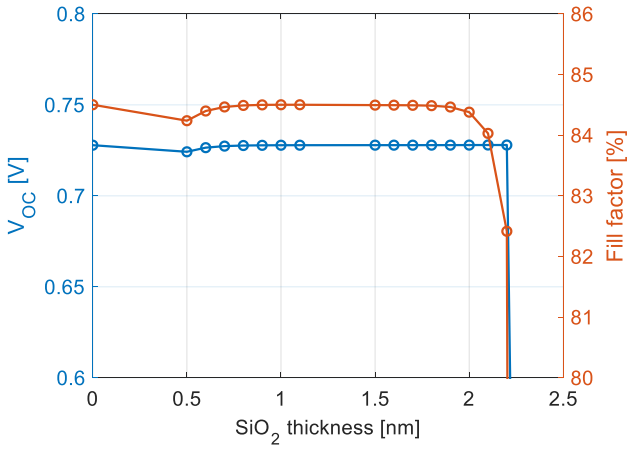

Figure 3.9: Open circuit voltage and fill factor of the solar cell with varying SiO_2 interlayer thickness for $WF_{MoO3} = 6.3$ eV.

The fill factor of these devices shows a similar behaviour with increasing interlayer thickness, although the insulator effect is already visible for 2 nm of SiO_2. The decrease in fill factor is better understood by looking at the J-V curves of these devices (left graph of Figure 3.10), still under the high (6.3 eV) work function scenario. The shape of J-V curves, and consequently the fill factor, are barely affected by the increase in SiO_2 thickness.

The J-V curve of a cell without SiO_2 interlayer has also been added as reference in the left graph of Figure 3.10. Surprisingly, when there is no interlayer, a decrease in open circuit voltage occurs. This drop is caused by a leakage current of electrons from a-Si to MoO_3. Because of the high band gap (9.3 eV) and energy alignment of SiO_2, the interlayer acts not only as a barrier for holes, but also as a barrier for electrons. Therefore, the SiO_2 interlayer ceases the leakage current. Overall, as long as the SiO_2 interlayer is thinner than 2.3 nm, there is no detrimental effect in the performance of the solar cell with a MoO_3 WF of 6.3 eV.

This phenomena is not in concordance with what is found in literature, where S-shapes are generally found in presence of a silicon oxide interlayer [77], [81]. In order to observe this event, the previous set of devices has to be simulated under a lower MoO_3 WF of 5.5 eV. This value was the measured one on [77], where a SiO_2 interlayer was spotted. The J-V curves corresponding to these devices can be observed in the right graph of Figure 3.10.

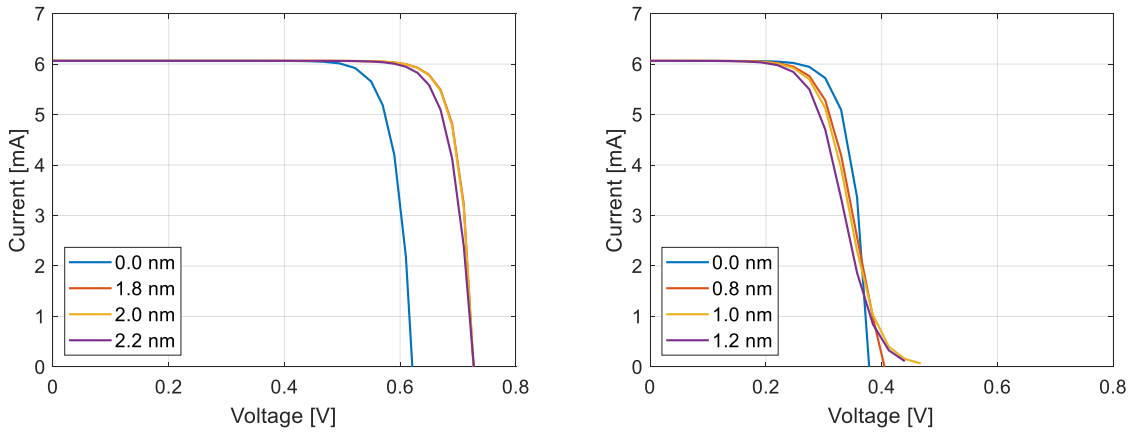

Figure 3.10: J-V curve with varying SiO_2 interlayer thickness for $WF_{MoO3} = 6.3$ eV (left) and $WF_{MoO3} = 5.5$ eV (right).

In these curves, the S-shape can be appreciated for SiO_2 thicker than 1 nm. This particular shape occurs when there are transport issues across the device, which will be explained shortly. The open circuit voltage values are also reduced with respect to the higher WF simulated solar cells. Moreover, the tunnelling limit for these solar cells has decreased to 1.6 nm, compared to the previously mentioned 2.3 nm for the higher work function devices.

This change in behaviour between the left and right J-V curves from Figure 3.10 is explained by a reduction in the charge carrier accumulation on both sites of the interlayer when the work function is decreased. As discussed in section 3.1, when increasing the MoO_3 work function, the c-Si band bending also increases. Therefore, the energy difference between the Fermi level and the valence band at the a-Si/c-Si interface decreases. This implies a greater hole accumulation on the hole transport layer. This higher hole accumulation facilitates the transport through the SiO_2 interlayer. Therefore, the transport across the hole contact will be more hindered when the work function is 5.5 eV, because of the lower hole accumulation with respect to the 6.3 eV case. This effect is observed in the J-V curves through a lower V_{OC} and an S-shape.

To summarize, in this section two set of solar cells with increasing SiO_2 interlayer thickness have been simulated. The results of the first set of simulations, which employed a MoO_3 work function of 6.3 eV, showed that the SiO_2 interlayer had no detrimental effect on the conversion efficiency as long as its thickness was below 2.3 nm. The second set, which employed a lowered MoO_3 work function of 5.5 eV, displayed S-shapes in the J-V curves for thicknesses greater than 0.8 nm. Therefore, the detrimental effects of the SiO_2 interlayer can be avoided with a MoO_3 work function of 6.3 eV, and an interlayer thickness below 2.3 nm.

This conclusion is novel among literature where solar cells with an interlayer with thickness from 1.6 to 2.5 nm have been fabricated [80]–[82]. These layers are thicker than the charge carrier tunnelling threshold (2 nm) [88] and then the tunnelling limit found in this thesis (≈2.3 nm). This fact suggests that an alternative transport mechanism may be present. [77] claims that the silicon oxide interlayer found in the interface contains a certain amount of oxygen deficiencies. These deficiencies create defect levels inside the material, being able to assist the tunnelling of holes

through the silicon oxide interlayer. Therefore, the charge carriers are able to tunnel energy barriers thicker than the tunnelling limit through trap assisted tunnelling. These traps are not implemented in the simulated solar cells from this work. The holes need to tunnel the SiO_2 interlayer by direct tunnelling, instead of TAT. This is the reason why the thickness limit found in our simulations is thinner than the one reported in literature.

3.2.2 Work function attenuation

Once seen the effects of the SiO_2 interlayer, this subsection focuses on the other phenomenon that occurs at the interface between MoO_3 and a-Si. It has been observed that the TMO work function is decreased close to the a-Si surface, and it has usually been attributed to an interface dipole [10], [81]. This dipole is claimed to reduce band bending at the c-Si surface. The objective of this subsection is to understand the effects that this attenuation in work function has on the performance of the solar cells.

The first step is to know where this attenuation in work function Δ comes from. [77] explored the three contributions to the attenuation, all of them related to the oxygen deficiency of MoO_3:

1. During deposition, the TMO layer is stoichiometric, i.e. MoO_3. All the molybdenum cations are Mo^{6+}. Because of the high reactivity, there will be oxygen deficiency on the layer. As a consequence, some molybdenum atoms will be reduced to Mo^{5+} and Mo^{4+}. This increase of low electronegativity cations results in a decrease of the work function of the material [86].
2. The oxygen vacancies act as n-type dopants, which have energy very close to the Fermi level. When these states ionize, they rise the Fermi level of the MoO_3, decreasing its work function as well [86].
3. At the boundary between different materials, a local separation of charges occurs over a very narrow distance [89]. This is described as an interface dipole. In the case of MoO_3, this dipole is especially important because of the donor states, which are negative trap charges accumulated on the MoO_3 surface [77].

The three contributions are summarised in Equation 3.1:

$$\Delta = \Delta WF_{cation} + \Delta WF_{donor} + \Delta WF_{dipole} \tag{3.1}$$

We are interested in studying the effect that Δ has on the performance of the solar cell. The work function attenuation is implemented through an interface dipole, while neglecting cation and donor components. Therefore, the three components were introduced through the dipole work function attenuation. A dipole layer was placed at MoO_3/a-Si interface, following the simulation approach in [90]. The dipole had the same material characteristics as a-Si. On each of the adjacent surfaces, a fixed interface charge σ_{DP} is placed. The charge concentration is the same on both sides, but opposite in sign.

Depending on which surface the negative charge concentration is, the sign of the dipole is negative or positive. The convention states that ΔWF_{dipole} is positive when the vacuum energy is raised outside of the material [89]. This implies that the dipole moment as a vector points from MoO_3 towards a-Si. In the studied devices, the dipole was found to be negative [10], hence the dipole moment points from a-Si towards the MoO_3 layer. This implies a linear drop in potential energy from the TMO to the passivating layer. In order to achieve this, the negative charge should be located closer to the MoO_3 layer. The configuration of the interface dipole is sketched in Figure 3.11.

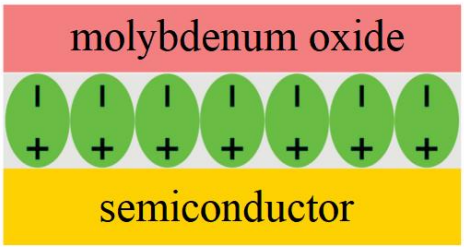

Figure 3.11: Sketch of the interface dipole between the MoO_3 and the neighbouring semiconductor.

The interface charge σ_{DP} determines the interface dipole moment p through Equation 3.3 [89]. Q is the charge of the dipole, which is composed of the elementary charge q multiplied by the interface charge and by the area that each dipole molecule occupies A. The area is assumed to be a square of 0.5 nm × 0.5 nm [90]. d is the thickness of the dipole layer, set to 0.5 nm.

$$p = Q\,d = \; q\,A\,\sigma_{DP}\,d \tag{3.3}$$

Through simulations, the magnitude of the work function attenuation can be calculated for different dipole moments. Figure 3.12 shows the graphical relation between the two magnitudes.

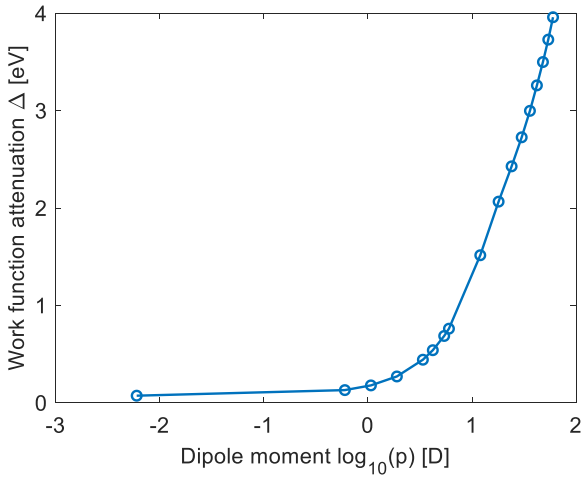

Figure 3.12: Work function attenuation as a function of the dipole moment.

The effect of the work function attenuation was studied by increasing the dipole moment in order to observe the evolution in the solar cell performance. Three different values were simulated: 0.006, 0.6 and 6 D, corresponding to interface charges explored in [90]. The MoO_3 work function was set to 6.3 eV. The J-V curves and corresponding band diagrams for these three devices can be observed in Figure 3.13. The J-V curve of a device without dipole has also been plotted as a reference.

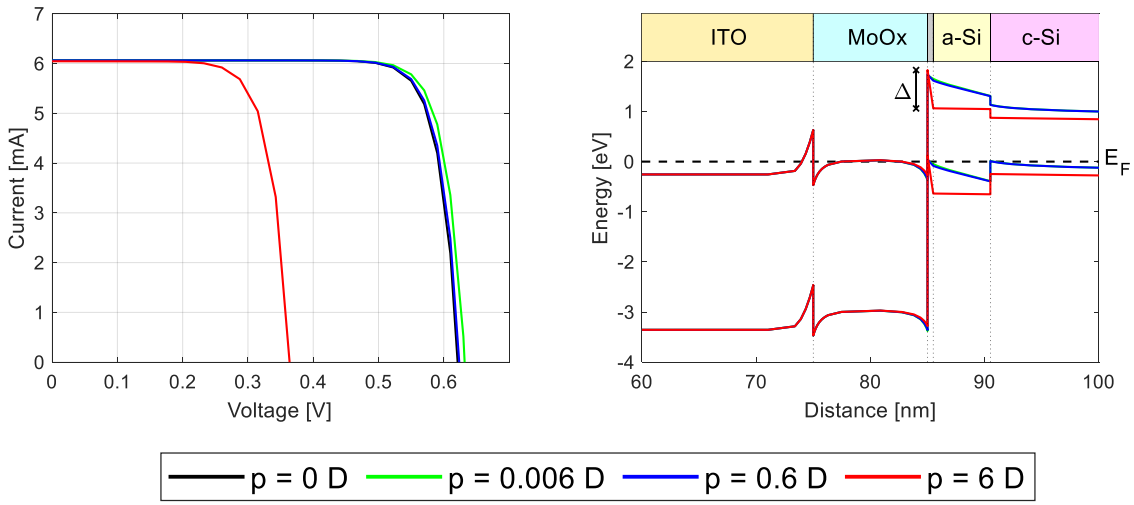

Figure 3.13: J-V curves (left) and band diagram (right) for the solar cells with different dipole moments. The drop across the dipole layer is represented in the band diagram, pointing out the magnitude of the work function attenuation.

As can be observed on the left graph in Figure 3.13, for the two smallest dipole moment values, the J-V curves are basically overlapping. Therefore, for dipole moments smaller than 0.6 D, the dipole has no effect on the J-V curve of the solar cell if the TMO work function is of 6.3 eV. In the corresponding band diagrams from the right graph in Figure 3.13, the energy drop across the dipole layer can be observed. For the two smallest values, it can be seen that the drop is barely noticeable. The band diagrams also show barely no energy difference between the Fermi level and the valence band at the c-Si/a-Si. This implies that the hole accumulation is such that the transport is not affected.

When the dipole moment is increased to 6 D, a significant effect on the J-V curves can be observed. The corresponding band diagram (red curve) shows an energy drop across the dipole of almost 1 eV. This fact reduces the energy band bending of the c-Si, therefore increasing the energy difference between the Fermi level and the valence band at the c-Si interface. This implies that there is a lower accumulation of holes with respect to the previous smaller dipole moments. This fact results in the reduction of the open circuit voltage of the solar cell.

To summarize, in this section, we have presented the three components of the work function attenuation. We have included this attenuation in drift diffusion simulations through an interface dipole. We have observed that for dipole moments smaller than 0.6 D, equivalent to work function attenuations $\Delta \leq 0.1$ eV, there are no detrimental effects on the performance of the solar cell. However, for a dipole moment of 6 D ($\Delta \approx 0.8$ eV) a considerable decrease in open circuit voltage is found. In order to prevent the detrimental phenomena, we should keep $\Delta \leq 0.1$ eV. The next section presents possible strategies on how to achieve this reduction of the work function attenuation components.

3.2.3 Reduction of the work function attenuation

This section focuses on the reduction of Δ. To do so, it is necessary to explore deeper the components of the work function attenuation.

The cation ΔWF_{cation} and donor ΔWF_{donor} attenuations were characterized in [86]. Greiner et al. demonstrate that these two terms depend on the oxygen deficiency (x in MoO_{3-x}), and that they are greater in absolute value as the oxygen deficiency increases. The reduction is caused by the

interactions with the adjacent material [86], hence the first nanometres of deposited material will be more oxygen deficient [41]. As MoO_3 is being deposited, the interfacial reactions will decrease, therefore the material will be more stoichiometric. This relation between oxygen deficiency and TMO thickness makes the cation and donor elements dependent on the thickness of the layer $\Delta WF_{cation}(t)$, $\Delta WF_{donor}(t)$. These components will be smaller for thinner layers than for thicker ones [16].

Since the oxygen reactivity of MoO_3 is high, the attenuation is hardly inevitable. By adding the constant work function of stoichiometric molybdenum trioxide WF_{MoO3} to these two components, a non-stoichiometric MoO_x work function dependent on the thickness of the layer $WF_{MoOx}(t)$ can be defined. This relation is shown in Equation 3.4.

$$WF_{MoOx}(t) = WF_{MoO3} + \Delta WF_{cation}(t) + \Delta WF_{donor}(t) \tag{3.4}$$

The MoO_x work function as a function of thickness has been several times characterized in literature [25], [34], [75], [77], [86], [87]. However, the values obtained differ depending on the study. The reason for this variation is that the degree of reduction of MoO_3 depends on the oxidation potential of the adjacent layer [16]. Therefore, the work function of MoO_x depends on the configuration of the HTL. Moreover, the deposition conditions and the contact with air of the TMO affect its work function [41]. Overall, each solar cell built employing MoO_x as hole transport layer will have a different shape of the work function as a function of thickness. This explains the different values found in literature, illustrated in Figure 3.14.

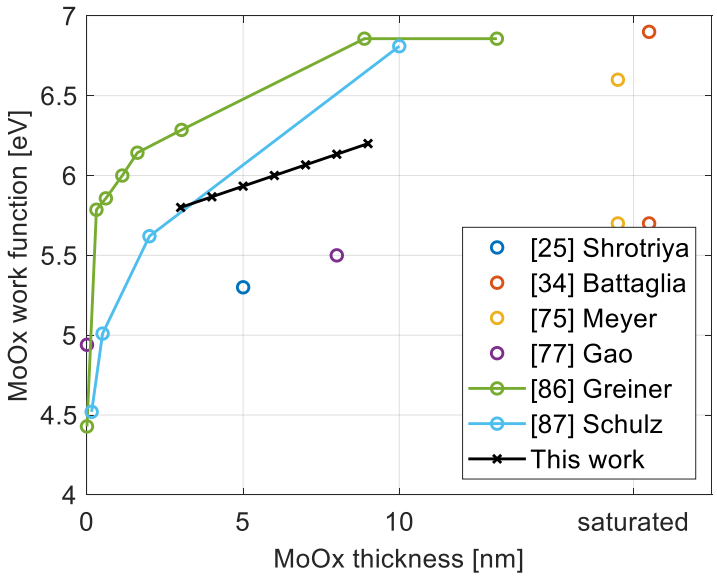

Figure 3.14: Literature values of MoO_x work function as a function of thickness. The values used for the simulations in this work are also represented with black crosses.

The graph in Figure 3.14 shows that the thinner the layers, the smaller the work function. This is because the donor and cation components are greater closer to the interface, because the first nanometres deposited are more oxygen deficient. Overall, the work function attenuation due to the cation and donor components can be reduced by increasing the thickness of the TMO layer.

Regarding the dipole component of the work function attenuation, its relation with the work function of MoO_x can be found in Equation 3.5 [10]. The thickness dependencies for all components have been added to it.

$$WF_{MoOx}(t) - WF_{a-Si} = qV_{bi}(t) - \Delta WF_{dipole}(t) \tag{3.5}$$

In order to be able to reduce the dipole attenuation, we need to understand this equation and the dependency with TMO thickness of its components.

The dependency of the MoO_x work function $WF_{MoOx}(t)$ with thickness is sketched in Figure 3.14; an increase in work function as the layer thickens. WF_{a-Si} does not depend on the thickness of the TMO. The built-in voltage $V_{bi}(t)$ will have the same dependency with the TMO thickness as $WF_{MoOx}(t)$, until a maximum built-in voltage is reached $V_{bi,max}$. The built-in voltage has a maximum limit because the energy bands cannot bend indefinitely [82]. Once that limit is reached, if the work function of the TMO increases, an interface dipole appears $\Delta WF_{dipole}(t)$.

Three cases can be found in Equation 3.5 as a function of the TMO thickness, which are graphically distinguished in Figure 3.15. For thin layers, the built-in voltage will have the same thickness dependency as $WF_{MoOx}(t)$ and will increase as the layer thickens. At a certain thickness t_{opt}, the built-in voltage will reach its maximum $V_{bi,max}$. From that thickness on, the built-in voltage will be constant, and an interface dipole will be formed at the interface $\Delta WF_{dipole}(t)$. The three cases can be distinguished in Equation 3.6.

$$WF_{MoOx}(t) - WF_{a-Si} = \begin{cases} qV_{bi}(t), & t < t_{opt} \\ qV_{bi,max}, & t = t_{opt} \\ qV_{bi,max} - \Delta WF_{dipole}(t), & t > t_{opt} \end{cases} \tag{3.6}$$

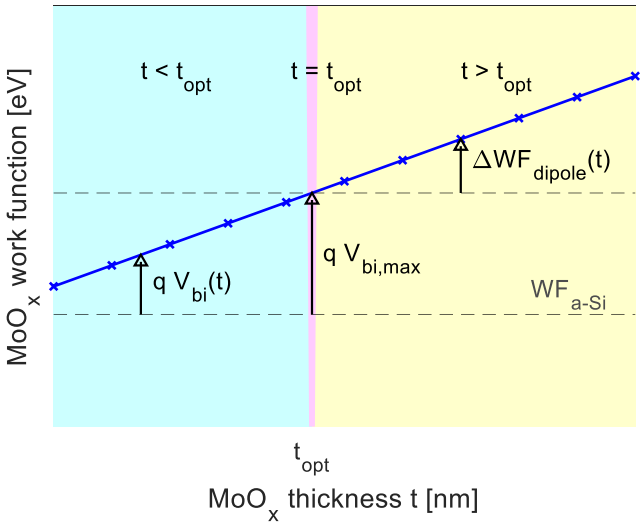

Figure 3.15: Graphical explanation of Equation 3.6 where the three cases can be distinguished.

This equation was numerically implemented in order to study realistically what is the effect of the MoO_x thickness variation. A set of devices was simulated with increasing TMO thickness. For each thickness, the work function and dipole moment were tuned following Equation 3.6. This tuning is illustrated in Figure 3.16.

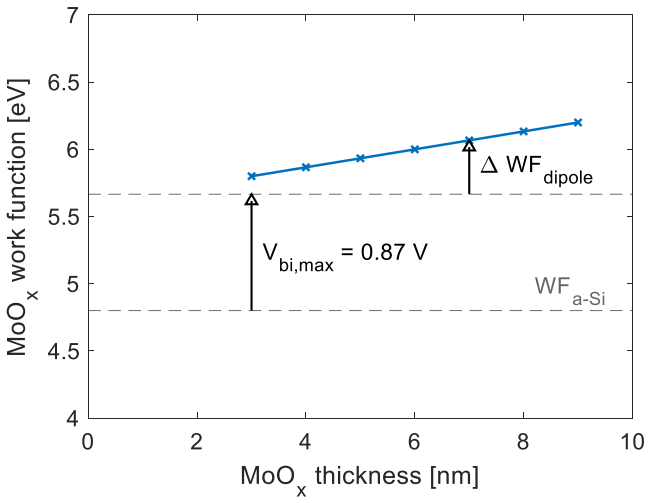

Figure 3.16: Graphical determination of $\Delta WF_{dipole}(t)$ for the chosen $WF_{MoOx}(t)$ in this work.

There are some unknowns in this equation. First of all, $WF_{MoOx}(t)$ has shown a great variation in Figure 3.14. The values chosen for the simulation are sketched in Figure 3.14 in black crosses, and in Figure 3.16. WF_{a-Si} was calculated from the simulations to be 4.8 eV. $V_{bi,max}$ was found to be 0.87 V, the limit value for which c-Si is a non-degenerate semiconductor. Finally, $\Delta WF_{dipole}(t)$ was determined by Equation 3.6, and tuned through the dipole moment.

Considering the chosen $WF_{MoOx}(t)$, it can be observed from Figure 3.16 that for all thicknesses, the band bending has reached its theoretical maximum, $V_{bi,max}$. Therefore, as the transition metal oxide layer thickens, the dipole moment will increase. This simulation corresponds to the third case of Equation 3.6, $t > t_{opt}$ (see Figure 3.15). The results of open circuit voltage and fill factor as a function of thickness for this set of devices are shown in Figure 3.17.

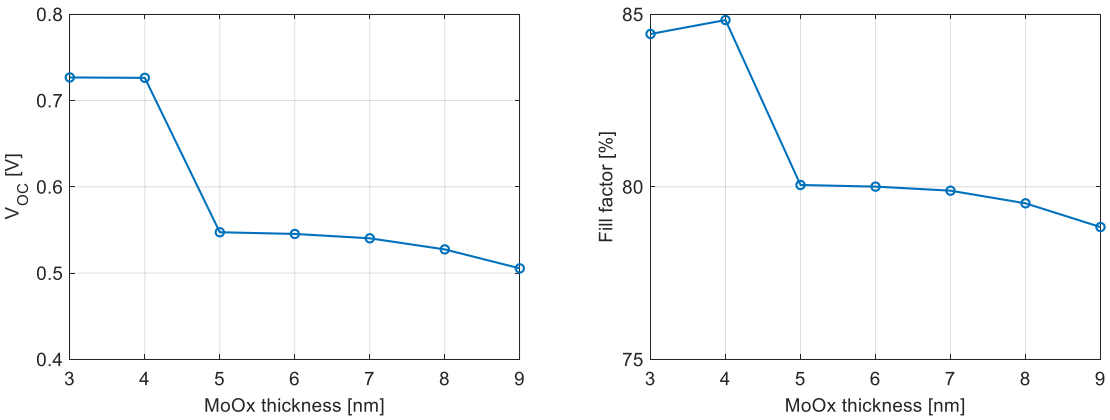

Figure 3.17: Open circuit voltage and fill factor as a function of MoO_x thickness with the dipole implemented.

The open circuit voltage and fill factor graphs show that there is a decrease in performance as the MoO_x thickens. This is attributed to the just mentioned increase in dipole moment with the TMO thickness, which results in a lower performance as explained in section 3.2.2.

In this curve, the sudden drop in open circuit voltage and fill factor between 4 and 5 nm is an artefact of the simulation motivated by a sudden increase in electric field. This fact creates a suddenly larger leakage current of electrons from a-Si to MoO_x. This circumstance is out of the scope of this thesis, therefore its effect is not studied.

3.2.4 SiO_2 and dipole

Once explored the impact of the dipole and the SiO_2 interlayer, the next step is to observe the effect of the two events together. They are both likely to occur in fabricated devices, hence they should be evaluated if we want to obtain realistic trends from fabricated devices.

The set of simulations from this section consists on solar cell devices including both a silicon dioxide interlayer and an interface dipole. The location of the dipole was set in the SiO_2/a-Si interface, since according to literature the dipole layer is on the silicon surface [32], [81]. The TMO thickness for these devices was increased as before, consequently tuning the MoO_x work function and the dipole moment. The set of solar cells were simulated under two different SiO_2 thicknesses, 1.5 and 1.8 nm, in order to analyse the effect that the SiO_2 interlayer has on the open circuit voltage and fill factor, following the approach from section 3.2.1. These two electrical parameters can be observed in Figure 3.18. The characteristics for the devices without SiO_2 interlayer are also plotted as reference.

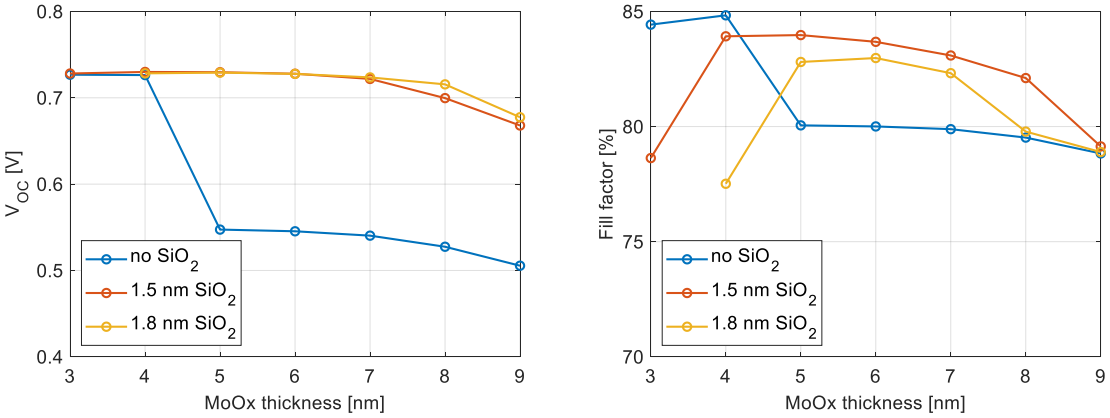

Figure 3.18: Open circuit voltage (left) and fill factor (right) of the solar cells with dipole and different SiO_2 thicknesses as a function of MoO_x thickness.

Aa summary, the effect of MoO_x thickness before analysing the trends from Figure 3.18. The increase in TMO thickness has two effects, a positive and a negative one. First, an increase in work function. As explained in section 3.1, a higher work function is beneficial because the energy difference between the MoO_3 conduction band and a-Si valence band decreases. Second, an increase in dipole moment. The drop in energy across the dipole interlayer increases with the dipole moment. As seen in the band diagram in Figure 3.13, a higher energy drop results in a lower hole accumulation in c-Si/a-Si interface, therefore a lower performance.

The open circuit voltage, left graph in Figure 3.18, slowly decreases as the MoO_x layer thickens. This decrease is due to the higher effect of the dipole moment, as explained in section 3.2.2. Figure 3.13 shows a drop in open circuit voltage with the increase in dipole moment.

The fill factor, right graph in Figure 3.18, experiences a bell shape, which represents the trade-off between an increase in work function, and an increase in dipole as the TMO layer thickens. For thin layers (3-4 nm), the work function is low. The transport is hindered because of the high energy difference between the MoO_3 conduction band and a-Si valence band, section 3.1. For thick layers (7-9 nm) the transport is hindered because of the low hole accumulation due to the increase in dipole moment (section 3.2.2). This lower hole accumulation at c-Si/a-Si interface, hinders the tunnelling across the SiO_2 interlayer, as explained in section 3.2.1, reducing the fill factor. The trade-off between a low work function and a high dipole moment is found for thicknesses around 5-6 nm. The optimum thickness t_{opt} for this set of devices is within that range.

Comparing the simulations with and without interlayer, the drop in V_{OC} and FF between 4 and 5 nm thicknesses does not occur anymore. The addition of the SiO_2 interlayer creates a barrier for the electrons at the a-Si surface, blocking the leakage current that decreases the performance.

It is necessary to stress that the results obtained here strongly depend on the dependency of the MoO_x work function with thickness. A different $WF_{MoOx}(t)$ may yield distinct trends and a new optimum TMO thickness. For this study, $WF_{MoOx}(t)$ is set as Figure 3.16, in order to obtain similar trends to the ones reported in fabricated devices [33] [81].

3.3 Maximizing the conversion efficiency

The objective of this section is to provide guidelines to the fabrication process of MoO_x SHJ solar cells in order to improve the conversion efficiency. To do so, the model developed in the previous section will be used to reproduce the values obtained for state-of-the-art solar cells. Later a brief study on light management for these devices is performed. Finally, this section ends by enumerating the guidelines towards the maximum performance.

3.3.1 State of the art trends

The highest efficiency on MoO_3 SHJ solar cells so far of 23.5% was recently achieved by Dréon [33]. There, a study on the effect of the thickness of the MoO_3 and of the passivating a-Si layers is done. The best performance is obtained for a solar cell with 4 nm of MoO_3 and 6 nm of a-Si passivating layer. This subsection will simulate these structures in order to highlight crucial steps during the fabrication of solar cells.

In order to perform a realistic fitting, the simulated solar cells include the dipole together with 2 nm of SiO_2 interlayer. The thickness of the front TCO was reduced to 70 nm, and the passivating amorphous silicon layer was increased to 6 nm. The TMO thickness was set to 4, 6 or 9 nm depending on the simulated solar cell. The MoO_x work function and dipole moment were tuned to mimic the measured open circuit voltage and fill factor. The rest of material characteristics and thicknesses remained as stated in the previous section.

The fitted devices were the ones with 6 nm thickness of a-Si and TMO thickness of 4, 6 and 9 nm. Additionally, the best solar cell fabricated in the study was included. The results are shown in Table 3.6. For each device, the first row in italics represents the measured open circuit voltage and fill factor, while the second one shows the best fitting obtained. The fitting values coincide with a percentage deviation of maximum 1.1%.

Table 3.6: Characteristics of the solar cells fabricated by Dréon [33] *and their fittings.*

MoO_3 thickness		***WF_{MoO3}* [eV]**	**Δ [eV]**	**p[D]**	**V_{oc} [mV]**	**FF [%]**
4 nm (best cell)	Experimental	--	--	--	734	81.8
	Fitting	5.93	0.06	0.4	732	81.8
4 nm (average)	Experimental	--	--	--	725	78.9
	Fitting	5.87	0.23	1.8	722	78.6
6 nm (average)	Experimental	--	--	--	726	79.0
	Fitting	5.89	0.23	1.8	726	79.6
9 nm (average)	Experimental	--	--	--	724	78.0
	Fitting	5.90	0.32	2.5	716	78.3

Focusing first on the average solar cells, the results are the expected ones. An increase in both work function and dipole moment is observed, which is in concordance with the previous section. The high work function value, which is barely negligible to the thickness variation, shows an excellent treatment of the TMO layer.

For the best solar cell, an improvement in both the work function and dipole moment can be observed. The best solar cell achieves a high work function for a thin layer, the main key characteristics to a great performance, as has been repeated along this work. Moreover the dipole moment is smaller than 0.6 D, which was shown in section 3.2.2 to have no effect on the performance of the solar cell. This boost in improvement could indicate that the best solar cell does not follow the same processing as the average ones.

A difference between these fittings and the fabricated solar cells is the interlayer width. The STEM image performed in [33] shows an amorphous silicon oxide layer of thickness greater than 2 nm. As already mentioned in section 3.2.1, the thicker oxide layer than the tunnelling limit is explained by the amorphous character of the layer, which inserts gap states which help the transport.

3.3.2 Light management

This section explores light management in SHJ MoO_3 solar cells. The solar cells simulated in this section include a textured bulk and front top layers, in order to mimic fabricated devices. The objective of texturing is to enhance the coupling of light. The parameter that is mostly affected by this technique is the short circuit current.

The simulation of a textured solar cell is a highly computationally expensive process. Simulations with several front layers yield many convergence problems. However, not considering texturization may dismiss the obtained short circuit current. For that reason, this subsection explains how the current is affected by the thickness of the different front layer parameters. Although these results refer to a specific device, the trend obtained is general for all the previously simulated solar cells.

The simulated device has the structure of Figure 2.4, but with the top layers texturized. Simulation details on the texturization approach can be found in [91]. The pitch and bulk thickness are reduced to 100 and 200 µm respectively in order to decrease the computational time. The width of the top TCO was kept to 70 nm, as in the previous simulation, while the thicknesses of the other two front layers, MoO_3 and a-Si, were varied. The rest of parameters were left unaltered. The short circuit current density (J_{SC}) results can be observed in Figure 3.19.

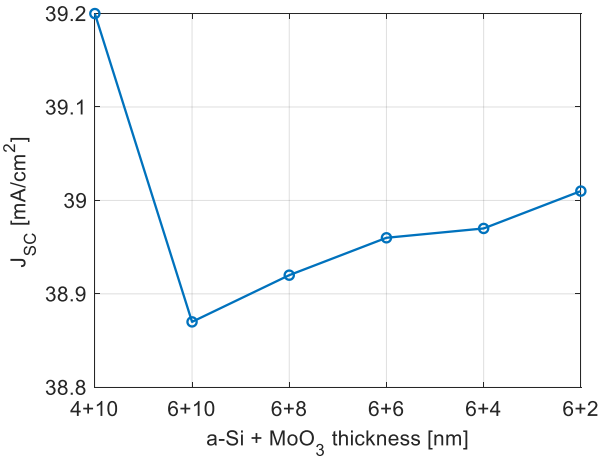

Figure 3.19: Short circuit current of textured solar cells under different front layer thicknesses.

The thinner the front layers are, the higher is the current density. This improvement on current is different for MoO_3 layers than for amorphous silicon ones. The highest possible short circuit current is achieved with 10 nm of TMO and 4 nm of a-Si. If the thickness of the passivating layer is increased by only 2 nm, a considerable drop of 0.34 mA/cm^2 can be observed. On the other hand, a reduction of MoO_3 thickness by 2 nm, results in a maximum gain in photocurrent of 0.07 mA/cm^2, almost 5 times smaller than the rise when the a-Si layer is reduced by the same width. It is not possible to recover the initial short circuit current value by only decreasing the thickness of the oxide layer.

This phenomenon is due to the difference in energy band gaps between materials: 3 eV for the transition metal oxide and 1.7 eV for the passivating layer. Here the advantage of the use of transition metal oxides with respect to amorphous silicon layers can be appreciated. However, the MoO_3 layer still suffers from parasitic absorption due to the defect states [81].

This trend is in concordance with the one shown in [33]. Although in those solar cells two additional layers were a part of the front HTL, these are very thin (0.5 nm for the dipole), or with high energy band gap, hence low absorption (9 eV for the SiO_2 interlayer). Therefore, it is possible to extrapolate the results with small relative error.

3.3.3 Towards the maximum performance

The objective of this subsection is to provide guidelines for the fabrication of the studied solar cells. From the simulations performed in this chapter, several key points can be extracted.

- From the SiO_2 study performed in subsection 3.2.1, it has been shown that the interlayer can have a beneficial effect if its thickness is kept under 2 nm and the MoO_3 work function is around 6.3 eV. Although it has also been stated that in fabricated devices the composition of this interlayer is not the same as the one simulated here, these results may still be valid.
- In subsection 3.2.4, we have observed a trade-off between an increase in work function, and an increase in dipole moment as the TMO layer thickens. Thin layers result in low work functions, while thick layers result in high dipole moments. The recommendation is to keep the thickness of the TMO layer within 5 to 6 nm, which shows the best trade-off between the two phenomena.
- The work function attenuation could also be reduced by lowering the cation and donor components. These two contributions are related to the oxygen reduction of MoO_3. Therefore, in order to lower the cation and donor components, it is necessary to avoid the reduction of the oxide. [92] showed that it can be achieved by depositing a thin layer of non-reactive material between the MoO_3 and the passivating layer, such as gold. In order to test its effect, the devices should be fabricated.
- An alternative to the thin layer of gold would be to realize an interface treatment to prevent the reduction of the TMO. The objective would be to achieve a negligible interface dipole while keeping a high work function.
- Regarding light management considerations, the thinner the passivating layer is, the better. However, in practice this statement is not so straight forward since there is a minimum a-Si thickness above which good junction properties are assured [93].

All these points can be used for fabrication groups in order to improve the performance of the solar cells in study. Proper simulation of all these phenomena by Sentaurus is challenging, but an estimation of the photovoltaic parameters can be performed assuming ideal conditions.

The highest performance was achieved by a solar cell with 4 nm thickness of MoO_3 and a-Si, with no dipole, 2 nm of SiO_2, and a TMO work function of 6.3 eV. The remaining parameters and

thicknesses were left unaltered. Under those conditions, the flat device yielded an open circuit voltage and fill factor of 732 mV and 84.5%, respectively. The short circuit current was extracted from textured simulations, assuming that the just mentioned photovoltaic parameters are unaltered by texturing. The combination of layer thicknesses resulted in a short circuit current of 39.3 mA/cm^2. With these three values, the efficiency of the solar cell was of 24.3 %.

Table 3.7 shows the comparison of those values with the record SHJ solar cell both-side-contacted [1].

Table 3.7: Comparison between the best fabricated SHJ solar cell with the best simulated solar cell in this work.

	J_{SC} [mA/cm^2]	V_{OC} [mV]	FF [%]	Efficiency [%]
This work	39.3	732	84.5	24.3
Adachi et al. [1]	40.8	738	83.5	25.1

The short circuit current could be further increased by optimizing the ITO thickness. Considering the refractive indexes, an optimum thickness for the TCO which decreases the front reflectance can be found. The electron transport layer at the back has not been optimized either, where some parasitic absorption and transmittance may be avoided.

The open circuit voltage and fill factor are very similar. Considering that they are highly dependent on each other, increasing one parameter will most likely come at expense of decreasing the other one. There may still be some room for improvement in the electron transport layer, but it is not considered because it is not the subject of this work.

To summarise, if all the improvements proposed here were achieved in a fabricated device, the result would be a competitive solar cell with SHJ counterpart.

3.4 Nature of dipole

Even though it is known that the appearance of the dipole is due to the interfacial reactions that occur on the a-Si/MoO_3 interface, the exact reason why it happens is not clear. In order to know it, it is necessary to understand all the interactions, chemical bonding and charge rearrangement occurring between two materials.

All this information is stored in the quantum wave functions [94]. To obtain them, the Schrödinger equation needs to be solved, since it contains all the information of a given system. This equation can be solved exactly for a quantum well or hydrogen atom, but it already becomes extremely complex when solving a very small atom such as lithium. For a N-body system, such as the one obtained in the a-Si/MoO_3 interface, the Schrödinger equation turns to be intractable.

Approximations need to be done if the interface between materials is to be studied. Here arises the need of density functional theory (DFT), a computational method for obtaining an approximate solution to the Schrödinger equation of a many body system. The fundamentals of this method as well as the computational details will be discussed in Chapter 4.

4 Atomistic background

As already mentioned in the last chapter, density functional theory (DFT) is a computational method that approximately provides a solution of Schrödinger equation. This chapter is structured as follows. Section 4.1 explains briefly the fundamentals of DFT. Section 4.2 shows details about the computational implementation of these fundaments in the numerical tool. The next section 4.3 explains approaches on how to model surfaces and interfaces in *ab initio* calculations. Finally, section 4.4 introduces the crystalline structures of the simulated materials.

Note that all the formulas in this chapter are in atomic units.

4.1 Density functional theory fundamentals

Density functional theory (DFT) is a computational modelling method with the purpose of investigating the electronic structure of many-body systems [95]. The main objective is to compute the wave function, which contains all the relevant information of a quantum system. To do so, it solves approximately the Schrödinger equation, which is otherwise unsolvable. It is the most widely applied *ab initio* method used for real materials in physics, chemistry and materials science.

Although it is an estimated method, very good approximations are known which work well for many systems [96]. This procedure allows to provide a reasonable balance between computational efficiency and accuracy.

As stated above, the objective of density functional theory is to be able to solve the Schrödinger equation for a many-body problem. Such a problem usually represents a material, which is mainly composed of electrons with positions $\vec{r}_n$, and ions that form the lattice, located on $\vec{R}_n$. The Schrödinger equation of this system is [95]:

$$i\frac{\partial}{\partial t}\phi = \hat{H}\phi \tag{4.1}$$

Where $i = \sqrt{-1}$, $\hat{H}$ is the Hamiltonian of the system, and $\phi = \phi(\vec{r}_1, \vec{r}_2, \dots; \vec{R}_1, \vec{R}_2, \dots; t)$ is the wave function. The wave function (ϕ) is a function of the coordinates of all the electrons and ions and dependent on time (t). By simplification of notation, it is represented as:

$$\phi = \phi(\vec{r}_1, \vec{r}_2, \dots; \vec{R}_1, \vec{R}_2, \dots; t) = \phi(\vec{r}, \vec{R}; t) \tag{4.2}$$

The Hamiltonian of the system is made of nuclear (R sub index), electronic (r) and mixed (r, R) kinetic ($\hat{T}$) and potential ($\hat{V}$) terms:

$$\hat{H} = \hat{T}_R + \hat{T}_r + \hat{V}_R + \hat{V}_r + \hat{V}_{r,R} \tag{4.3}$$

The solution of Schrödinger equation is analytical only for simple systems such as a hydrogen molecule or a quantum well. In order to present a solution for complex molecules, numerical approximations are typically used.

4.1.1 Born-Oppenheimer approximation

The Born-Oppenheimer approximation [97] allows to separate the abovementioned problem into two independent ones: (i) one for the electrons and (ii) one for the ions of the lattice. This is motivated by the great difference in mass between the nuclei and the electrons, exceeded by a factor of 1000 or more [98]. This implies that the kinetics of the electrons are substantially faster than those of the nuclei. Therefore, from an electron's point of view, the nuclei is static, simplifying significantly the electronic Hamiltonian.

From that point of view, the many-body wave function ϕ of the system can be separated into nuclear wave function components $\chi_n(\vec{R};t)$, and electronic wave functions $\psi_n(\vec{r},\vec{R})$ [95]:

$$\phi(\vec{r},\vec{R};t) = \sum_n \chi_n(\vec{R};t)\psi_n(\vec{r},\vec{R}) \tag{4.4}$$

This wave function is inserted into the Schrödinger equation and projected onto the electronic basis of one electron $\psi_m(\vec{r},\vec{R})$. Until now, no approximations have been done and this is valid for all general cases. The next step performs the first two: neglect the cross terms that appear, and choose the adiabatic representation, where the electronic wave function depends only parametrically on the nuclear positions: $\psi_m(\vec{r},\vec{R}) = \psi_m(\vec{r};\vec{R})$. Applying these two facts, the equations for the electronic and ionic basis can be separated into:

1. Electron-structure problem: regard the nuclei as fixed in space and solve for the electronic degrees of freedom.

$$\hat{H}_e\psi_m(\vec{r};\vec{R}) = \epsilon_m(\vec{R})\psi_m(\vec{r};\vec{R}) \tag{4.5a}$$

$$\hat{H}_e = \hat{T}_r + \hat{V}_r + \hat{V}_{r;R} \tag{4.5b}$$

2. Nuclear problem: solve for the ionic degrees of freedom.

$$i\frac{\partial}{\partial t}\chi_m(\vec{R};t) = [\hat{T}_R + \hat{V}_R + \epsilon_m(\vec{R})]\chi_m(\vec{R};t) \tag{4.6}$$

Through this separation, the ion-ion interaction can be solved classically. All terms are known, but not the electronic energy $\epsilon_m(\vec{R})$, requiring the electronic problem to be solved first. Therefore, from now on the focus will be shifted to only the electronic wave functions, $\psi_m(\vec{r};\vec{R}) = \psi_m(\vec{r})$.

4.1.2 Hohenberg-Kohn theorems

The Hohenberg-Kohn theorems [99] reformulate the many-body problem in terms of the density, but do not actually solve it [95]. When doing this, the dimensionality is reduced from 3N for $\psi_m(\vec{r})$ (being N the number of electrons in the system) to 3 for the ground state density $n_0(\vec{r})$. The two theorems are:

1. For any electronic system in an external potential $v_{ext}(\vec{r})$, the ground state density $n_0(\vec{r})$ determines uniquely the external potential safe for a constant [96].

Once known the ground state density and the external potential, the Hamiltonian of the system can be found. In particular, the functional of the energy $E[n(\vec{r})]$, where n is the electronic density. With it, the wave function for all states can be determined, which in turn allows to define the properties of the system.

$n_0(\vec{r}) \longrightarrow v_{ext}(\vec{r})$ (except for a constant)

$\longrightarrow$ All properties

The ground state density represents the ground state wave function $\psi_0(\vec{r})$, which is the state with the lowest energy. Density functional theory is a ground state theory.

The external potential is generally the potential felt by the electrons which is formed by the nuclei with atomic number Z_n, although it can include additional terms.

$$v_{ext}(\vec{r}) = -\sum_n \frac{Z_n}{\vec{r} - \vec{R}_I} \tag{4.7}$$

2. The ground state density $n_0(\vec{r})$ is determined by the global minimum value of the energy functional $E_0[n_0(\vec{r})]$.

$$E_0[n_0(\vec{r})] = \min_{n(\vec{r})} E[n(\vec{r})] \tag{4.8}$$

Therefore, the functional $E[n]$ alone is sufficient to determine the exact ground state energy and density. Excited states must be determined by other means.

In summary, the first theorem states that the ground state density alone determines the properties of the system, while the second one explains how to obtain the ground state energy and density.

For convenience, the energy functional is divided into a universal and a system dependent part:

$$E[n(\vec{r})] = F[n(\vec{r})] + \int v_{ext}(\vec{r}) n(\vec{r}) d\vec{r} \tag{4.9}$$

The universal functional $F[n(\vec{r})]$ contains the individual contributions of kinetic energy $T[n(\vec{r})]$, classical Coulomb interaction, and the non-classical self-interaction correction E_{xc}^{true}:

$$F[n(\vec{r})] = T[n(\vec{r})] + \frac{1}{2}\iint \frac{n(\vec{r}) n(\vec{r}')}{|\vec{r} - \vec{r}'|} d\vec{r} d\vec{r}' + E_{xc}^{true} \tag{4.10}$$

This functional is an unknown due to the self-interaction correction term, but depends only on the electron density. Therefore by knowing the electron density and the external potential, the whole system is defined.

Although the Hohenberg-Kohn theorems are extremely powerful, they do not offer a way of computing the ground-state density of a system in practice. To do so, the Kohn-Sham equations need to be applied.

4.1.3 Kohn-Sham equations

The Kohn-Sham equations [100] replace the original many-body problem with an auxiliary system of non-interacting particles. The main assumption is that the ground state density of an interacting system is equal to that of some non-interacting system that is exactly soluble [95]. All the difficult parts (exchange and correlation E_{xc}^{true}) are included in some approximate functional of density. This non-interacting system considers the electrons as independent particles moving in an effective potential, rather than the interaction of the electron with all the other electrons. This effect is illustrated in Figure 4.1. Although the wave-functions are approximate, as long as the ground state density and energy are the same as the exact ones, the approximation is valid.

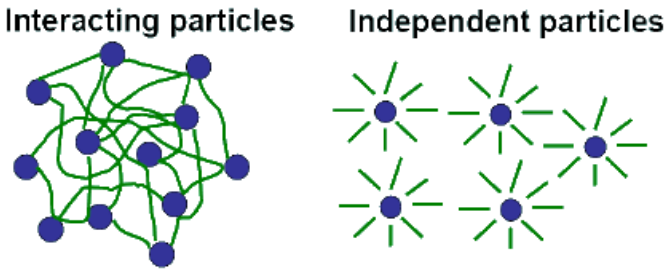

Figure 4.1: Graphical representation of the main assumption performed by the Kohn-Sham equations, from [95].

These equations provide a practical determination of the ground-state density of the system. Therefore, the solution of the independent Kohn-Sham problem determines all properties of the full many-body system.

The Kohn-Sham decomposition allows to compute the contributions separately, simplifying the energy calculation. The kinetic and coulombic energies need to be evaluated on a high accuracy, while the exchange-correlation energy is the hardest to obtain and represents a minor factor of the total energy. The decomposition allows a different degree of accuracy for each component, reducing the difficulty of the problem without a high precision loss.

More information about density functional theory and the equations presented in this section can be found elsewhere [101].

4.2 Implementation

In practice, the Kohn-Sham equations need to be solved iteratively [95]. The functionals of the system depend on the electron density, which determine the electronic wave functions. In turn, the electron density is related to the electronic wave functions by:

$$n(\vec{r}) = \sum_{i}^{occ} |\psi_i(\vec{r})|^2 \tag{4.11}$$

Therefore, in order to solve the system, an initial guess of the “input” charge density needs to be done. It is often achieved by overlapping atomic charge densities. With this initial charge density, the Kohn-Sham equation needs to be solved in order to find the one electron orbitals $\psi_i(\vec{r})$ (also called Kohn-Sham orbitals):

$$\left(-\frac{1}{2}\nabla^2 + v_{ext}(\vec{r}) + v_H(\vec{r}) + v_{xc}(\vec{r})\right)\psi_i(\vec{r}) = \varepsilon_i\psi_i(\vec{r}) \tag{4.12}$$

The first term in the parenthesis represents the kinetic energy, where ∇^2 is the Laplacian. ε_i is the Kohn-Sham eigen-energy. $v(\vec{r})$ are the potentials, where the sub-indexes indicate the external potential (ext), the classical Coulomb interaction (H), and the exchange correlation potential (xc). These potentials are related to their equivalent functionals through:

$$v_{xc}(\vec{r}) = \frac{\delta\varepsilon_{xc}}{\delta n} \qquad E_{xc}[n] = \int \varepsilon_{xc}[n(\vec{r})]\, n(\vec{r})\, d\vec{r} \tag{4.13}$$

Once the Kohn-Sham orbitals are determined, the electron density is computed from Equation 4.11. If the difference between the original charge density and the obtained one is smaller than a

certain threshold, the solution is considered correct and the properties of the system are determined. But if the similarity between the two densities is not high, the steps are repeated until the difference is smaller than the threshold. The flowchart in Figure 4.2 shows these steps in a graphical manner.

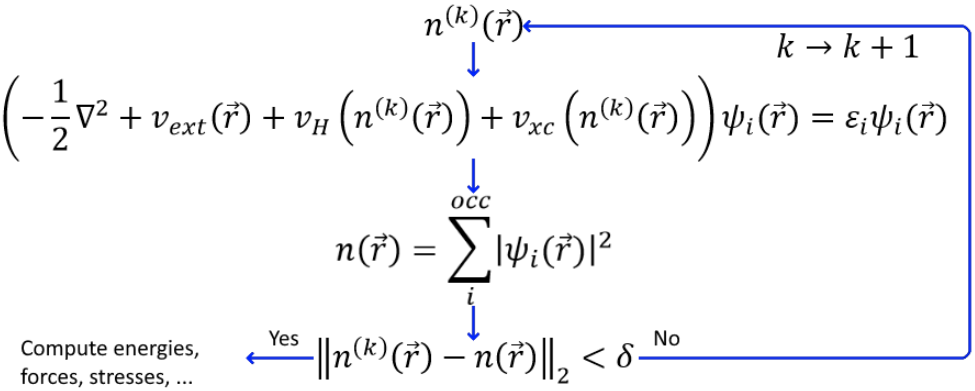

Figure 4.2: Flowchart of the iterative solution of the Kohn-Sham orbitals, based on the diagram by [95].

It is tempting to treat the Kohn-Sham states $\psi_i(\vec{r})$ as proper electronic particle states, but remember that they are fictitious.

4.2.1 VASP

The program employed in this thesis to iteratively solve the Kohn-Sham equations is the Vienna *Ab initio* Simulation Package (VASP) [102], [103]. The system structure and the calculations performed during the simulations are inputted through four files: POSCAR, INCAR, KPOINTS and POTCAR. The main output file is OUTCAR, which contains information on stress tensors, forces on the atoms, local charges, magnetic moments and dielectric properties. Further output files can be created if required with additional system information.

The POSCAR file contains the lattice geometry and ionic positions of the system. It requires the lattice vectors that determine the unit cell, as well as the coordinates of each atom inside the cell.

INCAR is the central input file of VASP. It determines "what to do and how to do it" [104]. The chosen approximation of the exchange correlation potential is also specified in this file (see subsection 4.2.3). Depending on the combination of functions used, it can perform structural optimization, calculate the density of states, band structure, etc.

The KPOINTS file forms the k-point mesh: a finite number of points in the Brillouin zone (BZ). In periodic systems, they are used to replace the integrals in real space by integrals over the first Brillouin zone in reciprocal space. This mesh can be defined manually or automatically. All the simulations in this project are performed using the automatic Monkhorst-Pack [105], which homogeneously distributes the k-points in the BZ, running parallel to the reciprocal lattice vectors. The k-points need to be differently defined on the calculations for the band structure, since all the points of the Brillouin need to be inserted.

Lastly, POTCAR files contain the pseudopotential for each atomic species used in the calculation. There are different versions depending on the pseudopotentials available (section 4.2.3).

Deeper information about these files and how the program works can be found in the VASP manual [104].

4.2.2 Computational details

During the computation of *ab initio* simulations, there are two very important parameters to be defined by the user: the k-points mesh and the cut-off energy.

The wave functions in a crystal obey Bloch's theorem [98]. This theorem states that the eigenfunctions of an electron in a perfectly periodic potential have the shape of plane waves modulated by a Bloch factor $u_i(\vec{r})$. This factor possesses the periodicity of the potential $u_i(\vec{r}+\vec{R}) = u_i(\vec{r})$, where $\vec{R}$ is any linear combination of the lattice vectors of the crystal. This theorem is applicable to the Kohn-Sham states $\psi_i(\vec{r})$:

$$\psi_i(\vec{r}) = e^{-i\vec{k}\vec{r}} u_i(\vec{r}) \tag{4.14}$$

Here $\vec{k}$ are the wave vectors of the reciprocal crystal lattice. They are related to the periodic special lattice through Fourier transform. All these wave vectors are contained in the first Brillouin zone (1BZ), a volume within this space that contains all the unique k-vectors that represent the periodicity of the crystal.

The evaluation of many key quantities such as the charge density, requires integration over the 1BZ. Since the Bloch factor is periodic and the integrals are generally computationally costly, this integral is replaced by a sum over a finite number of k-points. The higher number of k-points, the better the accuracy, but also the computational time. Therefore, the amount of k-points is related to the convergence and accuracy of the results.

For ease of calculations, and since the Bloch factor is periodic, the wave function is expanded using a truncated Fourier series [98].

$$\psi_i(\vec{r}) = \sum_{\vec{G}} u_i(\vec{G})\, e^{-i(\vec{G}+\vec{k})\vec{r}} \tag{4.15}$$

In practice, this series is truncated to include all $\vec{G}$ for which:

$$\frac{\hbar}{2m}\left(\vec{G}+\vec{k}\right)^2 < E_{cut} \tag{4.16}$$

Here the second parameter needed to check for convergence appears: the plane-wave cut-off energy E_{cut}. As well as with the number of k-points, the greater the cut-off energy, the higher the accuracy, but also the computational time.

4.2.3 Approximations

As already defined, the external potential $v_{ext}(\vec{r})$ is formed by the nuclei of the lattice and represents what the electrons observe. The electrons can be distinguished into two groups. The core electrons, which are strongly bound to the nuclei, and the valence electrons, which determine most of the properties of the material [96]. The external potential is singular at the ion core. Close to these points, the wave functions oscillate rapidly. These oscillations require a high computational power and do not alter the main properties. This is the reason why the exact external potential is usually replaced by an approximated one. There are several methods available to solve this issue [98].

The external potential approximation employed in this work for all simulated atoms is the Projector Augmented Wave (PAW) method [106]. The approach consists on smoothing these rapidly oscillating wave functions around the ion cores in order not to have singular points and reduce

the amount of plane waves required. The core electrons are removed from the problem, so the Kohn-Sham equations are only solved for the valence electrons [101].

The potential for each of the elements of the periodic table is supplied by VASP [106], [107]. For some elements several PAW versions exist [104]. In this work, we have employed the recommended versions: standard for Si and O, and sv for Mo. The sv extension implies that the s semi-core states are treated as valence states.

Although DFT is formally precise, the exact functional is unknown. The source of difficulty is the exchange correlation functional. This functional considers the difference between the classical and quantum mechanical repulsion between electrons. It demands high computational effort, therefore it needs to be approximated.

There are several approximations available for the exchange correlation functional. The most common and oldest one is the Local Density Approximation (LDA) [99]. It assumes the same exchange-correlation energy as that of a homogeneous electron gas of density n [98]. This results in over- and under-estimations, although they tend to compensate each other [108].

The approach can be further improved by considering also the gradient of the density, not only its value [109]. This considers non-homogeneity and allows corrections based on non-local density changes. These expansions are referred to as generalized gradient approximations (GGA) [110]. Inside this group, there are several options available.

One of these improved extensions is the PBE functional. The initials stand for the three scientists that parametrized it: Perdew, Burke and Ernzerhof [111]. It is the functional employed in this work for silicon bulk and all interface calculations. It has a broad applicability and has shown to give accurate results for a wide range of materials [112].

Even with the corrections, these functionals still fail to capture all contribution of the exchange correlation. That yields to errors in the description of some structures, and underestimation of the band energies. This problem has been solved through the use of hybrid functionals which include a component of the exact exchange energy calculated from Hartree-Fock theory [113]. Because of the improvement performed, their computational cost is usually higher than for LDA or GGA based-functionals [114]. There is also a huge series of hybrid functionals available, each suitable for a specific case. In this work, we have employed two hybrid functionals: vdW-DF2 and HSE06.

The just mentioned density functionals fail to describe correctly van der Waals (vdW) interactions [104]. This is an issue in this work since vdW bonding is crucial to MoO_3. Fortunately, there is a series of functionals that solve this problem by adding a correction factor accounting for this interaction. Ding et al. [115] compared several functionals for α-MoO_3 in order to find the most suitable one. They show how DF2 is the best exchange-correlation functional together with optB88. In this work we opted for the first one, since it is the one employed in [116].

DF2 is actually a version of the vdW-DF functional [117] developed by [118]. In VASP the method is implemented by Klimeš [119][120] using the algorithm of Román-Pérez and Soler [121]. There is no specific POTCAR file for this functional; either PBE or LDA can be used [104]. In this work the PBE one was employed, following again the approach by [116].

Additionally, to employ the vdW interaction, another correction needs to be added for the correct modelling of MoO_3. This material, as well as most transition metal oxides, has metal ions with partly filled d shells [17]. Because of this, it suffers a sharper electric field screening, which results in a strong Coulomb repulsion between electrons [122]. The previously mentioned functionals do

not account for these interactions, and need to be added as a correction term. Here, the DFT+U approach of Dudarev et al [123] was applied to the Mo 4d orbitals in order to obtain more accurate results. A U correction of 5 eV was used, based on the optimization performed by Inzani et al. [124].

To summarize, the vdW-DF2+U functional (U = 5 eV) with the PAW PBE POTCAR sv file was employed for all calculations of bulk and surface MoO_3.

Along this work, it is necessary to determine accurately the energy bands of some materials. DFT does not make an accurate prediction of these energies, either by under or overestimating them, depending on the functional employed. Fortunately, Heyd, Scuseria and Ernzerhof [125] developed a very accurate exchange correlation functional, the HSE06 functional, which improves the determination of band energies. It is achieved by making a distinction between short-range and long-range terms of the screening potential. This improvement allows for a more accurate band gap value, although there is still an underestimation [126]. It is implemented in VASP through the algorithm developed in [127]. The improved accuracy also increases the computational cost of this functional. This is the reason why this functional will only be used to calculate the bulk local potentials.

4.3 Symmetry element

VASP calculations require of a unit cell periodic over space. In this work, we will encounter several structures which have not inherently a periodic structure at least in one direction. Examples of these structures are the surface of a material and the interface between two layers. In order to study these structures in DFT, the periodicity needs to be artificially added.

One way of achieving this is by assuring that the cell boundary conditions are equivalent to the ones at an infinite distance [128]. This is the fundamental idea of the supercell method. The unit cell in study is surrounded by a sufficiently thick vacuum in order to ensure that there is no interaction between adjacent cells.

4.3.1 The lattice coincidence method

The construction of interfaces will be necessary along this project. The interface needs to simulate that when two materials are in contact, they will adapt their structures in order to reduce the amount of dangling bonds [51]. Moreover, the *ab initio* simulation requires of periodicity, which implies that the interface unit cell needs to be made of an integer number of individual unit cells. This way, the periodicity of the interface structure as well as that of the adjacent materials is conserved. This can result in a rather complex process if the two solids have dissimilar lattice constants and angles. Fortunately, the lattice coincidence method [128] provides us with a system to find the lattice constants of the interface unit cell.

The unit cell of a compound is determined by a set of three lattice vectors $\{a_1, a_2, a_3\}$. The surface in which the two materials will coincide is defined by the surface vectors $\{f_1, f_2\}$, which are a linear combination of the lattice set. Analogously, the adjacent surface for the second material will be determined by the set of vectors $\{f_3, f_4\}$. These two set of surface vectors will most likely be different.

Through linear combination of the surface vector sets, one can define two new sets of vectors $\{F_1, F_2\}$ and $\{F_3, F_4\}$. The relation between sets is given by Equations 4.17:

$$F_1 = m_{11} f_1 + m_{12} f_2 \tag{4.17a}$$

$$F_2 = m_{21} f_1 + m_{22} f_2 \tag{4.17b}$$

$$F_3 = m_{33} f_3 + m_{34} f_4 \tag{4.17c}$$

$$F_4 = m_{43} f_3 + m_{44} f_4 \tag{4.17d}$$

These new sets of vectors are the lattice vectors for the interface lattice. The integer indices m_{ij} are chosen in such a way that $\{F_1, F_2\} = \{F_3, F_4\}$ and that the area of coincidence lattice unit is small. These two characteristics define a good coincidence lattice. A graphical explanation of this method is shown in Figure 4.3.

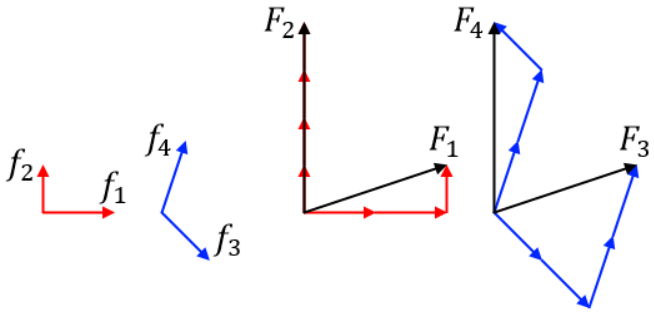

Figure 4.3: Graphical explanation of the lattice coincidence method.

It is not expected to find perfect lattice coincidence between the materials in study. Therefore, some strain is allowed so that $\{F_1, F_2\} \approx \{F_3, F_4\}$. The strain can be calculated through Equations 4.18, where it has been assumed $F_1 \geq F_2$ and $F_3 \geq F_4$.

$$s_1 = \frac{|F_1|}{|F_3|} - 1 \tag{4.18a}$$

$$s_2 = \frac{|F_2| \cos\theta_{12}}{|F_4| \cos\theta_{34}} - 1 \tag{4.18b}$$

$$s_3 = \frac{|F_2| \sin\theta_{12}}{|F_4| \sin\theta_{34}} - 1 \tag{4.18c}$$

With θ_{ij} being the angle between the superlattice unit vectors F_i and F_j. The smaller the strain and the surface area of the coincidence lattice unit cell, the better the lattice coincidence.

4.4 Structures of the materials

This section presents the structure and lattice vectors of the two materials that will be studied through *ab initio* simulations: silicon and molybdenum trioxide. The crystalline forms of these materials will be considered.

The use of these compounds is an approximation of reality. During deposition of molybdenum trioxide, this material takes an amorphous form [34]. Therefore, in order to properly simulate this material, the amorphous form should be considered. A similar issue occurs with silicon: given that

the ultimate objective is to study the interface between a-Si and MoO_3, amorphous silicon should be considered. However, the computational investigation of amorphous materials and interlayers is limited due to the large supercells required [129]–[131]. There are several studies performed about the c-Si/a-Si interface [132]–[134], but they require of complex computational methods, usually combining molecular dynamics and *ab initio* simulations [132]. Because of that complexity, they are out of the scope of this thesis.

4.4.1 Silicon

Silicon crystallizes in the cubic diamond structure, corresponding to the *Fd3m* space group [51]. It can be seen as two interpenetrating fcc sublattices with one sublattice displaced from the other by one-quarter of the distance along the body diagonal of the cube [4]. All the Si atoms are bonded to four equidistant neighbours to form a tetrahedron.

Equation 4.19 displays the lattice vectors of the primitive unit cell of silicon in Cartesian coordinates, where $a_0 = 5.43\ \text{Å}$ [135]. Only two atoms are contained in this cell, at the origin $(0,0,0)$ and at position $(0.25,0.25,0.25)$.

$$p_1 = \begin{pmatrix} a_0/2 \\ a_0/2 \\ 0 \end{pmatrix} \quad p_2 = \begin{pmatrix} a_0/2 \\ 0 \\ a_0/2 \end{pmatrix} \quad p_3 = \begin{pmatrix} 0 \\ a_0/2 \\ a_0/2 \end{pmatrix} \tag{4.19}$$

Silicon has another unit cell, the conventional unit cell. Its lattice vectors in Cartesian coordinates are shown in Equation 4.20, where the cubic structure is more straight-forward to see. 8 silicon atoms comprise this unit cell. Their positions have been found through the space group symmetries [136].

$$a_1 = \begin{pmatrix} a_0 \\ 0 \\ 0 \end{pmatrix} \quad a_2 = \begin{pmatrix} 0 \\ a_0 \\ 0 \end{pmatrix} \quad a_3 = \begin{pmatrix} 0 \\ 0 \\ a_0 \end{pmatrix} \tag{4.20}$$

Both unit cells, the primitive and the conventional one, are shown in Figure 4.4. In this work, the simulated structure of crystalline silicon has been the conventional unit cell.

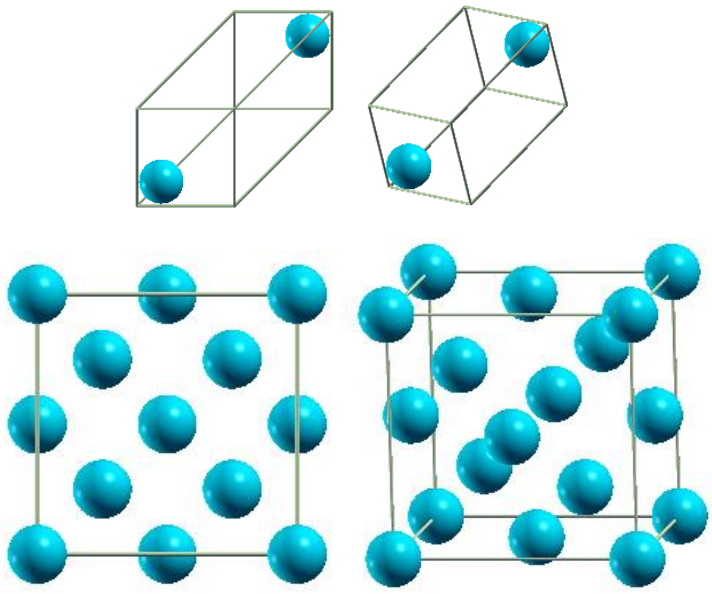

Figure 4.4: Primitive (top row) and conventional (bottom row) unit cells of crystalline silicon observed from two orientations. The silicon atoms are represented by the light blue balls. Figures generated with XCrySDen [137].

4.4.2 Molybdenum trioxide

Molybdenum trioxide has two phases, the thermodynamically stable orthorhombic α-phase, and the metastable monoclinic β-phase [138]. They both have as building block MoO_6 distorted octahedra, although ordered differently [139]. That is the building block of all molybdenum oxide phases, including amorphous molybdenum oxide [34], [140] and molybdenum dioxide [141], [142]. From now on the focus will be on the stable α phase.

Molybdenum trioxide crystallizes with four formula units of MoO_3 in a orthorhombic cell with symmetry *Pbnm* [139]. This makes the unit cell to be composed of 4 Mo atoms and 12 O atoms. The lattice vectors of this unit cell are displayed in Equation 4.21, where $a = 3.96$ Å, $b = 13.85$ Å and $c = 3.70$ Å. The symmetries of the group allow to determine the position of all the atoms inside the solar cell [136].

$$b_1 = \begin{pmatrix} a \\ 0 \\ 0 \end{pmatrix} \qquad b_2 = \begin{pmatrix} 0 \\ b \\ 0 \end{pmatrix} \qquad b_3 = \begin{pmatrix} 0 \\ 0 \\ c \end{pmatrix} \tag{4.21}$$

The structure of molybdenum oxide is based on bilayers oriented perpendicular to the y axis. The bilayers are held together across that axis by weak van der Waals forces. Each bilayer consists of two sublayers of distorted MoO_6 octahedra. These octahedra form edge-sharing zigzag rows along the z direction, and corner sharing rows along the x direction [143]. These internal interactions are held by strong covalent and ionic bonds.

In this structure, there are three inequivalent oxygen positions depending on their coordination [116], [143]. Firstly, a terminal oxygen O1 which is bonded only to one Mo atom. Secondly, a 2-fold coordinated oxygen O2 located asymmetrically between two Mo centres. Finally, the O3 oxygen is symmetrically bonded between two Mo centres in one sublayer, while forming a third bonding to a Mo atom from the neighbouring sublayer.

The structure of the TMO is displayed in Figure 4.5, where the position of the three oxygen atom sites is pointed out. The limit between bilayers is also sketched in purple dashed lines.

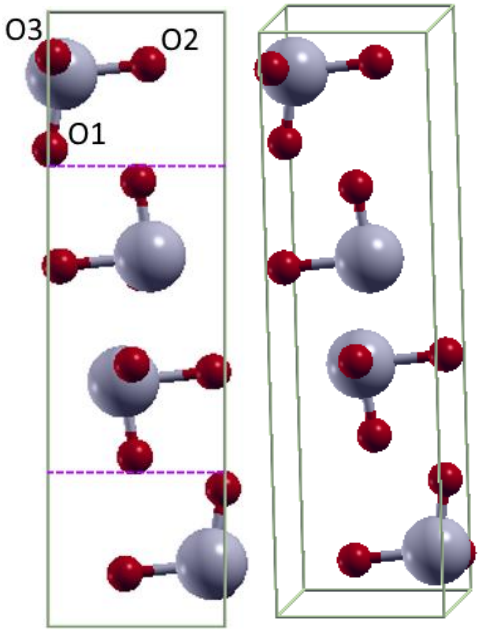

Figure 4.5: α-MoO_3 unit cell from different perspectives. The oxygen sites are indicated. Molybdenum atoms are represented by grey balls, while oxygen atoms are the red coloured ones. Figures generated with XCrySDen [137].

5

Ab initio simulation results

This chapter presents the results obtained from *ab initio* simulations. The first section 5.1 introduces a validation of the model by performing a structural optimization of the molybdenum oxides in study. The next section 5.2 calculates the work function of the oxides under different conditions. Finally, section 5.3 studies the interface between MoO_3 and silicon.

5.1 Validation of the model

In order to validate the simulated structures, a structural relaxation was performed. It consists on allowing all the atomic positions, lattice constants and angles to relax until a minimum in energy is found.

MoO_3 was structurally optimized until all the forces were smaller than 0.05 eV/Å. The energy cut-off and k-point mesh employed were 810 eV and 6x2x6, respectively. These three values are taken from [116]. The relaxed lattice constants are shown in Table 5.1, where literature values from experimental and simulated works are also compared. In the case of the simulated results, the functional employed is also mentioned (see section 4.2.3).

Table 5.1: Calculated lattice parameters for bulk MoO_3 compared to previous theoretical works and experiment. Percentage deviation from experimental values is given in brackets.

Lattice constants	[144]	[141]		[116]		This work	
	Experimental	PBE		vdW-DF2		vdW-DF2	
a [Å]	3.962	3.963	(0.03)	3.914	(1.21)	3.903	(1.49)
b [Å]	13.855	13.855	(0.00)	13.900	(0.32)	13.689	(1.20)
c [Å]	3.699	3.696	(0.08)	3.801	(2.76)	3.798	(2.68)

The results from the table show that PBE is the best functional, since its standard deviation is the lowest. However, those values were obtained by fixing the *b* parameter and relaxing the other two. This strategy needs to be used because PBE does not take into account the interactions between layers by van der Waals forces. The reduced number of degrees of freedom explains the lowest percentage deviation.

[115] showed that one of the best functionals when simulating MoO_3 is vdW-DF2. From the above table it can be seen that this method accurately represents the magnitude of the lattice parameters. The results obtained from this work are within the acceptable range of deviation. It can be stated that our model is valid.

There is a considerable underestimation of the *b* lattice constant compared to the simulations results in [116], although the k-point mesh and energy cut-off were the same. The difference is

found in the employed PAW pseudopotential: as explained in section 4.2.3, there are several versions of the PAW pseudopotentials employed in VASP [104]. In this work, we have employed the recommended standard version for oxygen molecule, while the hard pseudopotential was employed in [116]. The hard pseudopotentials are recommended when dimers with short bonds are present [104]. Given that MoO_3 is not a dimer, the use of this pseudopotential over the standard one was not motivated, so we opted for the standard one. However, looking at the obtained results, the hard pseudopotential is a better option.

The structural optimization of sub-stoichiometric molybdenum oxides was also performed. Starting with $MoO_{2.75}$, this compound was obtained by removing one oxygen atom from the MoO_3 unit cell. As mentioned in section 4.4.2, there are three inequivalent oxygen positions in the TMO unit cell. Depending on the oxygen removed, the optimal lattice constants will exhibit different values. This fact was also observed by [116]. The k-point mesh and energy cut-off were set the same as with MoO_3.

$MoO_{2.9375}$ was also structurally optimized. In order to simulate this compound, a supercell was built by repetition of the MoO_3 unit cell in directions 2x1x2. One oxygen atom in position O3 was removed in order to obtain the sub-stoichiometry. The number of k-points and cut-off energy need to be adapted to the new structure. Convergence tests were performed for both parameters in order to obtain the best trade-off between computational time and accuracy [145]. The optimal k-point mesh was found to be 6x4x6, with an accuracy of 0.01 meV/atom. The energy cut-off optimal value yield 880 eV, with a higher energy of 1 meV/atom.

Figure 5.1 shows the results from the structural optimization of the sub-stoichiometric oxides. Three lattice constants are displayed for $MoO_{2.75}$, corresponding to the removal of each of the inequivalent oxygen positions. The results obtained in [116] are also mentioned as a comparison, as well as the values for the stoichiometric oxide.

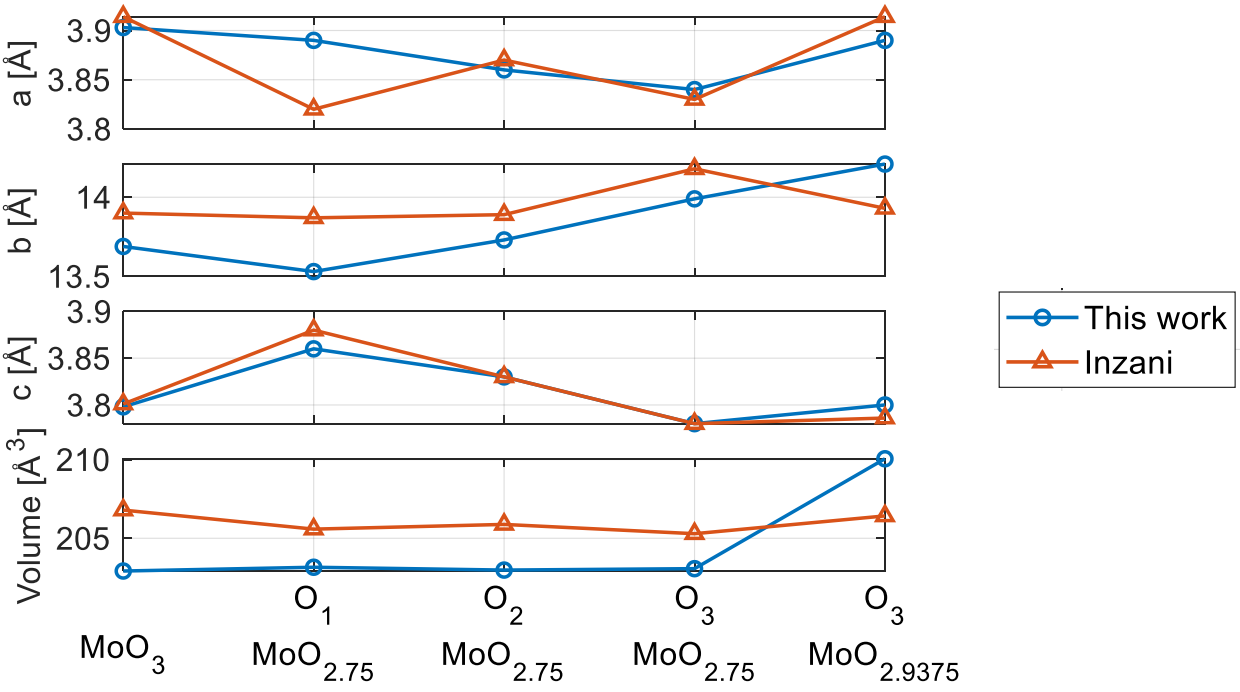

Figure 5.1: Relaxed lattice parameters from the structural optimization of $MoO_{2.75}$ and $MoO_{2.9375}$. The results were simulated for the three inequivalent oxygen positions for the atom with the lowest stoichiometry. The results obtained by [116] *as well as the parameters for the stoichiometric oxide are added for comparison.*

Taking the structural optimization of $MoO_{2.75}$ as reference, the position of the vacancies has a large effect on different cell parameters. O1 vacancy shows a large increase in *b* with decreasing *a* and *c*. The overall changes result however in the same cell volume. The O2 vacancy yields a smaller *a* parameter, a relatively unchanged *b* parameter and a slightly higher *c* parameter. As with the previous case, there is barely any change in volume. This same phenomenon is also found for the O3 vacancy. It is though achieved by a relatively unchanged *c* parameter whilst *a* and *b* decrease and increase, respectively, compared to the stoichiometric unit cell.

The structural optimization of $MoO_{2.9375}$ gives a rather surprising result since there is a significant increase in cell volume with respect to the stoichiometric and $MoO_{2.75}$ compounds. It would be expected that there are lesser effects on the lattice cell parameters as result of a lower vacancy concentration. However, the structural optimization shows a considerable increase in the *b* parameter across the van der Waals gap. The other two lattice constants are barely affected.

Comparing with the results reported by [116], with the exception of a couple points, the same trends have been obtained. Therefore, it can be stated that the model built in this work is also consistent with the removal of oxygen atoms.

Si unit cell was also structurally relaxed until all forces were smaller than 0.05 eV/Å. The cut-off energy and k-point mesh were 430 eV and 11x11x11, respectively. They showed the best trade-off in terms of energy convergence and simulation time. The results from the structural optimization show a lattice constant of 5.468 Å, in agreement with the experimental result obtained in (5.431 Å) [135].

5.2 Evaluation of the work function

Once that the structures are relaxed, material properties can be studied. In particular, the goal is investigating the work function of the molybdenum oxides. As has been stressed along Chapter 3, the work function of molybdenum oxide is a crucial parameter on the construction of SHJ solar cells featuring this material as carrier selective contact. Therefore, this section focuses on the calculation of the work function.

The work function calculation in *ab initio* simulations is however not a straightforward method. The first subsection will explain the approach employed to compute the work function. Then, the work function will be evaluated under two different conditions.

First of all, the longitude of the *b* lattice parameter will be altered to assess how the work function varies under strained conditions. Then, a second experiment is deployed to evaluate the dependency on the work function with the oxygen deficiency. Main outputs of such experiments are relevant for section 3.2, since the dependency on work function with oxygen deficiency (and therefore oxide thickness) is a key concept in this work.

5.2.1 Calculation approach

The work function is defined as the minimum energy needed to remove an electron from the surface of a solid to infinity [45]. It is calculated as the difference between the vacuum potential energy E_{vacuum} and the Fermi energy E_F, Equation 5.1:

$$WF = E_{vacuum} - E_F \tag{5.1}$$

In order to obtain the potential energy from the vacuum, a surface needs to be defined on VASP. A method to calculate the work function of materials is provided in VASP manual [104]. The approach consists on having a certain amount of unit cells which represent the bulk of the material, a unit cell illustrating the surface, and then a certain amount of vacuum. The vacuum thickness needs to be thick enough so that the atoms from the surface do not feel the interaction of the bulk atoms. Otherwise, the method could yield unrealistic results.

This approach was assessed for Si. 3 unit cells were repeated, yielding a total number of 24 Si atoms. The vacuum thickness was ≈10.8 Å, the thickness of two unit cells, sufficient to show a flat potential across it. The k-point mesh converged to 2x10x10 with an accuracy of 0.1 meV/atom, while the optimal cut-off energy resulted to be 430 eV. A work function of 4.8 eV was obtained, which is in excellent agreement with the experimentally measured value of 4.85 eV [146].

This approach is not valid for MoO_3 because the surfaces (010) and $(0\bar{1}0)$ have a different charge distribution. These surfaces are the ones between the original slab and its adjacent duplicate copy. This asymmetry generates two problems: (i) the vacuum potential energy outside these two surfaces will be different, and (ii) it would produce a uniform electric field in the vacuum slab and an opposite uniform electric field in the MoO_3 slab. Because of this electric field, there is no point where the potential energy in the vacuum is constant, thus it is not possible to define the vacuum energy.

A way to solve this issue is by adding a dipole correction into the methodology [147]. This dipole correction cancels the artificial field arouse due to the asymmetry in the charge distribution. An energy correction term is added to the total energy in order to compensate for this value.

However, in this thesis we have opted to apply the approach employed in [148]. By using two MoO_3 slabs, reflected with respect to the xz plane, the same type of surfaces will be encountered on both sides the vacuum slab. This is graphically explained in Figure 5.2.

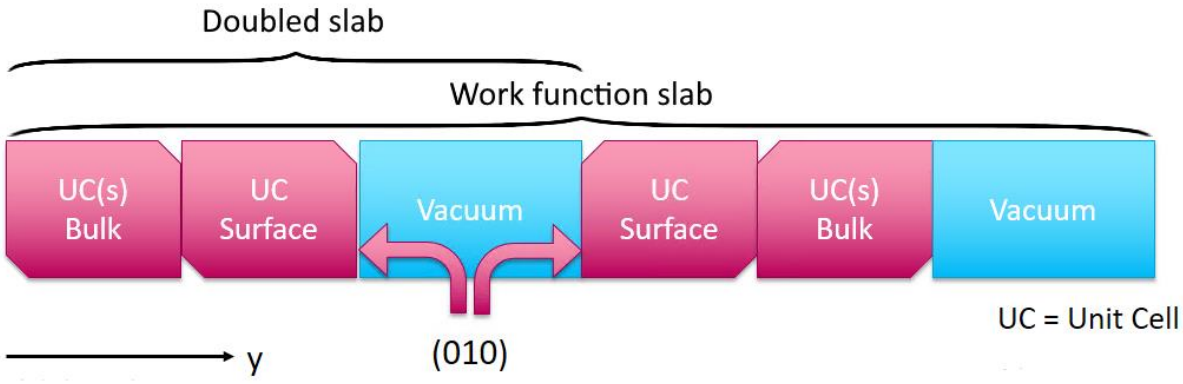

Figure 5.2: Schematic illustration of the approach employed to calculate the work function of MoO_3. The doubled slab and work function slab are pointed out. Figure based on [148].

Following such methodology, the WF of MoO_3 can be calculated. The first step consisted on duplicating the MoO_3 unit cell in y direction 1x2x1, resulting in a total of 8 Mo and 24 O atoms. 13.5 Å of vacuum were also applied on that same direction. Overall a super cell of 3.8x40.6x3.9 $Å^3$ volume was simulated. We will refer to it as the *doubled slab*. The cut-off energy and k-point mesh were found optimal to be 840 eV and 10x1x10 in a trade-off between computational time and accuracy. Under those circumstances, the atomic coordinates and positions were optimized by relaxing the structure until all forces are smaller than 0.05 eV/atom.

With the optimized structure, the slab for the work function calculation was built. It consisted on a *doubled slab*, approximately 3.7 nm of vacuum, another *doubled slab* reflected with respect to the y direction, and finally roughly 2.35 nm of vacuum. We will refer to it as the *work function slab*. It resulted on a supercell of 16 Mo and 48 O atoms with dimensions 3.8x114.7x3.9 $Å^3$. The vacuum thicknesses were increased with respect to the previous case in order to assure the flat potential across the vacuum layers. The k-point mesh was kept to 10x1x10 since it gave the same accuracy as higher meshes (such as 20x1x20).

The average local potential from this structure is shown in Figure 5.3. The position of the Mo atoms and some of the O atoms can be observed in its dips. The flat sections represent the potential across the vacuum slabs. The Fermi level has been taken as reference. The work function has been pointed out.

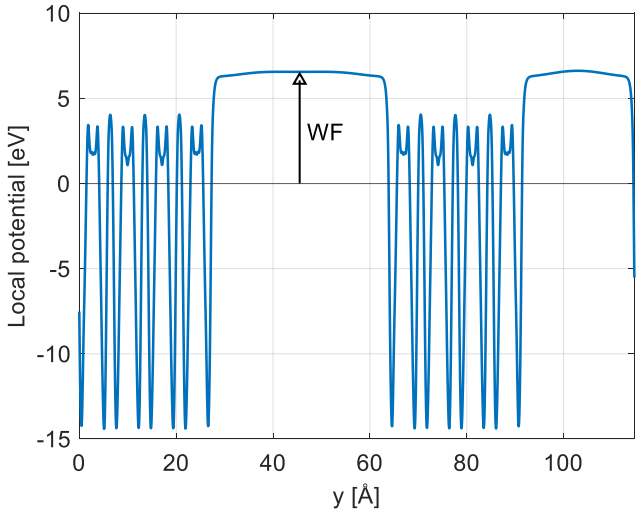

Figure 5.3: Local potential of MoO_3, with the Fermi level taken as zero reference. The work function has been pointed out.

A work function of 6.56 eV was obtained with this method. Although it is a reasonable range, it is smaller than the measured value of 6.9 eV [86]. This is due to the known underestimation of the band structures in DFT calculations [128]. This underestimation is however no problem since the obtained value will be compared to the work function calculation of molybdenum oxide under different conditions.

5.2.2 Effect of strain in MoO_3

During deposition of lattice-mismatched crystalline materials, the materials deposited last needs to adapt its structure in order to minimize the energy of the system [4]. This results in a distortion of the lattice constants of the unit cell, which often results in altered characteristics of the material.

[149] calculated through DFT how the band gap of MoO_3 varies under different distortions. They showed how, depending on the type of stretching and across which axis, there was a variation in the band gap. This section presents a similar study but focussed on work function analysis. Basically, the goal is to assess the effects of distortion of the MoO_3 unit cell in the work function.

In this thesis, for the sake of simplicity, the stretching was only performed on the y direction, since calculations of work function of MoO_3 are complex and demand high computational effort. The choose of y-direction follows the orientation in which the MoO_3 bilayers are repeated.

For the work function calculation, abovementioned method was employed. The energy cut-off and k-points mesh were kept constant. The *b* parameter was increased and decreased. The results for work function as a function of the distortion of *b* lattice constant is shown in Figure 5.4.

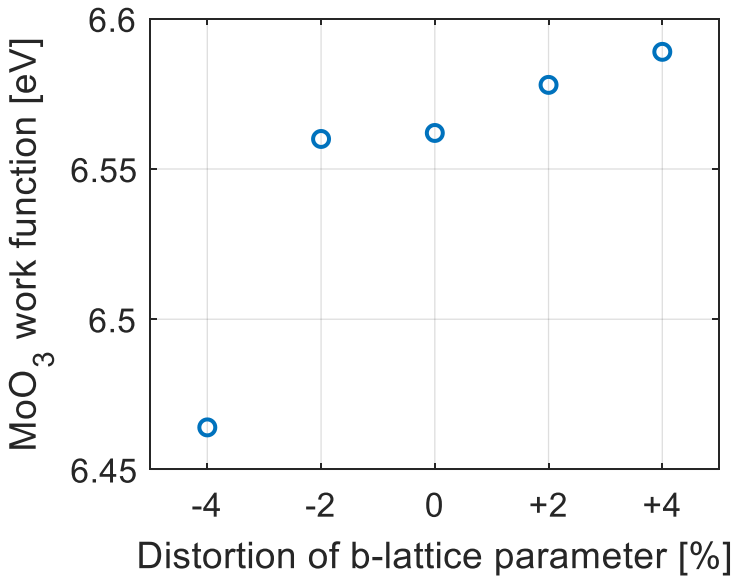

Figure 5.4: MoO_3 work function as a function of the distortion of b lattice constant.

As Figure 5.4 shows, the higher the stretching, the greater is the work function. Since the work function is defined as the energy needed to remove an electron atom from the surface of the TMO, this implies that the thicker the parameter, the harder it is to remove the electron. All the points follow a common trend except for the -4% distortion.

5.2.3 Effect of oxygen deficiency

The dependence on work function with oxygen deficiency is a key factor (see section 3.3) . Accordingly, its understanding is essential for the improvement of solar cells. In this section, the work function of different sub-stoichiometric molybdenum oxides will be calculated. The sub-stoichiometry was obtained by removing oxygen atoms from two different inequivalent positions: O2 and O3. These atoms are the ones closer to the surface and the Mo-O1 interaction is stronger [150], therefore O2 and O3 are most likely to detach. The dependence on work function will be not only on the amount of oxygen deficiency but also on the position of the oxygen atoms.

Five molybdenum oxides were simulated: MoO_3, $MoO_{2.958}$, $MoO_{2.9375}$, $MoO_{2.92}$ and $MoO_{2.875}$. The energy cut-off was kept to 840 eV for all the calculations. This value was found optimal for the larger structures ($MoO_{2.958}$ and $MoO_{2.92}$) and set for the remaining compounds in order to get consistent results.

The material with the highest deficiency was achieved by removing one oxygen atom from each of the *doubled slabs* from the *work function slab*. There were 16 Mo and 46 O atoms in this supercell. The position of the removed oxygen atom was the equivalent in each *doubled slab* in order to maintain the symmetry. The k-point mesh for this structure was the same as for the stoichiometric slab.

In order to obtain $MoO_{2.9375}$, the *work function slab* was duplicated in the z-direction (1x1x2). It resulted on a bigger supercell with 32 Mo and 92 O atoms. Two oxygen atoms were removed

from two of the symmetric *doubled slabs* in order to obtain the stoichiometry. The k-point mesh was decreased to 10x1x5.

The last two stoichiometries required an even greater supercell. The *work function slab* was repeated 1x1x3 times, yielding 48 Mo and 144 O atoms. $MoO_{2.958}$ was obtained by removing two oxygen atoms from one of the *doubled slabs* and its symmetric couple, while $MoO_{2.92}$ required of the removal of four oxygen atoms. The k-point mesh was reduced again to 10x1x3.

The work function for each of these structures was calculated as Figure 5.5 reports. A decrease in work function can be appreciated as the oxygen deficiency increases. This is in concordance with what has been observed in literature [86]. Moreover, in that same graph, it can be observed that the removal of an oxygen in O2 or O3 position does not have a big influence on the work function.

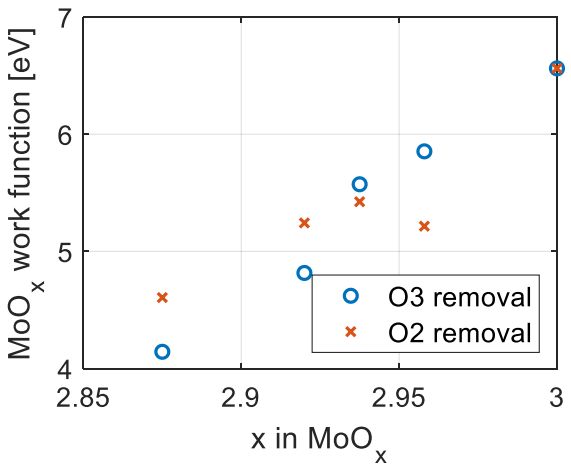

Figure 5.5: Work function of molybdenum oxides depending on oxygen deficiency.

5.3 MoO_3/Si interface

The main purpose of DFT calculations is to study the formation of the dipole at the MoO_3/Si interface. This section focuses on the construction and analysis of the interface between the two materials. Since it is a complex process, the thesis by Höffling [128] will be used as reference and the approach he employed for the study of the interface will be followed step by step.

5.3.1 Coincidence lattice

The first step for the study of the interface is to create a reasonable atomic model for a crystalline interface between cubic diamond silicon and molybdenum trioxide. It has been achieved using the lattice coincidence method described in section 4.3.1. The search was restricted to (010) surface orientations and to coefficients with $|m_{ij}| \leq 8$. It is highly appealing to use (010) surface for c-Si since that is the preferred orientation for solar cells fabrication [151]. It is also convenient for MoO_3 because of its configuration: given the bi-layered structure no bond must be broken to form the (010) surface [152] and the y direction is the weakest one [153].

The best results are listed in Table 5.2, considering the unit lattice vectors from Equation 5.2. f_1 and f_2 are the lattice vectors from silicon while f_3 and f_4 are the ones from MoO_3. The strains for each combination are also included (s_1 and s_2). The strain is evaluated in terms of misfit in the

coincidence lattice basis vectors, as defined in Equation 4.18. The third strain s_3 was not calculated because the vectors employed are parallel to each other, therefore $s_3 = 0\,\%$ for all cases.

$$f_1 = 5.431\begin{pmatrix}1\\0\\0\end{pmatrix} \qquad f_2 = 5.431\begin{pmatrix}0\\0\\1\end{pmatrix} \qquad f_3 = 3.903\begin{pmatrix}1\\0\\0\end{pmatrix} \qquad f_4 = 3.798\begin{pmatrix}0\\0\\1\end{pmatrix} \tag{5.2}$$

Table 5.2: Best coincidence lattice cells for Si and MoO_3.

F_1	F_3	$s_1[\%]$	F_2	F_4	$s_2[\%]$
$3f_1$	$4f_3$	4.36	$2f_2$	$3f_4$	-4.67
$5f_1$	$7f_3$	-0.61	$5f_2$	$7f_4$	2.14

The first noticeable feature of the discovered coincidence lattices is that in order to have a low strained material, it has to be big. That would probably explain why MoO_3 grown on silicon has an amorphous character and the reactivity of oxygen is considerably increased. Without a good lattice coincidence, we would expect that breaking the crystal symmetries at the interface in order to minimize dangling bonds is energetically preferable to overstraining the crystal structure [128]. However, as mentioned in section 4.4, DFT simulation of amorphous structures is not computationally feasible. Therefore, a strained model will be used for our investigation. The interface structure was built by fitting 12 MoO_3 unit cells with six cubic Si(001) unit cells. The stress was put entirely on the oxide side of the interface. The x direction is increased by 4.36% while the z direction is 4.67% shorter. This also mimics experimental growth conditions, where the oxide layer is generally grown on a Si substrate, so the silicon should impose its crystal structure onto the oxide.

The straining of the MoO_3 instead of the Si is also supported by the bulk modulus. The bulk modulus of a substance is a measure of how resistant to compression that substance is [154]. It is defined as the ratio of the infinitesimal pressure increase to the resulting relative decrease of the volume. Hence, a material with a bulk modulus of 100 GPa loses 1% of its volume when subjected to an external pressure of 1 GPa. When comparing the bulk modulus of two materials, the one with the lowest value is the easiest to compress. The bulk modulus for c-Si is 97.6 GPa [155], while for MoO_3 it is 40.1-48.2 GPa [156], [157]. This indicates that the TMO is easier to compress than Si.

With the already mentioned strains of the *a* and *c* lattice constants of the MoO_3 unit cell, the third lattice vector had to be found. A sweep was performed in order to find the *b* parameter that minimized the energy. The relaxation resulted in an energy minimum for *b* = 13.727 Å, a compression of only 0.28 %. Overall, the cell volume was only reduced by 0.24 %.

The bulk positions of the strained TMO were relaxed until the forces were below 5 meV/Å. Under those circumstances, the work function was found to be 6.94 eV, higher than in the non-strained material. However, evaporated MoO_3 thin films show an amorphous structure [34] therefore it is not possible to state that the work function of bulk MoO_3 deposited on top of c-Si increases.

5.3.2 Atomic structure

The supercell interface between the two materials was constructed by embedding the strained MoO_3 (001) unit cell in a 5 layer Si(001) matrix. The supercell contained a total of 252 atoms. The supercell can be sketched in the right graph from Figure 5.6.

The MoO_3 unit cell employed for the surface was different than in all previous calculations. On the left graph of Figure 5.6, the MoO_3 unit cell employed for all previous simulations can be observed. Figure 5.6 (middle) displays the unit cell employed for the interface calculations. It can be seen that the molecules have been displaced in the y-direction. This is done for two reasons. (i) So that the closer atom to the silicon surface is an oxygen one instead of a molybdenum one. This was done to favour the Si-O bonds. (ii) In order to have two full bilayers deposited on top of the silicon surface. The limit between bilayers has been pointed out by purple dashed lines in those pictures.

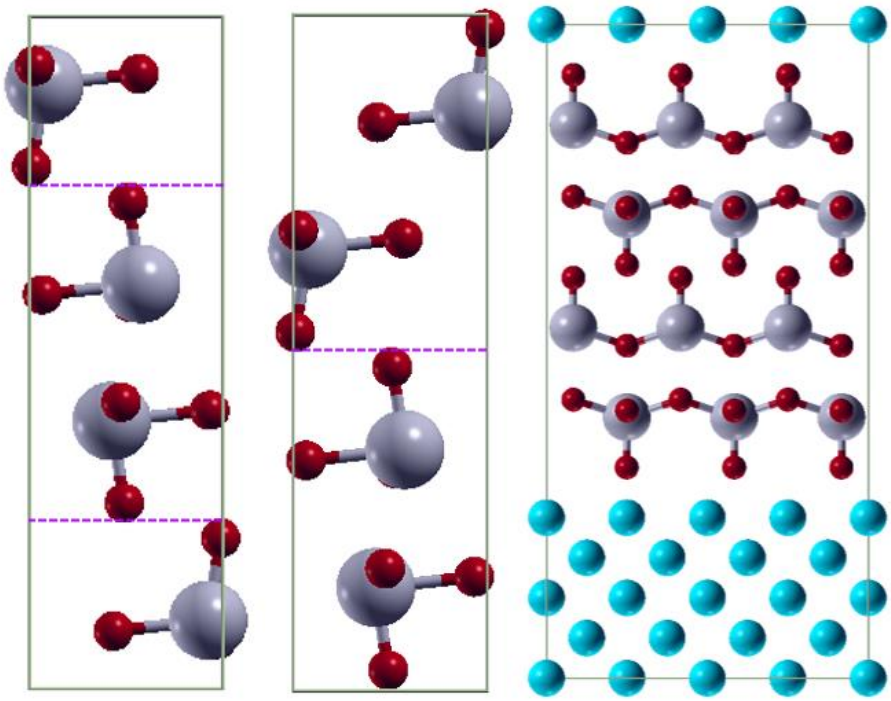

Figure 5.6: Left, original MoO_3 unit cell employed in all previous calculations. Middle, modified MoO_3 unit cell for the interface simulations. Right, MoO_3 and Si interface. The dashed purple lines represent the limits between bilayers in the MoO_3 unit cells. Molybdenum atoms in grey, oxygen ones in red, silicon atoms in blue. Figures generated with XCrySDen [137].

Si-O bonds are known to be very strong [158] and that is the reason why fabricated devices often find silicon oxide layers in that interface [77], [82]. This statement can be supported by comparing the strength of the Si-O bond with the one of the Mo-O bond. In [128], the obtained strength for SiO_2 is 1.32 eV for every broken Si-O bond. The same approach has been employed to obtain the strength of the Mo-O bond. From literature [153], [159], the (010) surface energy of MoO_3 calculated using DFT methods is around 0.826 J/m^2, equal to 51.56 meV/Å^2. Considering that there are four dangling Mo-O bonds per unit cell, and an area of the (010) surface of 15 Å^2, the bond density of MoO_3 is of 0.27 bonds/Å^2. Considering the already mentioned surface energy, the energy cost of breaking a Mo-O bond is of 0.19 eV. Comparing to the already mentioned 1.32 eV energy cost of breaking a Si-O bond, there is a significant difference. Even though the exact values depend on the conditions and type of bonding, we can state that the Si-O bond is stronger than the Mo-O bond. Therefore, the formation of the SiO_2 interlayer at the MoO_x/a-Si interface is favourable. This supports the study performed in section 3.2.1, where the formation of the SiO_2 interface was assumed from literature.

Back to the interface analysis, two optimizations were performed on the built supercell. First, the MoO_3 slab was laterally displaced on top of the c-Si matrix until the minimum of total energy was reached. Second, the optimal distance between the slabs in y direction had to be found. All the

calculations performed on the super cell employed the PBE functional, a reduced k-point mesh of 2x4x3, and a cut-off energy of 840 eV.

Starting with the lateral displacement, the MoO_3 slab was moved laterally in a 4x4 grid, following the same approach as in [128]. Given the high symmetry of the c-Si layer, only 16 points were needed for this optimization. The resulting total energies are plotted in Figure 5.7. The variation in total energy within the values explored is negligible.

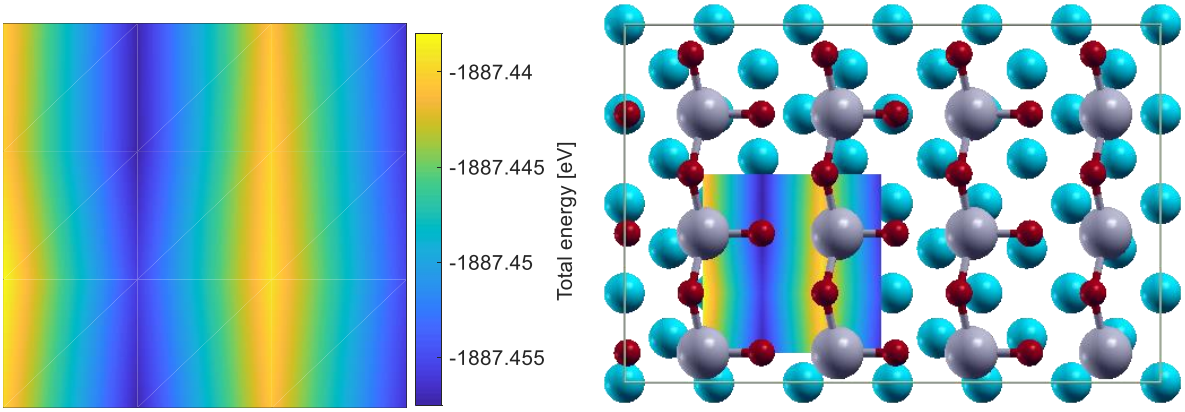

Figure 5.7: Left, total energy of the interface cell for MoO_3 moved across the Si unit surface cell. Right, top view of the unrelaxed interface structure unit cell. The two highest Si layers (blue) and lowest O (red) and Mo (grey) layers are shown.

In order to find the optimum displacement between slabs, the atomic distance in y direction between the closest Si-O was taken as a reference. It was tuned until a minimum in total energy was reached. The result of the optimization can be seen in Figure 5.8, yielding an optimum distance of 1.7 Å.

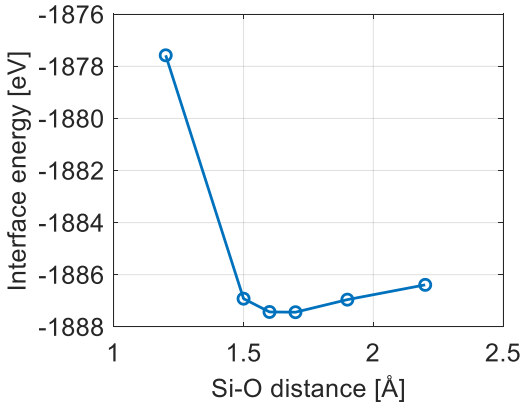

Figure 5.8: Optimization of the Si-O distance.

Once the optimized geometry was found, an ionic relaxation was performed until the forces were below 5 meV/Å. Unfortunately, due to time restraints, the results were delayed and it has not been possible to analyse them here. However, some information can still be extracted on the unrelaxed structure about the electrostatic potential and the charge rearrangement. Although some errors are expected, the main conclusions extracted may still be valid. In [128], the electrostatic potential and charge rearrangement is performed in the relaxed and unrelaxed structure. The exact values are different, but the conclusions extracted are the same. Therefore, the discussion from the next sections on the unrelaxed structure will most likely be very similar to the one on the relaxed one.

5.3.3 Electrostatic potential

This section explores the electrostatic potential at the interface. The most important information we calculate is the band discontinuities between the materials. In such calculations, the conduction band and valence band levels need to be first determined from the bulk materials.

As mentioned in section 5.2, there is a systematic underestimation of the band energies in DFT. This underestimation can be reduced by employing the functional HSE06, presented in section 4.2.3. The use of this functional allows for a more accurate description of the band energies of a bulk material. Therefore, the valence and conduction band energies can be found with higher precision.

With that purpose, the local potential and band energies of the Si and MoO_3 bulk were calculated employing the HSE06 functional. The energy cut-off and k-point mesh for these calculations are the same as for the bulk calculations in section 5.1. From this analysis, the band gap of these materials is extracted: $E_{g,Si}$ = 1.3 eV and $E_{g,MoO3}$ = 2.8 eV.

The value for crystalline silicon is in excellent agreement with the one simulated in [128] (1.29 eV), where the same approach was employed. This functional has shown to be the most accurate compared to other tested functionals [160], [161]. However, there is still a difference with respect to the measured band gap for c-Si of 1.12 eV [45].

The MoO_3 band gap is in excellent agreement with the one measured in [162] of 2.81 eV. As done with silicon, different functionals were also employed to calculate the TMO band gap and the conclusion is similar: HSE06 shows a higher accuracy than LDA or GGA functionals [163]. The band gap was also calculated employing different vdW functionals, and still HSE06 showed a better [124]. Comparing with literature, the value obtained in this work is an underestimation of the measured band gap. However, the amount of this error cannot be properly measured because there is not high concordance in the measured band gap values which range from 3 to 3.8 eV [[164]–[166] and references in therein].

Once obtained the local potential for the interface and for the bulk materials, they are aligned. Alignment of the electrostatic potentials of the bulk materials with the potential at the interface gives information about the type of alignment that it is found between the materials. By aligning the bulk potentials with the one from the interface, although not obtained with HSE06 because of the high computational time needed by the functional, the difference between conduction and valence band energies can be found accurately. The results will reveal the energy barriers at hetero-interfaces for charge collection.

The electrostatic potential of the unrelaxed interface across the y direction is shown in Figure 5.9. In the graph the position of the atoms is noticed by the dips in energy. The five silicon layers can be identified, as well as the 4 Mo atoms. The O atoms are harder to identify, since their energy drop is shielded by that of Mo. In the graph, the local potentials of the bulk materials obtained through the more accurate HSE06 functional are also shown.

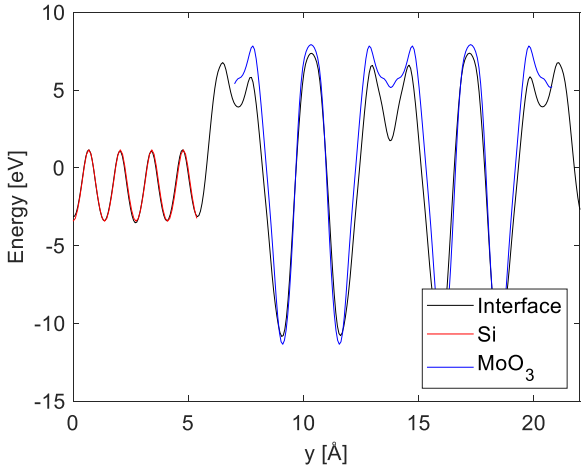

Figure 5.9: Electrostatic potential at the interface.

While the Si bulk potential aligns perfectly with the bulk potential, the same condition does not occur with the MoO_3 bulk potential. In fact, a slightly different shape is found, and there is not alignment between the maximums and minimums of both potentials. This problem is tackled by considering two different type of alignments. First, the MoO_3 bulk potential is aligned with the interface potential by making the highest points of both energies coincide. Second, the potentials are aligned by the minimums of energy. The type of structure found for each case will be compared to the alignment found by semiconductor physics simulations.

The interface potential together with the conduction and valence bands for the two alignments are shown in Figure 5.10. The figure on the left displays the alignment by making the minimum of potentials coincide, while the figure on the right employs the maximum values for the levelling. The valence band and conduction band energy obtained from the bulk calculations are also shown in Figure 5.9.

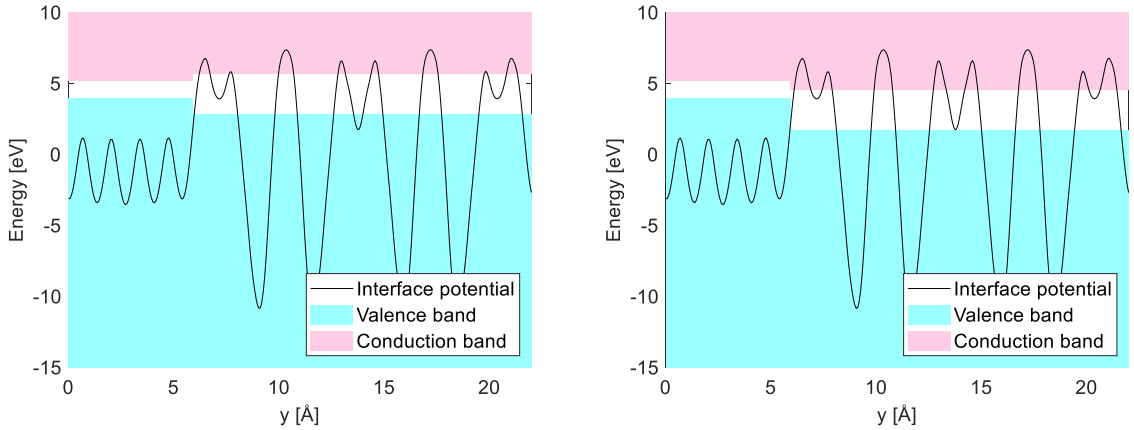

Figure 5.10: Interface potential and band energy levels for the alignment of MoO_3 bulk potential by minimums (left) and by maximums (right).

Looking at Figure 5.9 (left), there is a potential barrier at interface for the movement of carriers from Si to MoO_3. This type of alignment prevents charge-carrier separation at the interface. If an electron-hole pair would reach this interface, none of the carriers would be able to travel from Si to MoO_3 easily so they would recombine. By defining the difference between bands as displayed in Equations 5.3 [128], the band offsets of this structure are $\Delta E_C = 0.47$ eV and $\Delta E_V = 1.15$ eV.

$$\Delta E_C = E_{C,MoO3} - E_{C,Si} \tag{5.3a}$$

$$\Delta E_V = E_{V,Si} - E_{V,MoO3} \tag{5.3b}$$

On the other hand, the alignment by using maximums of the potentials shows a different interface. The electrons that want to travel from silicon to the oxide, do not encounter any barrier, while the holes need to overcome a high energy barrier to achieve that same venture. For this situation the difference between band energies are $\Delta E_C = -0.64$ eV and $\Delta E_V = -2.26$ eV.

Comparing these two structures, the energy levels obtained by alignment by maximums is consistent with the simulations performed in Chapter 3. This can be seen by comparing the above figure with Figure 3.2. A similar energy alignment is observed. Since the TMO acts as a hole contact in solar cells, one would expect to find the barrier for the electrons, not holes. However, as deeply discussed in Chapter 3, the transport mechanism between Si and MoO_3 consists on holes from Si recombining with the electrons from MoO_3. In this structure, rather than looking at the offsets between the conduction and valence bands, we should be considering the energy difference between the valence band of Si and conduction band of MoO_3. Making the calculations, a value of $\Delta E = 0.54$ eV is found. This energy difference is smaller in absolute value than the two previously discussed, showing that the transport mechanism considered along this work is consistent with atomistic DFT models. Moreover, in the simulated solar cells, the interface is not the only important fact. The electric field that the bulk material suffers alters the carrier population, making the electrons the minority charge carriers and the holes the majority ones on the Si/MoO_3 interface. Under this condition, the hole current from Si to MoO_3 is dominant over the current of electrons from Si to MoO_3.

5.3.4 Interface dipole

As mentioned thoroughly this work, the objective of *ab initio* simulations is to identify the formation of the dipole. A dipole is defined as a separation of a pair of equal and oppositely charges over a narrow distance [89]. In order to recognise the dipole, these interface charges need to be identified.

VASP allows to calculate the electron charge distribution of simulated structures [104]. The calculated electron charge density distribution of MoO_3 slab (not shown) is in concordance with literature, where the distribution of charge is spherical and the charges are accumulated around the oxygen atoms [162]. However, we are not interested on the charge distribution of the slabs individually, but rather on the movement of charges because of the interaction between layers.

The change in the distribution of charges at the interface is the most important tool to identify the dipole. In order to investigate the charge transfer between slabs, it is necessary to compare the charge density for the interface system with the isolated subsystems in vacuum [128]. These subsystems were built by removing either the Si or MoO_3 slab from the interface cell. The charge rearrangement is calculated as the local charge density difference [167], displayed in Equation 5.4.

$$\Delta n(\boldsymbol{x}) = \Delta n_{IF}(\boldsymbol{x}) - \left(\Delta n_{Si}(\boldsymbol{x}) + \Delta n_{MoO3}(\boldsymbol{x})\right) \tag{5.4}$$

Where $\Delta n(\boldsymbol{x})$ is the local charge density as a function of all three coordinates in space $\boldsymbol{x}$, and the sub-indexes stand for the interface (IF), the silicon slab (Si) and the molybdenum oxide slab ($MoO3$). Integrating over the plane A perpendicular to the surface normal y we can determine the differential charge dQ, Equation 5.5.

$$dQ(y) = \int_A \Delta n(\boldsymbol{x}) dxdz \tag{5.5}$$

By integrating it again into a volume between y_0 and y, the charge transfer ΔQ is obtained, Equation 5.6.

$$\Delta Q(y, y_0) = \int_{y_0}^{y} dQ(y) dy \tag{5.6}$$

Figure 5.11 shows the differential charge and the charge transfer at the interface. As expected, most of the charge rearrangement is located at the interface. In particular from the differential charge graph, charge is transferred from the most external Si atoms to the O atoms closer to the interface. This is caused by the already mentioned Si-O bonds that are formed at the interface between materials.

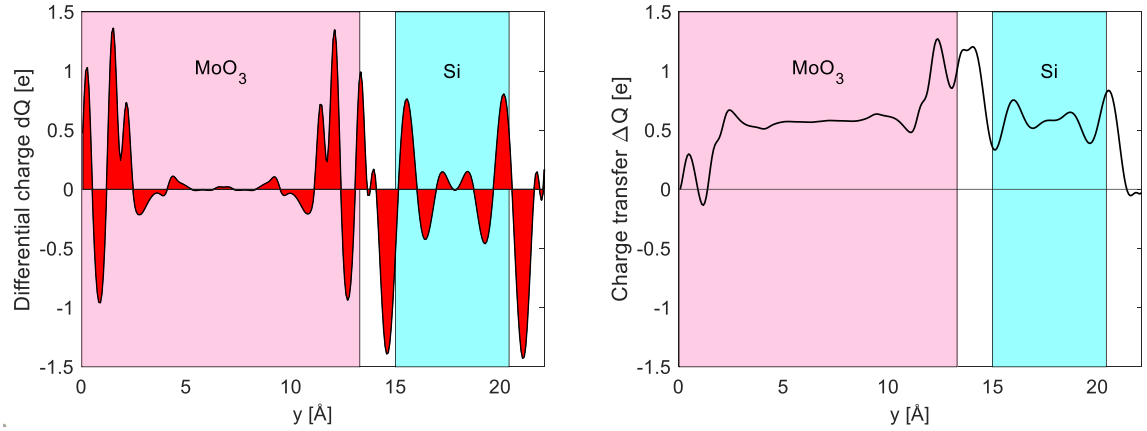

Figure 5.11: Differential charge dQ (left) and charge transfer ΔQ (right) upon the formation of the MoO_3/Si interface.

The charge rearrangement also shows the formation of the dipole. The left graph shows how negative charge is placed at the interface of the MoO_3, coming from the Si atoms. The accumulation of negative charge at the MoO_3 surface is in concordance with the negative dipole implemented in the semiconductor physics simulations from section 3.2.2. The charge transfer graph (right on Figure 5.11) experiences a drop on the interface between MoO_3 and Si, which is also a representative feature of the interface dipole. There is a subtle yet continuous increase of ΔQ throughout the oxide. It represents a small charge transfer from the Si slab to the MoO_3. However, for balancing the charge, it is also necessary to observe a continuous decrease of ΔQ in the bulk-like Si region, which is not so clearly visible.

From the differential charge figure, an approximated dipole moment can be calculated. Considering the basic definition of the dipole moment $p = Q\, d$ [89], the charge accumulated and the separation distance can be extracted from the differential charge graph (left on Figure 5.11). Taking the average between the energy peak at the MoO_3 surface and the drop at the Si, the charge of this dipole is 1.2 electrons. The distance between these two points is 1.24 Å, considered to be the distance of the dipole. Knowing the elementary charge, a dipole moment of 7 D is obtained. This value represents a quite high dipole moment when comparing it to the dipole moments considered in section 3.2. However, considering the previously measured work function of the strained MoO_3 of 6.9 eV, a higher dipole moment is expected. Comparing it to literature, in [168] a dipole moment of 4.52 D was calculated through DFT for a MoO_3 cluster on top of Cu(111).

The dissimilarity in the simulated structures could explain the difference in dipole moments, but in any case the values are of similar magnitude.

The effect of the charge rearrangement can also be studied through the difference in the local electrostatic potential. Analogous to the local charge density difference, the local electrostatic potential difference $\Delta V(\boldsymbol{x})$ is obtained, Equation 5.7 [167].

$$\Delta V(\boldsymbol{x}) = \Delta V_{IF}(\boldsymbol{x}) - \left(\Delta V_{Si}(\boldsymbol{x}) + \Delta V_{MoO3}(\boldsymbol{x})\right) \tag{5.7}$$

It can be interpreted more easily by taking the planar average $\Delta\bar{V}(y)$, Equation 5.8.

$$\Delta\bar{V}(y) = \frac{1}{A}\int_{A} \Delta V(\boldsymbol{x})dxdz \tag{5.8}$$

The electrostatic potential difference is depicted in Figure 5.12. The sharp drop on the interface region shows the dipole step in the y direction. This is the so-called work function attenuation due to the dipole, extensively discussed on Chapter 3. The potential step between the two peaks in which the 7 D were calculated is of 0.79 eV. Looking at Figure 3.12, where the dipole moment is related to the work function attenuation, an attenuation of 0.79 eV yields a dipole moment slightly higher than 6 D. This value is consistent with the previously calculated dipole moment by DFT. Overall, we have related and found concordance between DFT and semiconductor physics simulations.

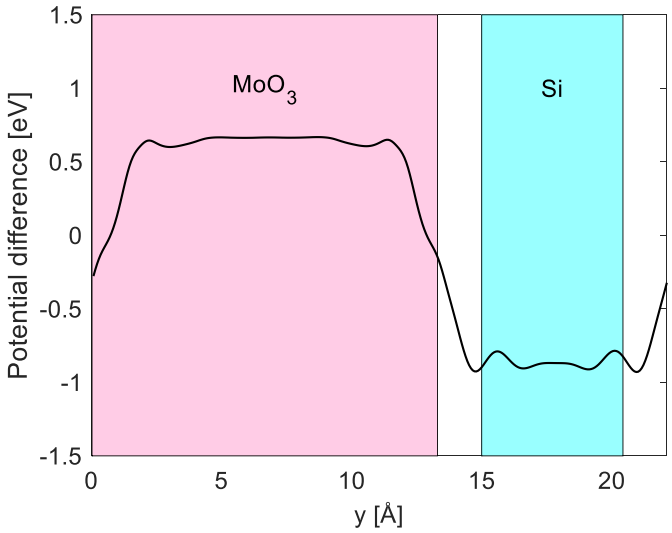

Figure 5.12: Electrostatic potential difference at the interface between MoO_3 and Si due to rearrangement of charges.

6 Conclusions

This chapter summarizes the final conclusions of this study by answering the main research questions presented in section 1.1.

- What are the main material parameters affecting the contact formation?

As explained in section 3.1, the main material parameters that affect the contact formation of MoO_3 are the trap concentration and the work function. We have demonstrated how in the simulated devices a high work function and trap concentration are the key parameters for achieving the greatest conversion efficiency.

- How is the transport behaviour?

The second question was also answered in section 3.1, since the tuning of the work function determined the type of transport mechanism that occurred in the solar cell. Trap assisted tunnelling was dominant when there was no energy alignment between amorphous silicon and molybdenum oxide, condition that occurred for low work function values. On the other hand, band to band tunnelling is dominant for high TMO work function values, when the energy levels were aligned in a way that charge carriers were able to easily trespass from one material to the other.

- What are the limiting physical mechanisms for hole transport layer stack?

The main limiting physical phenomena encountered were found at the interface. Section 3.2 explores how the interface between molybdenum oxide and amorphous silicon impacts in charge collection. Two mechanisms were studied in this interface: the appearance of a silicon dioxide interlayer, and the work function attenuation.

The effect of the silicon dioxide interlayer strongly depended on the work function of the TMO. For high work function values, the interlayer showed barely any effect in the performance of the solar cell as long as the tunnelling limit was not reached. The interlayer is even positive for achieving relatively high V_{OC}. However, for low MoO_3 work function values and thick enough SiO_2 interlayers, S-shapes were encountered in the J-V response, as a result of low charge carrier accumulation. The reactions that yielded to the growth of this interlayer were discussed in section 5.3 through the study of the interface between MoO_3 and c-Si.

The origin and three components of the work function attenuation were studied in section 3.2.2. For relatively high work function attenuation values (>1 eV), it was shown how this phenomenon had a detrimental effect on the open circuit voltage of the solar cell. The reduction of the dipole component strongly depends on the thickness of MoO_x layer. Accordingly, adjusting MoO_x thickness potentially lead to the optimal solar cell because the magnitude of the interface dipole is thickness dependant.

Through the introduction of the interface dipole and the silicon dioxide interlayer, a realistic model for solar cells was built. An adequate trade-off between two components was shown to result in the best efficiency: (i) high work function and (ii) low interface dipole. The model was validated through the fitting of fabricated devices, including the record solar cell. The obtained results were in reasonable agreement, hence confirming hypothesis statements of this thesis, implying that the developed model reproduce the inner physics of the solar cells under study.

- What material parameters can be controlled during the process to improve conversion efficiency?

The outcomes obtained from this fitting, together with a brief optical study, allowed us to provide guidelines for the fabrication of solar cells. They are explained in section 3.3.3. The most important ones are (i) keep a suitable trade-off between the interface dipole and silicon dioxide interlayer through the MoO_3 work function, (ii) tune MoO_3 work function through the layer thickness, (iii) keep the passivation layer as thin as possible to improve the light management.

- What is the atomistic nature of interface charge rearrangement?

The *ab initio* simulations performed in chapter 5 confirmed most of the phenomena assumed from literature in the drift diffusion results chapter. After a validation of the model in section 5.1, the work function of molybdenum oxide was measured in section 5.2. It was shown how the oxygen deficiency decreased the work function of the transition metal oxide, which is related to the tuning of work function through the layer thickness. This statement was the basis for the reduction of the interface dipole in Chapter 3.

Section 5.3 studied the interface between crystalline silicon and molybdenum oxide as the basic structure of MoO_x/a-Si interface. Therefore, the main outcomes obtained are the core for extended future studies including amorphous matrix. These studies showed that the Si-O bonds are stronger than the Mo-O ones, which indicate that the former will be preferred over the latter. Therefore, the formation of the SiO_2 interlayer at the MoO_x/a-Si interface is energetically favourable. Secondly, the energy level alignment found between the two adjacent materials is consistent with parameterization of drift diffusion simulations. Since the transport mechanisms strongly depend on the energy level alignment, this result confirms that the charge transport is based in intra-band trap assisted tunnelling and band to band tunnelling. Finally, the charge rearrangement between the molecules in the unrelaxed structure showed the formation of the interface dipole. The dipole moment and the drop in energy resulted from the electrostatic potential were within the values explored in Chapter 3, indicating agreement between both simulating studies.

7 Outlook

The initial objectives of this thesis only regarded drift diffusion simulations. These were fulfilled relatively fast, so it was decided to extend the field of research of this study to *ab initio* simulations. The results from these simulations have provided a more complete research. After the work performed, several research lines are opened to keep this investigation.

First of all, because of the already mentioned time constraints, the atomic position relaxation of the interface simulations were not finished by the end of this thesis. If the simulations had been ready on time, the results on the relaxed interface could be analysed and compared to the ones of the unrelaxed interface. It is expected that the conclusions drawn from both systems are very similar, however these results would make the thesis more complete.

Following the research line of this study, the use of molybdenum trioxide as p-contact could be explored. Solar cells have been fabricated under this condition, therefore it is a feasible study.

All the work performed on molybdenum could be extended to the other two transition metal oxides employed as hole contact: vanadium pent-oxide (V_2O_5) and tungsten tri-oxide (WO_3). A very complete comparison between the three could have been done, and the reason of the higher outcome for molybdenum oxide could be found.

Regarding the *ab initio* simulations, more realistic interface models could be implemented. First of all, considering the Si (111) surface instead of (010), representing the texturing of solar cell. The results obtained could be compared to the ones on (010) surface, observing the effect that the silicon orientation could have, if any, on the dipole and silicon oxide interlayer formation.

On this same topic, the simulation of amorphous materials could be implemented. This would apply not only to the transition metal oxide, but also to the passivating layer. As already mentioned, the computational cost and difficulties of these simulations is high, but there are studies on the simulation of amorphous materials, so it could be feasible. These results would also shine a light on more realistic work function values for the molybdenum oxide.

Bibliography

[1] D. Adachi, J. Luis Hernández, and K. Yamamoto, “Impact of carrier recombination on fill factor for large area heterojunction crystalline silicon solar cell with 25.1% efficiency,” *Appl. Phys. Lett.*, vol. 107, p. 233506, 2015.

[2] K. Yamamoto *et al.*, “High-efficiency heterojunction crystalline Si solar cell and optical splitting structure fabricated by applying thin-film Si technology,” *Jpn. J. Appl. Phys.*, vol. 54, p. 08KD15, 2015.

[3] S. Y. Lee *et al.*, “Analysis of a-Si:H/TCO contact resistance for the Si heterojunction back-contact solar cell,” *Sol. Energy Mater. Sol. Cells*, vol. 120, pp. 412–416, 2014.

[4] S. M. Sze, *Semiconductor Devices - Physics and Technology*. 2008.

[5] H. Fujiwara, T. Kaneko, and M. Kondo, “Application of hydrogenated amorphous silicon oxide layers to c-Si heterojunction solar cells,” *Appl. Phys. Lett.*, vol. 91, no. 13, p. 133508, 2007.

[6] Z. C. Holman *et al.*, “Current losses at the front of silicon heterojunction solar cells,” *IEEE J. Photovoltaics*, vol. 2, no. 1, pp. 7–15, 2012.

[7] P. Procel, G. Yang, O. Isabella, and M. Zeman, “Theoretical evaluation of contact stack for high efficiency IBC-SHJ solar cells,” *Sol. Energy Mater. Sol. Cells*, vol. 186, pp. 66–77, Nov. 2018.

[8] H. Fujiwara and M. Kondo, “Effects of a-Si:H layer thicknesses on the performance of a-Si:H/c-Si heterojunction solar cells,” *J. Appl. Phys.*, vol. 101, p. 54516, 2007.

[9] J. Melskens, B. W. H. van de Loo, B. Macco, L. E. Black, S. Smit, and W. M. M. Kessels, “Passivating Contacts for Crystalline Silicon Solar Cells: From Concepts and Materials to Prospects,” *IEEE J. Photovoltaics*, vol. 8, no. 2, pp. 373–388, 2018.

[10] L. G. Gerling *et al.*, “Transition metal oxides as hole-selective contacts in silicon heterojunctions solar cells,” *Sol. Energy Mater. Sol. Cells*, vol. 145, pp. 109–115, Feb. 2016.

[11] K. L. Chopra, P. D. Paulson, and V. Dutta, “Thin-film solar cells: an overview,” *Prog. Photovoltaics Res. Appl.*, vol. 12, no. 23, pp. 69–92, 2004.

[12] W. Qiu *et al.*, “An electron beam evaporated TiO2 layer for high efficiency planar perovskite solar cells on flexible polyethylene terephthalate substrates,” *J. Mater. Chem. A*, vol. 3, no. 45, pp. 22824–22829, Nov. 2015.

[13] Y. Zhao, A. M. Nardes, and K. Zhu, “Effective hole extraction using MoOx-Al contact in perovskite CH3NH3PbI3 solar cells,” *Appl. Phys. Lett.*, vol. 104, no. 21, p. 213906, May 2014.

[14] Y. C. Tseng, A. U. Mane, J. W. Elam, and S. B. Darling, “Ultrathin molybdenum oxide anode buffer layer for organic photovoltaic cells formed using atomic layer deposition,” *Sol. Energy Mater. Sol. Cells*, vol. 99, pp. 235–239, Apr. 2012.

[15] A. Fell *et al.*, “Input Parameters for the Simulation of Silicon Solar Cells in 2014,” *IEEE J. Photovoltaics*, vol. 5, no. 4, pp. 1250–1263, 2015.

[16] M. T. Greiner and Z. H. Lu, “Thin-film metal oxides in organic semiconductor devices: Their

electronic structures, work functions and interfaces," *NPG Asia Mater.*, vol. 5, no. 7, Jul. 2013.

[17] M. T. Greiner, M. G. Helander, W. M. Tang, Z.-B. Wang, J. Qiu, and Z. H. Lu, "Universal energy-level alignment of molecules on metal oxides," *Nat. Mater.*, vol. 11, no. 1, p. 76, 2012.

[18] S. Lany, "Band-structure calculations for the 3d transition metal oxides in GW," *Phys. Rev. B*, vol. 87, p. 85112, 2013.

[19] T. Matsushima and H. Murata, "Observation of space-charge-limited current due to charge generation at interface of molybdenum dioxide and organic layer," *Appl. Phys. Lett.*, vol. 95, no. 203306, Nov. 2009.

[20] S. Lany, J. Osorio-Guillén, and A. Zunger, "Origins of the doping asymmetry in oxides: Hole doping in NiO versus electron doping in ZnO," *Phys. Rev. B*, vol. 75, p. 241203(R), 2007.

[21] U. Würfel, A. Cuevas, and P. Würfel, "Charge carrier separation in solar cells," *IEEE J. Photovoltaics*, vol. 5, no. 1, pp. 461–469, 2015.

[22] J. Meyer, S. Hamwi, M. Kröger, W. Kowalsky, T. Riedl, and A. Kahn, "Transition metal oxides for organic electronics: Energetics, device physics and applications," *Advanced Materials*, vol. 24, no. 40. pp. 5408–5427, 23-Oct-2012.

[23] J. Bullock, D. Yan, A. Cuevas, Y. Wan, and C. Samundsett, "n- and p-type silicon Solar Cells with Molybdenum Oxide Hole Contacts," in *Energy Procedia*, 2015, vol. 77, pp. 446–450.

[24] L. G. Gerling, S. Mahato, C. Voz, R. Alcubilla, and J. Puigdollers, "Characterization of Transition Metal Oxide/Silicon Heterojunctions for Solar Cell Applications," *Appl. Sci.*, vol. 5, no. 4, pp. 695–705, Oct. 2015.

[25] V. Shrotriya, G. Li, Y. Yao, C. W. Chu, and Y. Yang, "Transition metal oxides as the buffer layer for polymer photovoltaic cells," *Appl. Phys. Lett.*, vol. 88, no. 7, p. 73508, 2006.

[26] W. Wu *et al.*, "Dopant-free back contact silicon heterojunction solar cells employing transition metal oxide emitters," *Phys. Status Solidi - Rapid Res. Lett.*, vol. 10, no. 9, pp. 662–667, 2016.

[27] M. Bivour, J. Temmler, H. Steinkemper, and M. Hermle, "Molybdenum and tungsten oxide: High work function wide band gap contact materials for hole selective contacts of silicon solar cells," *Sol. Energy Mater. Sol. Cells*, vol. 142, pp. 34–41, 2015.

[28] B. Macco, M. F. J. Vos, F. J, N. F. W. Thissen, A. A. Bol, and W. M. M. Kessels, "Low-temperature atomic layer deposition of MoOx for silicon heterojunction solar cells," *Phys. Status Solidi - Rapid Res. Lett.*, vol. 9, no. 7, pp. 393–396, 2015.

[29] J. Bullock *et al.*, "Efficient silicon solar cells with dopant-free asymmetric heterocontacts," *Nat. Energy*, vol. 1, no. 3, pp. 1–7, Mar. 2016.

[30] M. F. J. Vos, "Atomic layer deposition of molybdenum oxide for silicon heterojunction solar cells," Eindhoven University of Technology, 2015.

[31] L. Fang, S. J. Baik, and K. S. Lim, "Transition metal oxide window layer in thin film amorphous silicon solar cells," *Thin Solid Films*, vol. 556, pp. 515–519, 2014.

[32] Z. Liang *et al.*, "Interaction at the silicon/transition metal oxide heterojunction interface and its effect on the photovoltaic performance," *Phys. Chem. Chem. Phys.*, vol. 17, p. 27409, 2015.

[33] J. Dréon *et al.*, "23.5%-efficient silicon heterojunction silicon solar cell using molybdenum

oxide as hole-selective contact," *Nano Energy*, vol. 70, no. 104495, Jan. 2020.

[34] C. Battaglia *et al.*, "Hole Selective MoOx Contact for Silicon Solar Cells," *Nano Lett.*, vol. 14, no. 2, pp. 967–971, 2014.

[35] J. W. Rabalais, R. J. Colton, and A. M. Guzman, "Trapped electrons in substoichiometric MoO3 observed by X-ray electron spectroscopy," *Chem. Phys. Lett.*, vol. 29, no. 1, pp. 131–133, Nov. 1974.

[36] S. Y. Lin, Y. C. Chen, C. M. Wang, P. T. Hsieh, and S. C. Shih, "Post-annealing effect upon optical properties of electron beam evaporated molybdenum oxide thin films," *Appl. Surf. Sci.*, vol. 255, pp. 3868–3874, Jan. 2009.

[37] Z. Zhang *et al.*, "Impact of oxygen vacancy on energy-level alignment at MoOx/organic interfaces," *Appl. Phys. Express*, vol. 6, no. 9, p. 095701, Sep. 2013.

[38] F. Menchini *et al.*, "Transparent hole-collecting and buffer layers for heterojunction solar cells based on n-type-doped silicon," *Appl. Phys. A Mater. Sci. Process.*, vol. 124, no. 7, p. 489, Jul. 2018.

[39] C. Battaglia *et al.*, "Silicon heterojunction solar cell with passivated hole selective MoO x contact," *Appl. Phys. Lett.*, vol. 104, no. 11, p. 113902, Mar. 2014.

[40] L. Neusel, M. Bivour, and M. Hermle, "Selectivity issues of MoOx based hole contacts," in *Energy Procedia*, 2017, vol. 124, pp. 425–434.

[41] I. Irfan and Y. Gao, "Effects of exposure and air annealing on MoOx thin films," *J. Photonics Energy*, vol. 2, no. 1, p. 021213, 2012.

[42] C. Messmer, M. Bivour, J. Schon, S. W. Glunz, and M. Hermle, "Numerical Simulation of Silicon Heterojunction Solar Cells Featuring Metal Oxides as Carrier-Selective Contacts," *IEEE J. Photovoltaics*, vol. 8, no. 2, pp. 456–464, 2018.

[43] Mike Tang Soo Kiong Ah Sen, "Molybdenum oxide thin films for heterojunction crystalline silicon solar cells," Delft University of Technology, 2017.

[44] E. Canadell and M. H. Whangbo, "Conceptual Aspects of Structure-Property Correlations and Electronic Instabilities, with Applications to Low-Dimensional Transition-Metal Oxides," *Chem. Rev.*, vol. 91, no. 5, pp. 965–1034, Jul. 1991.

[45] A. Smets, K. Jäger, O. Isabella, R. van Swaaij, and M. Zeman, *Solar energy*. UIT Cambridge, 2015.

[46] J. L. Gray, "The Physics of the Solar Cell," in *Handbook of photovoltaic science and engineering*, 2011, pp. 82–128.

[47] C. G. B. Garrett and W. H. Brattain, "Physical Theory of Semiconductor Surfaces," *Phys. Rev.*, vol. 99, no. 2, pp. 376–387, 1955.

[48] W. Shockley and W. T. Read, "Statistics of the recombinations of holes and electrons," *Phys. Rev.*, vol. 87, no. 5, pp. 835–842, Sep. 1952.

[49] A. G. Aberle, "Surface passivation of crystalline silicon solar cells: a review," *Prog. Photovoltaics Res. Appl.*, vol. 8, no. 5, pp. 473–487, 2000.

[50] J. Mitchell, D. MacDonald, and A. Cuevas, "Thermal activation energy for the passivation of the n-type crystalline silicon surface by hydrogenated amorphous silicon," *Appl. Phys. Lett.*, vol. 94, no. 16, p. 162102, 2009.

[51] D. A. Neamen, *Semiconductor Physics and Devices Basic Principles*, Third. Mc Graw Hill, 2003.

[52] R. L. Anderson, “Germanium-Gallium Arsenide Heterojunctions [Letter to the Editor],” *IBM J. Res. Dev.*, vol. 4, no. 3, pp. 283–287, Apr. 1960.

[53] A. Schenk and G. Heiser, “Modeling and simulation of tunneling through ultra-thin gate dielectrics,” *J. Appl. Phys.*, vol. 81, no. 12, p. 7900, 1997.

[54] W. Goes *et al.*, “Identification of oxide defects in semiconductor devices: A systematic approach linking DFT to rate equations and experimental evidence,” *Microelectron. Reliab.*, vol. 87, pp. 286–320, Aug. 2018.

[55] C. K. Williams, “Kinetics of trapping, detrapping, and trap generation,” *J. Electron. Mater.*, vol. 21, no. 7, pp. 711–720, 1992.

[56] A. Gehring and S. Selberherr, “Modeling of tunneling current and gate dielectric reliability for nonvolatile memory devices,” *IEEE Trans. Device Mater. Reliab.*, vol. 4, no. 3, pp. 306–319, 2004.

[57] Synopsys, “Sentaurus,” *Version K-2015.06*, 2015. .

[58] Synopsys, “TCAD Sentaurus: Sentaurus Device User Guide,” *Version K-2015.06*, 2015. .

[59] P. P. Altermatt, “Models for numerical device simulations of crystalline silicon solar cells - A review,” *J. Comput. Electron.*, vol. 10, no. 3, pp. 314–330, 2011.

[60] J. Bullock, A. Cuevas, T. Allen, and C. Battaglia, “Molybdenum oxide MoOx: A versatile hole contact for silicon solar cells,” *Appl. Phys. Lett.*, vol. 105, no. 23, p. 232109, 2014.

[61] D. Menzel, M. Mews, B. Rech, and L. Korte, “Electronic structure of indium-tungsten-oxide alloys and their energy band alignment at the heterojunction to crystalline silicon,” *Appl. Phys. Lett.*, vol. 112, no. 011602, pp. 1–5, 2018.

[62] H. Mehmood, H. Nasser, T. Tauqeer, S. Hussain, E. Ozkol, and R. Turan, “Simulation of an efficient silicon heterostructure solar cell concept featuring molybdenum oxide carrier-selective contact,” *Int. J. Energy Res.*, vol. 42, no. 4, pp. 1563–1579, 2018.

[63] K. Horio and H. Yanai, “Numerical Modeling of Heterojunctions Including the Thermionic Emission Mechanism at the Heterojunction Interface,” *IEEE Trans. Electron Devices*, vol. 37, no. 4, pp. 1093–1098, 1990.

[64] M. K. Ieong, P. M. Solomon, S. E. Laux, H. S. P. Wong, and D. Chidambarrao, “Comparison of raised and Schottky source/drain MOSFETs using a novel tunneling contact model,” in *International Electron Devices Meeting 1998. Technical Digest (Cat. No. 98CH36217)*, 1998, pp. 733–736.

[65] E. O. Kane, “Theory of Tunneling,” *J. Appl. Phys.*, vol. 32, p. 83, 1961.

[66] C. Canali, G. Majni, R. Minder, and G. Ottaviani, “Electron and Hole Drift Velocity Measurements in Silicon and Their Empirical Relation to Electric Field and Temperature,” *IEEE Trans. Electron Devices*, vol. 22, no. 11, pp. 1045–1047, 1975.

[67] Ioffe Physical Technical Institute, “Physical Properties of Semiconductors.” [Online]. Available: http://www.ioffe.ru/SVA/NSM/Semicond/. [Accessed: 24-Mar-2020].

[68] A. Schenk, “Finite-temperature full random-phase approximation model of band gap narrowing for silicon device simulation,” *J. Appl. Phys.*, vol. 84, no. 7, p. 3684, 1998.

[69] D. J. Roulston, N. D. Arora, and S. G. Chamberlain, “Modeling and Measurement of Minority-Carrier Lifetime versus Doping in Diffused Layers of n+-p Silicon Diodes,” *IEEE Trans. Electron Devices*, vol. 29, no. 2, pp. 284–291, 1982.

[70] A. Richter, F. Werner, A. Cuevas, J. Schmidt, and S. W. Glunz, “Improved parameterization

of Auger recombination in silicon," *Energy Procedia*, vol. 27, pp. 88–94, 2012.

[71] D. B. M. Klaassen, "A unified mobility model for device simulation? I. Model equations and concentration dependence," *Solid State Electron.*, vol. 35, no. 7, pp. 953–959, 1992.

[72] D. Scire and P. Procel, "To be published."

[73] A. Klein *et al.*, "Transparent Conducting Oxides for Photovoltaics: Manipulation of Fermi Level, Work Function and Energy Band Alignment," *Materials (Basel).*, vol. 3, pp. 4892–4914, Nov. 2010.

[74] M. Sayer, A. Mansingh, J. B. Webb, and J. Noad, "Long-range potential centres in disordered solids," *J. Phys. C Solid State Phys.*, vol. 11, no. 2, p. 315, 1978.

[75] J. Meyer and A. Kahn, "Electronic structure of molybdenum-oxide films and associated charge injection mechanisms in organic devices," *J. Photonics Energy*, vol. 1, no. 011109, Jan. 2011.

[76] R. A. Vijayan *et al.*, "Hole-Collection Mechanism in Passivating Metal-Oxide Contacts on Si Solar Cells: Insights from Numerical Simulations," *IEEE J. Photovoltaics*, vol. 8, no. 2, pp. 473–482, 2018.

[77] M. Gao *et al.*, "Bifunctional Hybrid a-SiOx(Mo) Layer for Hole-Selective and Interface Passivation of Highly Efficient MoOx/a-SiOx(Mo)/n-Si Heterojunction Photovoltaic Device," *ACS Appl. Mater. Interfaces*, vol. 10, pp. 27454–27464, 2018.

[78] N. Oka *et al.*, "Study on MoO3-x films deposited by reactive sputtering for organic light-emitting diodes," *J. Vac. Sci. Technol. A Vacuum, Surfaces, Film.*, vol. 28, no. 4, pp. 886–889, Jul. 2010.

[79] I. Irfan *et al.*, "Energy level evolution of air and oxygen exposed molybdenum trioxide films," *Appl. Phys. Lett.*, vol. 96, no. 24, p. 243307, Jun. 2010.

[80] D. Sacchetto *et al.*, "ITO/MoOx/a-Si:H(i) Hole-Selective Contacts for Silicon Heterojunction Solar Cells: Degradation Mechanisms and Cell Integration," *IEEE J. Photovoltaics*, vol. 7, no. 6, pp. 1584–1590, Nov. 2017.

[81] J. Cho *et al.*, "Interface analysis and intrinsic thermal stability of MoOx based hole-selective contacts for silicon heterojunction solar cells," *Sol. Energy Mater. Sol. Cells*, vol. 201, p. 110074, 2019.

[82] L. G. Gerling, C. Voz, R. Alcubilla, and J. Puigdollers, "Origin of passivation in hole-selective transition metal oxides for crystalline silicon heterojunction solar cells," *J. Mater. Res.*, vol. 32, no. 2, pp. 260–268, 2017.

[83] J. Geissbühler *et al.*, "22.5% Efficient Silicon Heterojunction Solar Cell With Molybdenum Oxide Hole Collector," *Appl. Phys. Lett.*, vol. 107, p. 081601, 2015.

[84] J.-H. Yang *et al.*, "Dopant-Free Hydrogenated Amorphous Silicon Thin-Film Solar Cells Using Molybdenum Oxide and Lithium Fluoride," *J. Phys. Chem. C*, vol. 117, pp. 23459–23468, 2013.

[85] Z. A. Weinberg, G. W. Rubloff, and E. Bassous, "Transmission, photoconductivity, and the experimental band gap of thermally grown SiO2 films," *Phys. Rev. B*, vol. 19, no. 6, pp. 3107–3117, Mar. 1979.

[86] M. T. Greiner, L. Chai, M. G. Helander, W. M. Tang, and Z. H. Lu, "Transition metal oxide work functions: The influence of cation oxidation state and oxygen vacancies," *Adv. Funct. Mater.*, vol. 22, no. 21, pp. 4557–4568, Nov. 2012.

[87] P. Schulz *et al.*, "High-Work-Function Molybdenum Oxide Hole Extraction Contacts in

Hybrid Organic−Inorganic Perovskite Solar Cells," *Appl. Mater. interfaces*, vol. 8, pp. 31491–31499, 2016.

[88] J. Shewchun, R. Singh, and M. A. Green, "Theory of metal-insulator-semiconductor solar cells," *J. Appl. Phys.*, vol. 48, no. 2, pp. 765–770, Feb. 1977.

[89] J. Bisquert, *Nanostructured Energy Devices: Equilibrium Concepts and Kinetics*. CRC Press, 2014.

[90] U. Würfel *et al.*, "How Molecules with Dipole Moments Enhance the Selectivity of Electrodes in Organic Solar Cells – A Combined Experimental and Theoretical Approach," *Adv. Energy Mater.*, vol. 6, no. 1600594, pp. 1–11, 2016.

[91] P. Procel *et al.*, "Opto-electrical modelling and optimization study of a novel IBC c-Si solar cell," *Prog. Photovoltaics Res. Appl.*, vol. 25, pp. 452–469, 2017.

[92] M. T. Greiner, L. Chai, M. G. Helander, W. M. Tang, and Z. H. Lu, "Metal/metal-oxide interfaces: How metal contacts affect the work function and band structure of MoO3," *Adv. Funct. Mater.*, vol. 23, pp. 215–226, 2013.

[93] M. Tanaka *et al.*, "Development of New a-Si/c-Si Heterojunction Solar Cells: ACJ-HIT (Artificially Constructed Junction-Heterojunction with Intrinsic Thin-Layer)," *Jpn. J. Appl. Phys.*, vol. 31, no. 3518, 1992.

[94] J. Coomer, "Density Functional Theory for Beginners," *University of Exeter*. [Online]. Available: http://newton.ex.ac.uk/research/qsystems/people/coomer/dft_intro.html. [Accessed: 29-Jan-2020].

[95] P. Erhart, "A very short introduction to density functional theory (DFT), from the course Condensed matter physics." 2016.

[96] R. M. Martin, "Density Functional theory, from the course Bridging Time and Length Scales in Materials Science and Biophysics." 2015.

[97] M. Born and R. Oppenheimer, "Zur Quantentheorie der Molekeln," *Ann. Phys.*, vol. 389, no. 20, pp. 457–484, Jan. 1927.

[98] M. Asta, "Density Functional Theory, An Introduction, from The 4th Summer School for Integrated Computational Materials Education." 2018.

[99] P. Hohenberg and W. Kohn, "Inhomogeneous electron gas," *Phys. Rev.*, vol. 136, no. 3B, p. B864, Nov. 1964.

[100] W. Kohn and L. J. Sham, "Self-consistent equations including exchange and correlation effects," *Phys. Rev.*, vol. 140, no. 4A, p. A1133, Nov. 1965.

[101] K. Capelle, "A Bird's-Eye View of Density-Functional Theory," *Brazilian J. Phys.*, vol. 36, no. 4A, pp. 1318–1343, 2006.

[102] G. Kresse and J. Furthmüller, "Efficient iterative schemes for ab initio total-energy calculations using a plane-wave basis set," *Phys. Rev. B*, vol. 54, no. 16, pp. 11169–11186, Oct. 1996.

[103] G. Kresse and J. Furthmüller, "Efficiency of ab-initio total energy calculations for metals and semiconductors using a plane-wave basis set," *Comput. Mater. Sci.*, vol. 6, pp. 15–50, Jul. 1996.

[104] G. Kresse, M. Marsman, and J. Furthmüller, *VASP the GUIDE*. 2018.

[105] H. J. Monkhorst and J. D. Pack, "Special points for Brillouin-zone integrations," *Phys. Rev. B*, vol. 13, no. 12, pp. 5188–5192, Jun. 1976.

[106] P. E. Blochl, “Projector augmented-wave method,” *Phys. Rev. B*, vol. 50, no. 24, pp. 17953–17979, 1994.

[107] G. Kresse and D. Joubert, “From ultrasoft pseudopotentials to the projector augmented-wave method,” *Phys. Rev. B*, vol. 59, no. 3, pp. 1758–1775, 1999.

[108] M. C. Gibson, “Implementation and Application of Advanced Density Functionals,” Durham, 2006.

[109] P. Ziesche, S. Kurth, and J. P. Perdew, “Density functionals from LDA to GGA,” *Comput. Mater. Sci.*, vol. 11, no. 2, pp. 122–127, Apr. 1998.

[110] J. P. Perdew, “Accurate Density Functional for the Energy: Real-Space Cutoff of the Gradient Expansion for the Exchange Hole,” *Phys. Rev. Lett.*, vol. 55, no. 16, pp. 1665–1668, 1985.

[111] J. P. Perdew, K. Burke, and M. Ernzerhof, “Generalized Gradient Approximation Made Simple,” *Phys. Rev. Lett.*, vol. 77, no. 18, p. 3865, 1996.

[112] W. Gao, T. A. Abtew, T. Cai, Y. Y. Sun, S. Zhang, and P. Zhang, “On the applicability of hybrid functionals for predicting fundamental properties of metals,” *Solid State Commun.*, vol. 234–235, pp. 10–13, May 2016.

[113] J. P. Perdew, M. Ernzerhof, and K. Burke, “Rationale for mixing exact exchange with density functional approximations,” *J. Chem. Phys.*, vol. 105, no. 22, pp. 9982–9985, Dec. 1996.

[114] D. Fritsch, B. J. Morgan, and A. Walsh, “Self-Consistent Hybrid Functional Calculations: Implications for Structural, Electronic, and Optical Properties of Oxide Semiconductors,” *Nanoscale Res. Lett.*, vol. 12, no. 1, Dec. 2017.

[115] H. Ding, K. G. Ray, V. Ozolins, and M. Asta, “Structural and vibrational properties of α-MoO3 from van der Waals corrected density functional theory calculations,” *Phys. Rev. B*, vol. 85, no. 012104, 2012.

[116] K. Inzani, M. Nematollahi, F. Vullum-Bruer, T. Grande, T. W. Reenaas, and S. M. Selbach, “Electronic properties of reduced molybdenum oxides,” *Phys. Chem. Chem. Phys.*, vol. 19, no. 13, pp. 9232–9245, 2017.

[117] M. Dion, H. Rydberg, E. Schrö, D. C. Langreth, and B. I. Lundqvist, “Van der Waals Density Functional for General Geometries,” *Phys. Rev. Lett.*, vol. 92, no. 24, p. 246401, 2004.

[118] K. Lee, É. D. Murray, L. Kong, B. I. Lundqvist, and D. C. Langreth, “Higher-accuracy van der Waals density functional,” *Phys. Rev. B*, vol. 82, no. 081101, 2010.

[119] J. Klimeš, D. R. Bowler, and A. Michaelides, “Van der Waals density functionals applied to solids,” *Phys. Rev. B*, vol. 83, no. 195131, 2011.

[120] J. Klimeš, D. R. Bowler, and A. Michaelides, “Chemical accuracy for the van der Waals density functional,” *J. Phys. Condens. matter*, vol. 22, no. 022201, 2010.

[121] G. Román-Pérez and J. M. Soler, “Efficient Implementation of a van der Waals Density Functional: Application to Double-Wall Carbon Nanotubes,” *Phys. Rev. Lett.*, vol. 103, no. 9, p. 096102, 2009.

[122] S. A. Tolba, K. M. Gameel, B. A. Ali, H. A. Almossalami, and N. K. Allam, “The DFT+U: Approaches, Accuracy and Applications,” in *Density Functional Calculations: Recent Progresses of Theory and Application*, 2018, p. 1.

[123] S. L. Dudarev, G. A. Botton, S. Y. Savrasov, C. J. Humphreys, and A. P. Sutton, “Electron-energy-loss spectra and the structural stability of nickel oxide: An LSDA+U study,” *Phys.*

Rev. B, vol. 57, no. 3, pp. 1505–1509, 1998.

[124] K. Inzani, T. Grande, F. Vullum-Bruer, and S. M. Selbach, “A van der Waals Density Functional Study of MoO3 and Its Oxygen Vacancies,” *J. Phys. Chem. C*, vol. 120, pp. 8959–8968, 2016.

[125] J. Heyd, G. E. Scuseria, and M. Ernzerhof, “Hybrid functionals based on a screened Coulomb potential,” *J. Chem. Phys.*, vol. 118, no. 8207, 2003.

[126] F. Fuchs, J. Furthmüller, F. Bechstedt, M. Shishkin, and G. Kresse, “Quasiparticle band structure based on a generalized Kohn-Sham scheme,” *Phys. Rev. B*, vol. 76, no. 115109, 2007.

[127] A. V Krukau, O. A. Vydrov, A. F. Izmaylov, and G. E. Scuseria, “Influence of the exchange screening parameter on the performance of screened hybrid functionals,” *J. Chem. Phys.*, vol. 125, no. 224106, 2006.

[128] B. Höffling, “The Interfaces between Silicon and Transparent Conducting Oxides,” Friedrich-Schiller-Universität Jena, 2015.

[129] I. Štich, R. Car, and M. Parrinello, “Amorphous silicon studied by ab initio molecular dynamics: Preparation, structure, and properties,” *Phys. Rev. B*, vol. 44, no. 20, pp. 11092–11104, Nov. 1991.

[130] A. S. Dalton and E. G. Seebauer, “Structure and mobility on amorphous silicon surfaces,” *Surf. Sci.*, vol. 550, pp. 140–148, 2004.

[131] K. Jarolimek, “Atomistic Models of Amorphous Semiconductors,” 2011.

[132] M. Tosolini, L. Colombo, and M. Peressi, “Atomic-scale model of c-Si/a-Si:H interfaces,” *Phys. Rev. B*, vol. 69, p. 075301, 2004.

[133] E. J. Albenze and P. Clancy, “Interface Response Functions for Amorphous and Crystalline Si and the Implications for Explosive Crystallization,” *Mol. Simul.*, vol. 31, no. 1, pp. 11–24, Jan. 2005.

[134] S. Izumi, S. Hara, T. Kumagai, and S. Sakai, “Structural and mechanical properties of well-relaxed amorphous-crystal interface in silicon: Molecular dynamics study,” *Comput. Mater. Sci.*, vol. 31, no. 3–4, pp. 279–286, Nov. 2004.

[135] T. Hom, W. Kiszenik, and B. Post, “Accurate lattice constants from multiple reflection measurements. II. Lattice constants of germanium silicon, and diamond,” *J. Appl. Crystallogr.*, vol. 8, no. 4, pp. 457–458, Aug. 1975.

[136] M. I. Aroyo *et al.*, “Bilbao Crystallographic Server: I. Databases and crystallographic computing programs,” in *Zeitschrift für Kristallographie-Crystalline Materials*, 2006, vol. 221, no. 1, pp. 15–27.

[137] A. Kokalj, “XCrySDen-a new program for displaying crystalline structures and electron densities,” *J. Mol. Graph. Model.*, vol. 17, pp. 176–179, Jun. 1999.

[138] P. F. Carcia and E. M. McCarron, “Synthesis and properties of thin film polymorphs of molybdenum trioxide,” *Thin Solid Films*, vol. 155, no. 1, pp. 53–63, Dec. 1987.

[139] G. Andersson and A. Magneli, “On the crystal structure of Molybdenum Trioxide,” *Acta Chem. Scand.*, vol. 4, pp. 793–797, 1950.

[140] E. Burattini, J. Purans, and A. Kuzmin, “XAFS studies of octahedral amorphous oxides,” *Japanese J. Appl. Physics-supplement*, vol. 32, pp. 655–655, 1993.

[141] D. O. Scanlon, G. W. Watson, D. J. Payne, G. R. Atkinson, R. G. Egdell, and D. S. L. Law,

"Theoretical and Experimental Study of the Electronic Structures of MoO3 and MoO2," *J. Phys. Chem. C*, vol. 114, pp. 4636–4645, 2010.

[142] B. G. Brandt and A. C. Skapski, "A Refinement of the Crystal Structure of Molybdenum Dioxide," *Acta Chem. Scand.*, vol. 21, pp. 661–672, 1967.

[143] I. A. de Castro *et al.*, "Molybdenum Oxides – From Fundamentals to Functionality," *Adv. Mater.*, vol. 29, no. 1701619, pp. 1–31, 2017.

[144] H. Sitepu, B. H. O'connor, and D. Li, "Comparative evaluation of the March and generalized spherical harmonic preferred orientation models using X-ray diffraction data for molybdite and calcite powders," *J. Appl. Crystallogr.*, vol. 38, no. 1, pp. 158–167, 2005.

[145] Laalitha Liyanage, "Running a DFT calculation in VASP, from ICME Fall." 2012.

[146] H. B. Michaelson, "The work function of the elements and its periodicity," *J. Appl. Phys.*, vol. 48, p. 4729, 1977.

[147] L. Bengtsson, "Dipole correction for surface supercell calculations," *Phys. Rev. B*, vol. 59, no. 19, p. 12301, 1999.

[148] C. He, "Work function of (001) and (00-1) surface of α-Fe2O3," *Mod. Phys. Lett. B*, vol. 32, no. 17, p. 1850188, 2018.

[149] P.-R. Huang, Y. He, C. Cao, and Z.-H. Lu, "Impact of lattice distortion and electron doping on a-MoO 3 electronic structure," *Sci. Rep.*, vol. 4, no. 7131, 2014.

[150] R. Tokarz-Sobieraj, K. Hermann, M. Witko, A. Blume, G. Mestl, and R. Schlögl, "Properties of oxygen sites at the MoO3(010) surface: Density functional theory cluster studies and photoemission experiments," *Surf. Sci.*, vol. 489, no. 1–3, pp. 107–125, Aug. 2001.

[151] S. D. Al-Alagawi, M. A. Aboud, and A.-R. K. Ali, "Optical Method to Determine the Orientation of Monocrystalline Silicon," 2007.

[152] A. Papakondylis and P. Sautet, "Ab Initio Study of the Structure of the a-MoO3 Solid and Study of the Adsorption of H2O and CO Molecules on Its (100) Surface," *J. Phys. Chem.*, vol. 100, no. 25, pp. 10681–10688, 1996.

[153] V. Agarwal and H. Metiu, "Oxygen Vacancy Formation on α-MoO3 Slabs and Ribbons," *J. Phys. Chem. C*, vol. 120, pp. 19252–19264, 2016.

[154] M. Biron, *Material Selection for Thermoplastic Parts: Practical and Advanced Information*. William Andrew, 2015.

[155] M. A. Hopcroft, W. D. Nix, and T. W. Kenny, "What is the Young's modulus of silicon?," *J. Microelectromechanical Syst.*, vol. 19, no. 2, pp. 229–238, Apr. 2010.

[156] D. Liu *et al.*, "High-pressure Raman scattering and x-ray diffraction of phase transitions in MoO3," *J. Appl. Phys.*, vol. 105, no. 023513, Jan. 2009.

[157] S. Duwal, M. Kim, S. Kawaguchi, N. Hirao, Y. Ohishi, and C. S. Yoo, "Phase Transitions and Resistivity Anomaly of Layered MoO3 at High Pressure," *J. Phys. Chem. C*, vol. 122, no. 39, pp. 22632–22641, Oct. 2018.

[158] F. Weinhold and R. West, "The Nature of the Silicon-Oxygen Bond," *Organometallics*, vol. 30, pp. 5815–5824, 2011.

[159] S. P. Sun *et al.*, "First principles investigation of the surface stability and equilibrium morphology of MoO3," *Appl. Surf. Sci.*, vol. 467, pp. 753–759, Feb. 2019.

[160] A. J. Garza and G. E. Scuseria, "Predicting Band Gaps with Hybrid Density Functionals," *J. Phys. Chem. Lett.*, vol. 7, pp. 4165–4170, Oct. 2016.

[161] J. E. Moussa, P. A. Schultz, and J. R. Chelikowsky, “Analysis of the Heyd-Scuseria-Ernzerhof density functional parameter space,” *J. Chem. Phys.*, vol. 136, no. 204117, 2012.

[162] A. H. Reshak, “Specific features of electronic structures and optical susceptibilities of molybdenum oxide,” *RSC Adv.*, vol. 5, no. 22044, 2015.

[163] H. Peelaers and C. G. V. de W. Materials, “First-principles study of van der Waals interactions in MoS2 and MoO3,” *J. Phys. Condens. Matter*, vol. 26, no. 305502, 2014.

[164] S. Il Park, S. Jae Baik, J. S. Im, L. Fang, J. W. Jeon, and K. Su Lim, “Towards a high efficiency amorphous silicon solar cell using molybdenum oxide as a window layer instead of conventional p-type amorphous silicon carbide,” *Appl. Phys. Lett.*, vol. 99, no. 6, p. 063504, Aug. 2011.

[165] K. H. Wong, K. Ananthanarayanan, J. Luther, and P. Balaya, “Origin of Hole Selectivity and the Role of Defects in Low-Temperature Solution-Processed Molybdenum Oxide Interfacial Layer for Organic Solar Cells,” *J. Phys. Chem. C*, vol. 116, pp. 16346–16351, 2012.

[166] M. Anwar and C. A. Hogarth, “Optical properties of amorphous thin films of MoO3 deposited by vacuum evaporation,” *Phys. Status Solidi*, vol. 109, no. 2, pp. 469–478, Oct. 1988.

[167] B. Höffling, F. Ortmann, K. Hannewald, and F. Bechstedt, “Organic-Metal Interface: Adsorption of Cysteine on Au(110) from First Principles,” in *High Performance Computing in Science and Engineering ’10, Heidelberg, Springer*, 2011, pp. 119–134.

[168] Y. Yang, J. Zhou, M. Nakayama, L. Nie, P. Liu, and M. G. White, “Surface dipoles and electron transfer at the metal oxide-metal interface: A 2PPE study of size-selected metal oxide clusters supported on Cu(111),” *J. Phys. Chem. C*, vol. 118, no. 25, pp. 13697–13706, 2014.